2013

# Multi-scale modeling of inertial flows through propped fractures

Ali Takbiri Borujeni
*Louisiana State University and Agricultural and Mechanical College*

# MULTI-SCALE MODELING OF INERTIAL FLOWS THROUGH PROPPED FRACTURES

A Dissertation

Submitted to the Graduate Faculty of the
Louisiana State University and
Agricultural and Mechanical College
in partial fulfillment of the
requirements for the degree of
Doctor of Philosophy

in

The Craft & Hawkins Department of Petroleum Engineering

by
Ali Takbiri Borujeni
B.S., Petroleum University of Technology, 2005
M.S., Petroleum University of Technology, 2007
M.S., Institute Francais du Petrole, 2007
August 2013

# Acknowledgements

I am most grateful to my advisor, Dr. Mayank Tyagi for the opportunity to work under him and for providing me with guidance and the resources; my committee members, Drs. Karsten Thompson and Dan Rao and my Physics minor advisor Dr. Jonathan Dowling for their invaluable contributions and criticisms that have given shape to this work; I would also like to thank Dr. Christopher White for useful discussions and contributions in the earlier part of this research. I would like to acknowledge the financial support of ExxonMobil Upstream Research Company for the financial support of this project and my studies. I want to thank the Craft and Hawkins department, the Chair and Faculty of Petroleum Engineering for giving me the opportunity to undertake my graduate studies, for the invaluable knowledge gained during my studies and the discussions I benefitted from while carrying out this work. I express my gratitude to the PALABOS group (www.lbmethod.org/palabos) for the open source code which was used to implement the LBM algorithm.

I am appreciative of my friends and colleagues with whom I shared and gained useful ideas. This includes, Nathan Lane, Yijie Shen, Paula Sanematsu, Seth Bradley, Chukwudi Chukwudozie, Masoud Safari-Zanjani, and Kasra Fattah. In addition, I acknowledge the Louisiana Optical Network Initiative (LONI) and the Center for Computation and Technology (CCT) at LSU for granting me access to High Performance Computing (HPC) resources on which the simulations in this work were carried out. I also thank the members of staff at the CCT, especially Dr. Le Yan for helping me resolve some of the problems I faced while using the HPC systems. Finally, I am eternally indebted to my parents and siblings for the love and moral support they have given to me throughout my academic sojourn. Indeed, to them is this work dedicated.

I would like to thank my parents who have always been constant sources of support and encouragement and their values have helped pave the path of privileged education.

This dissertation is dedicated to my parents, my sister Sara, and my brothers Hojat and Sasan.

# Table of Contents

# List of Tables

# List of Figures

# Nomenclature

## General Symbols

| | |
|---|---|
| $T_{gx_{i\pm1/2,j}}$ | Gas transmissibility along the x-direction between Gridblock (i,j) and Gridblock (i±1,j) |
| $\bar{p}_r$ | Reservoir average pressure |
| $\langle v \rangle$ | Volume averaged velocity of the fluid |
| $\langle V_z \rangle$ | Calculated average z-direction velocity |
| $\nabla P$ | Dynamic pressure gradient in the fluid |
| $A_i$ | Cross-sectional area perpendicular to $i$ (x, y, or z) directions |
| $B_g$ | Gas formation volume factor (reservoir volume/volume at standard conditions) |
| $B_{gi}$ | Initial gas formation factor |
| $B_w$ | Water formation factor |
| $c_f$ | Rock compressibility |
| $c_s$ | Sound speed in the fluid |
| $c_w$ | Water compressibility |
| $D_p$ | Diameter of the particles |
| $f_i$ | Discrete distribution functions in $i$ direction in velocity space |
| $f_i^{eq}$ | Discrete equilibrium distribution functions in $i$ direction |
| $F_o$ | Forchheimer number |
| $G$ | Original gas in place |
| $G_p$ | Cumulative gas production |
| $J_g$ | Productivity index of gas reservoir |

| | |
|---|---|
| $K$ | Permeability tensor of the porous medium |
| $k_{int}$ | Intrinsic permeability of the porous media |
| $k_{int}$ | Intrinsic permeability of the porous medium |
| $L$ | Length of the porous media |
| $L_e$ | Traveled distance by the fluids |
| $p_i$ | Initial pressure |
| $P_{i,j}$ | Pressure of Gridblock (i,j) |
| $p_{wf}$ | Flowing bottom hole pressure |
| $Re$ | Reynolds number |
| $S_{wi}$ | Initial water saturation |
| $T$ | Tortuosity |
| $v$ | Velocity of the fluid in the porous media |
| $V_b$ | Volume of the grid block |
| $V_{z,i}$ | Calculated z-direction velocity for the grid $i$ |
| $V_{z,i}$ | Calculated z-direction velocity for the grid $i$ |
| $W_e$ | Water influx |
| $w_i$ | Weight factors for $i$ direction in Equation 2.5 |
| $W_p$ | Cumulative water production |
| $Z$ | Elevation of the center of the grid block |
| $z_i$ | Initial gas compressibility factor |
| $\mathbf{e}_i$ | Directions $i$ in which fluid particles can move |

## Greek Symbols

| | |
|---|---|
| $\alpha_c$ | Volume conversion factor |
| $\beta_c$ | Transmissibility conversion factor |
| $c_\phi$ | Rock compressibility |
| $\bar{\rho}$ | Average density of the fluid |
| $\beta$ | Inertial or non-Darcy parameter |

$\Delta p$ Pressure drop

$\Delta V_{z,i}$ Difference between the normalized calculated z-direction velocity of LB and FEM for the grid $i$

$\mu$ Viscosity of the fluid

$\phi$ Porosity of the rock in the grid block

$\rho$ Density of the fluid

## Superscripts

$FEM$ Finite Element MEthod

$LB$ Lattice Boltzmann

0 Initial timestep

$\nu$ Old iteration

$\nu + 1$ New iteration

$n$ Reference

$n + 1$ New timestep

# Abstract

Non-Darcy flows are expected to be ubiquitous in near wellbore regions, completions, and in hydraulic fractures of high productivity gas wells. Further, the prevailing dynamic effective stress in the near wellbore region is expected to be an influencing factor for the completion conductivity and non-Darcy flow behavior in it. In other words, the properties (fracture permeability and $\beta$-factor) can vary with the time and location in the reservoir (especially in regions close to the wellbore). Using constant values based on empirical correlations for reservoirs/completions properties can lead to erroneous cumulative productivity predictions. With the recent advances in the imaging technology, it is now possible to reconstruct pore geometries of the proppant packs under different stress conditions. With further advances in powerful computing platforms, it is possible to handle large amount of computations such as Lattice Boltzmann (LB) simulations faster and more efficiently.

Calculated properties of the proppant pack at different confining stresses show reasonable agreement with the reported values for both permeability and $\beta$-factor. These predicted stress-dependent permeability and $\beta$-factors corresponding to the effective stress fields around the hydraulic fractured completions is included in a 2D gas reservoir simulator to calculate the productivity index.

In image-based flow simulations, spatial resolution of the digital images used for modeling is critical not only because it dictates the scale of features that can be resolved, but also because for most techniques there is at least some relationship between voxel size in the image data and numerical resolution applied to the computational simulations. In this work we investigate this relationship using a computer-generated consolidated porous medium, which

was digitized at voxel resolutions in the range 2-10 microns. These images are then used to compute permeability and tortuosity using lattice Boltzmann (LB) and compared against finite elements methods (FEM)simulation results. Results show how changes in computed permeability are affected by image resolution (which dictates how well the pore geometry is approximated) versus grid or mesh resolution (which changes numerical accuracy). For LB, the image and grid resolution are usually taken to be the same; we show at least one case where effects of grid and image resolution appear to counteract one another, giving the mistaken appearance of resolution-independent results. For FEM, meshing can provide certain attributes (such as better conformance to surfaces), but it also adds an extra step for error or approximation to be introduced in the workflow.

# Chapter 1
# Introduction

## 1.1 Pore-scale Image-based flow simulations using Lattice Boltzmann Method

In geoscience and petroleum engineering studies, estimation of effective rock properties can often be performed using more than one approach, each with various benefits and drawbacks. Experimental approaches are preferred if it is not possible to account for all relevant physics by an equation or model; however, they tend to be time consuming and expensive. Empirical approaches provide simplicity, but are usually valid for limited conditions and sacrifice a connection to the underlying physics. For certain properties such as porosity, permeability, and non-Darcy factor, numerical simulation using digital images has become a credible alternative, enabled by improvements of 3D imaging techniques, numerical methods, and computing power. Appealing aspects of this approach include the ability to probe pore-scale physics at a level not possible with traditional experiments and the ability to perform an endless set of numerical tests without degrading or altering the sample. Considerations that can limit this digital approach include whether the imaging technique can resolve all relevant characteristic scales in the pore space and whether numerical algorithms are able to accurately model the physical processes.

For fluid flow problems, two main approaches to image-based pore-scale modeling have evolved, which differ based on how the pore space is discretized and how the flow equations are solved. Network models divide the pore space into a collection of pores connected by pore throats. Hence, the discretization is defined by the pore structure (usually not uniquely). Flow is solved by enforcing mass conservation at the pores and applying Poiseuille flow ap-

proximations in the pore throats. The second approach is more traditional computational modeling . The domain is discretized into nodes, voxels, or volume elements, and the resulting grid is used to numerically approximate the relevant partial differential equations for flow. The latter approach, which we will refer to as a computational fluid dynamics (CFD) approach can be further broken down into techniques that employ regular versus unstructured grids. While this distinction is often worth making in CFD studies, it is particularly important for image-based modeling because the voxel data from X-ray tomography or similar methods can be used directly as the numerical grid. This gridding approach has become widely used in porous media studies in conjunction with the lattice Boltzmann (LB) method, which has proved to be highly effective for simulating fluid flow through porous media [18, 53].

LB has been been applied to many porous media flow simulations. Succi et al. [73] were one of the first groups that employed LB to study flow of fluids in complex geometries such as porous media. In their study, they used LB to calculate permeability of porous media. The main result of their work was the LB adherence of Darcy's equation in complex 3D geometries. Ferreol and Rothman [18] simulated single phase flow through Fontainebleau Sandstone and found approximately the same permeability values as equivalent finite-difference calculations and laboratory measurements. Jin et al. [33] also presented an integrated procedure for the estimation of the absolute permeability of unconsolidated and consolidated reservoir rock. Challenges for applying LB to real problems include finite-size effects and relaxation time dependence of no-flow boundaries. In image-based simulations, the accuracy of the calculated macroscopic properties is dependent on the spatial resolution of the rock image [32, 51]. However, there is always a trade-off between the image resolution (and the related lattice spacing) versus computational power. Furthermore, in all digital samples, there is a resolution threshold, below which certain flow characteristics, such as recirculation, are not resolved [47]. The alternative to a regular numerical grid is an unstructured mesh used with a compatible computational method such as the finite element method (FEM) or finite volume

method (FVM). In the past, difficulties associated with unstructured mesh generation have limited their application to pore-scale modeling problems. However, recent improvements to meshing algorithms and the availability of commercial image-based meshing packages have made this less of a concern. In principle, unstructured meshes are well suited for pore-scale modeling for two reasons: an ability to conform to complicated geometries and the ability to employ local spatial refinement. The latter point is particularly significant for microscopically heterogeneous porous media because refinement allows small pores and/or regions critical to transport to be meshed at higher resolutions without introducing additional computational expense where it is not needed. A related advantage is that (depending on how much control the user has over mesh resolution) numerical resolution can be selected based on computational considerations independently of what voxel resolution was used in the digital imaging process.

Non-Darcy flow parameter can also be calculated using image-based flow simulations of real images of rocks. However, flow simulations for determining the non-Darcy flow parameter are more demanding than those for permeability calculations. There have been extensive work on computations of $\beta-$factor using numerical methods on images of porous rocks. Balhoff and Wheeler [6] simulated non-Darcy flows of an incompressible fluid using a physically representative pore-scale network model. LB simulations have also been used for determining the $\beta-$factor. Chukwudozie [11] used LB simulations to calculate permeabilities and $\beta-$factors of real images of Castlegate sandstone samples. Newman and Yin [56] simulated the transition between Darcy to non-Darcy flows in a synthetically generated 2D porous media using LB. In order to calculate $\beta$-factor using LB simulations, high pressure gradients (body forces) need to be applied to the computational domain. However, compressibility effects are a major issue for low porosity systems when pressure gradient to drive flow is implemented by density difference. For low porosity samples, high flow rate conditions can only be implemented by large density gradients, which invariably introduce fluid compressibility in an incompressible fluid system. Limit on Mach number puts a limit on the range of lat-

tice flow velocity and hence the upper limit on the Reynolds number that can be simulated. It implies that for systems with small length dimensions, only by increasing the numerical resolution can high flow rate conditions be simulated. Therefore, samples of porous media to be used for LB flow simulations should be at high resolutions to guarantee high Reynolds number regimes [11].

### 1.2 Stress-dependent permeability and non-Darcy factor

Fluid production/injection changes the pore pressure in the reservoir and as a result effective stress increases. As a result, physical properties of the porous media such as pore sizes, pore size distributions, and pore shapes may change. There are extensive studies on effect of confining increase on the change in the permeability of rocks [17, 64, 64, 70, 76, 78, 79, 84]. Change of permeability is attributed to change in pore shape and sorting, lithology, rock mineralogy, initial permeability value, and various aspects of pore structure.

Davies and Davies [14] stated that geometry of pores and rock types is the key in change of permeability with stress in both unconsolidated and consolidated sandstones. These changes have direct effect on the performance of both well and reservoir. They have direct impacts on reserve estimation, reservoir productivity, and management. A better reservoir simulation should have stress-dependent properties included [14].

Zoback and Byerlee [84] measured the effect of pore-pressure and confining stress on Berea Sand Stones. They mentioned that pore-pressure has more significant influence on the permeability than confining stress.

Jones and Owens [34] measured the effect of confining stress on the permeability of tight gas sands. they reported tat permeability of tight-gas sands can decreased almost ten-fold of surface pressure conditions. Reductions ranged from three to twenty-folds. They also mentioned that effect of confining stress on low permeability formations is mire severe because stress can limit the already tight pathways of fluid flow. They plotted cube root of the permeability against logarithm of confining stress and found a good linear match. They

also reported 5 to 10 percent decrease on pore volume.

According to Ye et al. [79], typically of intermediate and high strength ceramic proppants can be used up to 10 to 14 KPa before crushing of the grains occur. Crushing may cause the migration of debris and plugging of the flow pathways which can decrease the permeability and increase the inertial flow parameter.

In real cases, occasional shut-ins such as in well work-overs and pressure build-up tests, can decrease confining stresses on the proppants in the fractures, which causes cyclic-stress loading-unloading which may lead to fatigue failure and decrease in the productivity [30].

Among different causes of deviations from Darcy law are high velocities in the porous media, low Knudsen number flow, multiphase flow, and non-Newtonian rheology. The deviations due to high velocities of fluids are the main sources of deviations in the petroleum engineering applications. High flow rates exist near wellbore regions (where flow merges from a higher areas away from the well to a smaller region near the wellbore and completions), hydraulic fractures, high potential wells, naturally fractured reservoirs, and gravel packs [2].

For these flow conditions there is a need to develop modifications to the Darcy law to accurately predict excessive pressure drops across the the reservoir. One of the first relationships was proposed by Forchheimer [20]. He modified the Darcy law by adding a quadratic term to it. Cornell and Katz [12] redefined this quadratic term.

Deviation from Darcy equation is more significant in regions around the wellbore especially in fractured reservoirs. Augmented pressure drop around the wellbore limits the reservoir productivity. Conventional reservoir simulators are usually unable to account for inertia effects and seem to over-predict the reservoir performance. This causes problems when it comes to matching the data in history matching. Therefore, determining correct inertial flow parameter is required as an input for reservoir simulators. Holditch and Morse [29] built a 2D reservoir simulator including non-Darcy gas flow in hydraulic fracture to assess the effect of non-Darcy flow on the well performance. They concluded that non-Darcy flow could decrease the effective conductivity of by a factor of 20 or more. Guppy et al. [26]

studied the pressure build up data for finite-conductivity fractures producing at high flow rates. They concluded that the effect of non-Darcy flow on build up analysis causes the fracture conductivity to be smaller than the true conductivity. The difference could be as much as 85%.

### 1.3 Thesis Outline

In this research, first set of numerical investigations starts with a study of image resolution and numerical resolution to understand the interplay between these two effects and their impact on the accuracy of numerical predictions. Then, using LB simulations, permeability and $\beta$-factor for a proppant pack under confining stresses are estimated. Finally, the calculated results are incorporate into a single-phase gas reservoir simulator to see their impact on the productivity indices of the hydraulically fractured gas reservoirs. Chapter 2 outlines principles of fluid flows though porous media and the theoretical background of LB method. Darcy law and deviations from Darcy law at elevated velocities, and Forchheimer equation are introduced in this chapter. Moreover, LB equation are presented and its main challenges for flow simulations through porous media are highlighted.

In Chapter 3, the scaling performance of the parallel code used for the pore-scale simulations (PALABOS) is briefly presented.

Chapter 4 investigates the effect of the image and numerical resolutions on the accuracy of the simulations results for determining porous media properties such as permeability and tortuosities.

In Chapter 5, permeabilities and $\beta$-factors of a proppant pack at four different stress conditions are calculated using LB simulations. Calculated results in Chapter 6 are then used in a 2D reservoir gas simulator and their impact on the productivity indices are investigated. Effects of the fracture length and width, reservoir permeabilities, and flow rates on the productivity indices are also estimated.

Chapter 7 presents a summary and brief discussions of the results presented in the previous

chapters and also addresses future research that may be fruitful to other researchers.

All the CT-imaging and segmentation results used in this research were provided by Prof. Clint Willson (LSU) research group. In particular, Paula Sanematsu generated all the images of proppant packs under various stress loads.

Comparisons with FEM results were made possible with the collaborations of Prof. Karsten Thompson (LSU) research group. In particular, Yijie Shen and Nathan Lane performed all the FEM simulations that are presented in this work along with LB simulations.

# Chapter 2
# Background

## 2.1 Fundamentals of fluid flows through porous media

Laminar flow of single-phase fluid in porous media at low Reynolds number is described by Darcy law, which states that pressure drops are linearly proportional to the velocity of the fluid. For higher flow rates, however, this linear proportionality is no-longer valid and pressure drops are higher than what is predicted by the Darcy law.

There have been many views on appearance of this non-linearity. First investigators attributed it to the turbulence. Reynolds number utilization for finding the onset of the non-linearity is because of this school of thought. Geertsma [22], however, stated that the turbulence is not actually occurring in the pores of the porous rock and inertial flow resistance is the the reason for the excessive pressure drop in high flow rates. Some other researchers have also attributed it to the increase of microscopic drag force on the porous walls [27], [19]. In Darcy law, pressure drops across the porous media are due to the viscous drag of the fluid molecules on the surface of the rock. For higher fluid velocities, acceleration, deceleration, and recirculation of the fluids cause energy losses and therefore, excessive pressure drops. Figure 2.1 shows typical flow regimes in porous media. As can be seen, for high fluid velocities (high Reynolds numbers), the linear proportionally is not valid due to inertial flow contributions.

One of the first correlation to account for nonlinear effects was proposed by Forchheimer (1901),

$$\frac{\Delta p}{L} = \frac{\langle u \rangle \mu}{k_{int}} + \beta \rho \langle u \rangle |\langle u \rangle| \tag{2.1}$$

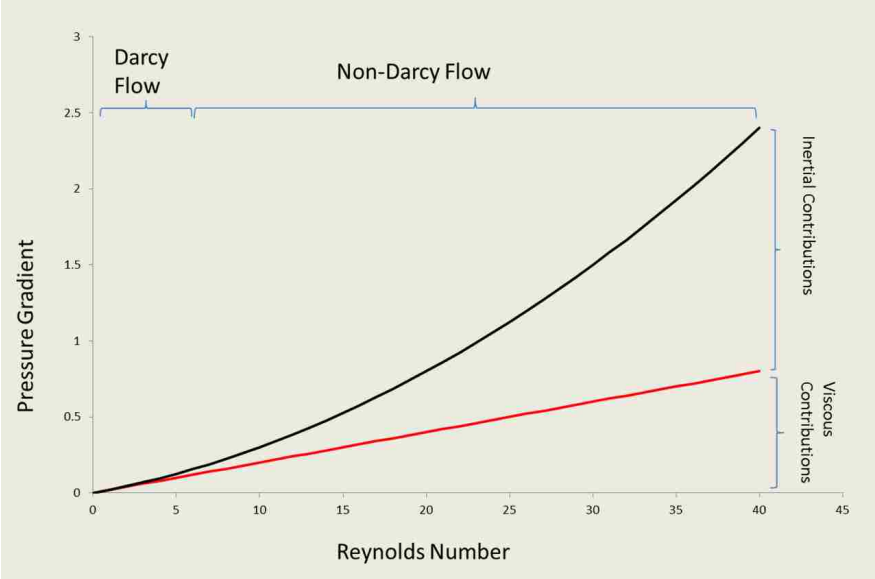


Figure 2.1: Typical flow regimes in porous media

where $k_{int}$ is the intrinsic permeability of the porous media, $\Delta p$ is the pressure drop, $L$ is the length of the porous media, $\beta$ (often called $\beta$-factor) is the inertial or non-Darcy parameter, $\langle v \rangle$ is the volume averaged velocity of the fluid in the media, $\rho$, and $\mu$ are the density and viscosity of the fluid, respectively.

In this equation, analogy to pipe flow has been assumed. In pipes, pressure gradient is dependent on the fluid velocities but in higher fluid velocities, in turbulent regime, pressure gradient is proportional to the square of the velocity of the fluid. However, this excessive pressure drop in the porous media can not be attributed to the turbulence because non-Darcy effects can cause excessive pressure drop where flow is still in the laminar regime.

Deviations from Darcy equation are given different names such as turbulence flow, inertial flow, and non-Darcy flow by different researchers. Firoozabadi and Katz [19] listed the nomenclature used in the literature for high velocity gas flow and attributed this deviation to the effects of increased microscopic drag forces on the pore walls. It is usually assumed that $\beta$- factor is one of the properties of the porous medium like permeability but flow experiments in porous media have shown that $\beta$- factor can also be a function of Reynolds number. Therefore, we might not get constant $\beta$- factor for a wide range of flow rates.

There have been two main types of criteria for determining the onset of the non-Darcy flow in the porous media [46, 82]. The first type is based on the Reynolds number in the porous media. Reynolds number is defined as

$$Re = \frac{\rho D_p v}{\mu} \tag{2.2}$$

where $D_p$ is the diameter of the particles, $\rho$ and $\mu$ are the density and viscosity of the fluid, and $v$ is the velocity of the fluid in the porous media. Critical value of the non-Darcy flow vary from 1 to 100. The second type is based on the Forchheimer number, which is defined as,

$$F_o = \frac{k_{int}\beta\rho v}{\mu} \tag{2.3}$$

where $k_{int}$ is the intrinsic permeability of the medium and $\beta$ is the non-Darcy flow parameter. According to the second criterion, the critical value varies from 0.005 to 0.2 [82].

## 2.2 Lattice Boltzmann method

LB is a simplification of the Boltzmann equation that solves for particle distribution functions in a discrete phase space. In this method, positions of particles are limited to nodes of a lattice with equal spacings [74]. Velocity magnitudes in each direction have particular values so that the distance between a particle and its neighbors is equal to the discrete velocity times the time steps.

Lattice Boltzmann models are denoted by $DdQq$ where $d$ shows the dimension of the simulation (either 2 or 3) and $q$ shows the number of discrete directions particle can move. LB consists of two steps: streaming and collision. In streaming, directional specific densities $f_i$ move towards their nearest neighbors. In the collision step, momentum exchange between the particles takes place due to collisions with each other at a particular node.

The LB equation with streaming and single velocity relaxation operator (LBGK) collision

is

$$f_i(\mathbf{x} + \mathbf{e}_i\Delta t, t + \Delta t) = f_i(\mathbf{x}, t) - \frac{(f_i(\mathbf{x}, t) - f_i^{eq}(\mathbf{x}, t))}{\tau} \tag{2.4}$$

where $\mathbf{e}_i$ are directions in which fluid particles can move and $f_i$ are the discrete distribution functions in velocity space. In this formulae, $f_i^{eq}$ are the equilibrium distribution functions,

$$f_i^{eq}(\mathbf{x}) = w_i \left[1 + \frac{(\mathbf{e_i}.\mathbf{u})}{{c_s}^2} + \frac{(\mathbf{e_i}.\mathbf{u})^2}{2{c_s}^4} - \frac{u^2}{2{c_s}^2}\right] \tag{2.5}$$

where $w_i$ are weight factors specific to different directions, $c_s = 1/\sqrt{3}$ is the sound speed in the fluid, $\mathbf{u}$ is the velocity of the fluid, and $\rho$ is the density of the fluid. Hydrodynamics variables, density and velocity, are calculated from first and second moments of particle distribution functions.

$$\rho(\mathbf{x}) = \sum_i f_i(\mathbf{x}) \tag{2.6}$$

$$\mathbf{u}(\mathbf{x}) = \frac{1}{\rho(\mathbf{x})} \sum_i f_i(\mathbf{x})\ \mathbf{e}_i \tag{2.7}$$

Traditional Navier-Stokes equations can be derived from LB equation for weakly compressible fluids in the low Mach number regime [37, 51]. Kinematic viscosity can be defined as $\nu = \frac{1}{3}(\tau - \frac{1}{2})$ in which $\tau$ should always be greater than 0.5. Fluid pressure is defined by

$$p(\mathbf{x}) = {c_s}^2(\rho(\mathbf{x}) - \bar{\rho}) \tag{2.8}$$

where $\bar{\rho}$ is the average density of the fluid.

### 2.2.1 Boundary conditions

The bounce-back boundary scheme is one of the most common no-flow boundary conditions implemented in LB simulations. In this scheme, distribution functions streamed from a fluid node to a neighboring solid node are implemented using reflected values along the same link.

The numerical accuracy of LB is proved to be second-order in space except in the bounce-

back boundary regions where the accuracy is only first-order accurate [10, 37, 48, 57, 58, 68]. There are several more complex no-slip boundary conditions with second-order accuracies. Many of these boundary conditions are only applicable for regular geometries [57, 68].

In a bounce-back scheme, the no-flow boundary is assumed to be at a halfway distance between the fluid and solid nodes for simple geometries. However, in more complex geometries such as porous media, the bounce-back scheme puts no-flow boundary somewhere between the wall and adjacent fluid nodes. Exact position of the no-flow boundary is dependent on the relaxation parameter and geometry of the system [28, 37, 40, 51]. Image resolution affects this issue because position dependence of the no-flow boundaries are more significant for lower resolution images.

Overall, for flow through porous media studies, the bounce-back scheme is more practical since it simplifies handling of complex pore-matrix boundaries and is computationally efficient. The low-order accuracy improves a few lattice spacings away from the wall and can be compatible with second-order accuracy of LB [37, 47, 48, 51, 69].

In practical simulations, the body force approach, which is an imitation of pressure boundary conditions at the inlet and outlet, is used in LB. In this approach, a pressure gradient acting on the fluid is replaced by an external force [9, 18].

### 2.2.2 Finite-size effects

Accuracy of the LB method depends on how well the numerical domain is resolved by lattice spacings. In cases that the numerical domain is not well-resolved, finite-size effects or Knudsen flow behavior may mask the true results [32, 51] .

To avoid these problems, the characteristic length of the computational domain should be at least the same order as the mean free path in order for results to describe hydrodynamic behavior of the flow [18]. Relaxation time also impacts finite-size effects. It controls the mean free path [51].

Finite-size effects generally decrease as smaller relaxation times are used [59]. Holdych

et al. [31] used a recursive application of the LB equation to achieve explicit forms for the effective variable stencils in LB schemes and obtained modified equations for fluid flow models. They found that truncation errors are second-order in space and are proportional to low-order polynomial orders of the relaxation time. They also assigned different values of the relaxation times for different flow regimes to minimize truncation errors.

Finite-size effects are particularly important in the simulation of flow through porous media where the numerical domain consists of many irregular pore bodies with converging-diverging geometries. In order to determine whether the finite-size effects are large, fine graining can be performed, meaning each voxel in the image contains multiple lattice sites for the numerical simulation. However, when this approach is used on a regular grid the computational expense can be significant.

### 2.2.3 Compressibility effects

LBGK model solves for the compressible Navier Stokes equations in the incompressible limit. Therefore, an accurate simulation of incompressible flow using this method is through low Mach and low density variations. Any deviation from these two requirements will lead to a so-called compressibility error [67].

In practice, when simulating the incompressible flows, the steady state macroscopic equations recovered from BGK are different from Navier Stokes equations by terms of spatial deviations of fluid density. This deviations are called compressibility effects. In addition pressures are related to the fluid density by $p = {c_s}^2 \rho$ where $c_s$ is the sound speed which is a constant. In incompressible flow of fluids, density should remain constant along flow paths which means that there would be no pressure gradient and is not meaningful for practical applications. This means that it enters slightly compressible region to solve pressure gradients. By replacing the pressure gradient by a uniform body force exact analytical solution of distribution functions of BGK for steady state flows is obtained [43].

According to Sterling and Chen [71], accuracy of LB for incompressible simulation of fluids

improves as lattice spacing and Ma decrease. Krüger et al. [39] also stated that LB is equivalent to Navier Stokes equations is the limit Ma and $\Delta$x tend to zero.

### 2.2.4 Permeability calculation

Permeability of a sample of porous media is defined as

$$K = -\mu \frac{\langle u \rangle}{\nabla P} \tag{2.9}$$

where $K$ is the permeability tensor of the porous medium, $\langle u \rangle$ is the average velocity of fluid, $\mu$ is the viscosity of the fluid, and $\nabla P$ is the dynamic pressure gradient in the fluid. In this work, permeability is computed in the same manner as in a laboratory experiment: an applied pressure drop is imposed and flowrate is measured (or vice versa). These two values, the fluid viscosity, and the sample dimensions are then used to compute permeability.

### 2.2.5 Tortuosity calculation

Tortuosity quantifies the straightness of trajectory that fluid must wind through the pore space as it passes along a linear distance of a porous medium. One definition of tortuosity is the square of the actual distance fluid travels in the domain to the length of the domain in the direction of pressure gradient:

$$T = (\frac{L_e}{L})^2 \tag{2.10}$$

where $L$ and $L_e$ are the length of the domain and the traveled distance by the fluids, respectively [11]. Nabovati and Sousa [55] presented a volume-averaged estimate of tortuosity from numerical pore-scale simulation results. They suggested

$$T = \frac{\sum_{i,j,k} u_{mag}(i,j,k)}{\sum_{i,j} |u_x|(i,j,k)} \tag{2.11}$$

where $x$ is the leading flow direction.

# Chapter 3
# Scaling performance of PALABOS

## 3.1 Parallelization study and scaling performance

In this study, the PALABOS (Parallel Lattice Boltzmann Solver) code, which is a parallelized LB code for solving flow problems and is available from the web address `www.lbmmethod.org/palabos`, has been used. All flow simulations were carried out on Louisiana Optical Network Initiative (LONI) resources.

Strong and weak scaling performance of the PALABOS code is tested for a 3D rectangular channel flow and shown in Figure 3.1. In these tests, file read/write or input/output operations of each processor are minimized.

The strong scaling test serves to determine how well the code performs with a problem of fixed size while increasing the number of cores. Figure 3.1a shows the wall clock time spent by processors versus the number of processors used for the computation in a log-log plot. In an ideal strong scaling test, the wall clock time is considered to diminish linearly as number of processors increase, giving a log-log plot with a slope of $-1$. The slope calculated for the code has a slope of $-1.05$.

In weak scaling, the work load assigned to each processor should remain constant. In other words, each processor has the same amount of work to do, such that no slowing should be observed for the ideal case and a log-log plot of computational time versus number of processors should have a slope of zero. In Figure 3.1b, log-log plot showed a slope of 0.04, which exhibits weak scalability. Based on these performance tests, the PALABOS code exhibits good scaling performance.

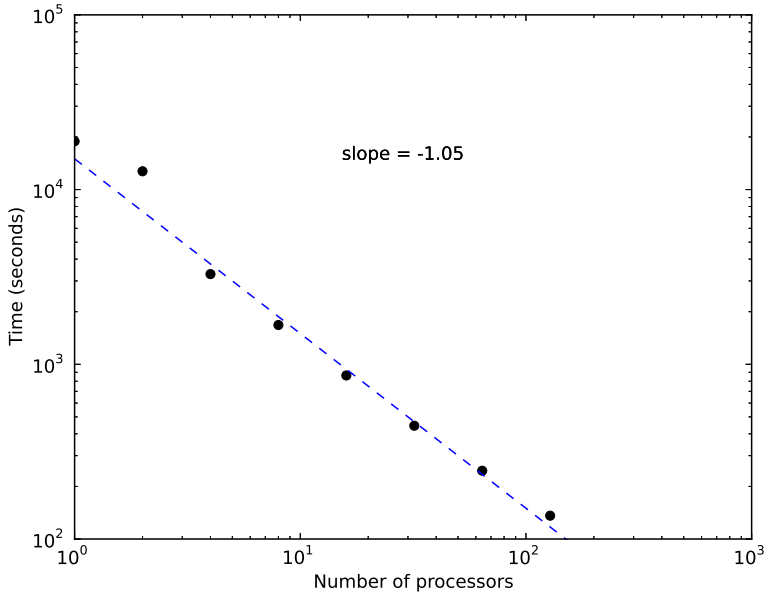


(a) Strong scaling

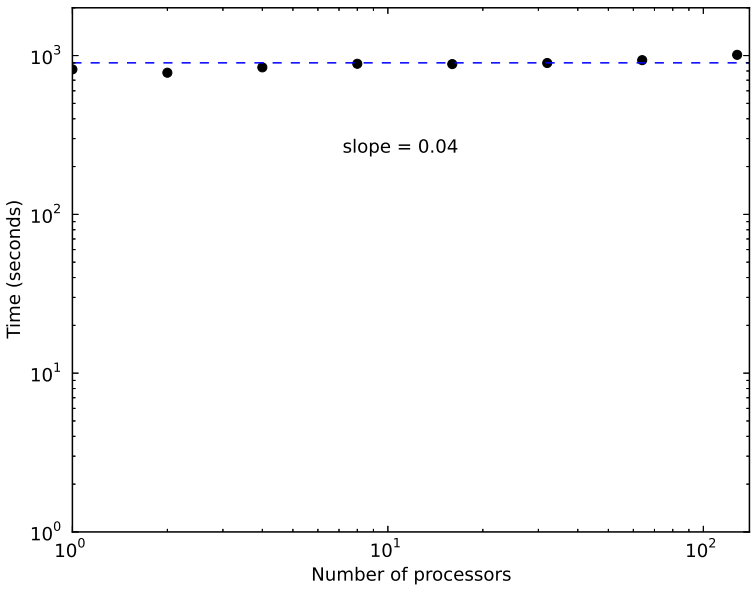


(b) Weak scaling

Figure 3.1: Strong and weak scaling study of PALABOS code

# Chapter 4
# Effects of image resolution and numerical resolution on computed permeability of consolidated packing

Image-based pore-scale modeling has become an important tool for studying fluid transport and other phenomena in porous media. Spatial resolution of the digital images used for modeling is critical not only because it dictates the scale of features that can be resolved, but also because for most techniques there is at least some relationship between voxel size in the image data and numerical resolution applied to the computational simulations. In this work we investigate this relationship using a computer-generated consolidated porous medium, which was digitized at voxel resolutions in the range 2-10 microns. These images, which are free of experimental and segmentation errors, are then used to compute permeability and tortuosity using lattice Boltzmann (LB) and finite elements methods (FEM). Results show how changes in computed permeability are affected by image resolution (which dictates how well the pore geometry is approximated) versus grid or mesh resolution (which changes numerical accuracy). For LB, the image and grid resolution are usually taken to be the same; we show at least one case where effects of grid and image resolution appear to counteract one another, giving the mistaken appearance of resolution-independent results. For FEM, meshing can provide certain attributes (such as better conformance to surfaces), but it also adds an extra step for error or approximation to be introduced in the workflow. Results show that performing grid coarsening on the FEM mesh caused a reduction in computed permeability, but in this particular case the effect is related to tightening of the pore space rather than loss of numerical accuracy.

Verification and validation of the LB code are performed on Body Centered Cubic (BCC) sphere packs and Castlegate Sandstone. For more detailed verification and validation, refer to Chukwudozie [11].

### 4.1 Image-Based Flow Simulation

A significant amount of past research has been performed to study and validate LB modeling of fluid flow in packed beds. Permeability studies in random sphere packs include [4, 8, 24, 33, 42, 49, 52, 54, 63, 66]. Additionally, Pan et al. [60, 61] and Stewart et al. [72] studied the effect of sphere size, spatial discretization, and fluid viscosity (relaxation parameter) on the computed permeability of random-sphere packs and Maier et al. [50] investigated flow of single-phase fluid through a column of glass beads.

Similarly, traditional CFD methods have been used to simulate flow in packed beds [3, 5, 15, 25, 45]. However, these techniques have not been as widely applied to imaged-based modeling (i.e., where the flow domain is obtained from microCT or similar 3D image data) as LB or network modeling [65].

### 4.2 Finite-element for pore-scale flow

While the finite element method is widely used for traditional CFD applications [41], its application to pore-scale flow simulations has been very limited. This is unfortunate because one of the main attributes of FEM is its ability to operate on unstructured meshes, which in turn allows local refinement to help address the wide variation in pore size and local velocity in a microscopically heterogeneous porous media. Some notable studies have considered relatively simple 2D geometries, or simple configurations of spherical particles in 3D [21, 23]. However, these approaches have not been applied in a more general way to image-based pore-scale modeling.

In this paper we solve the Stokes equations by FEM. A Bubnov-Galerkin approach is employed that uses a $P_2P_1$ or Taylor-Hood element. This choice of element implies that a linear approximation is assumed for pressure and a quadratic approximation is assumed for

velocity. Both pressure and velocity are defined at the vertices of the tetrahedral element, while the additional degrees of freedom required for the quadratic velocity approximation are added at the mid-points of each tetrahedral edge. Details of the numerical implementation can be found in Lane [41].

### 4.2.1 Meshing

The aforementioned reluctance to use FEM for image-based pore-scale modeling is largely related to the added challenge posed by mesh generation in a heterogeneous, interconnected flow domain. Part of the challenge is algorithmic: the nuts and bolts of mesh generation for these structures is not easy. However, this part of the problem is becoming less burdensome because of modern off-the-shelf meshing routines that operate directly on voxel images. The more difficult aspect of the problem is understanding and quantifying whether the mesh structure effectively captures the pore structure.

For image-based modeling, the digital image used as the basis for the structural model is already an approximation to the actual pore structure, which encompasses errors associated with image resolution, segmentation, and the inherent approximation when arbitrary surfaces are described using a voxel format (regardless of the resolution). When meshes are created from digital images, geometric and topologic parameters are altered further. An unstructured mesh typically has a different pore volume and surface area than the digital image that is used as the template. Connectivity can also change, especially in cases of corner-to-corner voxel connections, which even for the highest-quality images do not provide a definitive answer as to whether a physical connection existed in the original porous media. One can make an argument that an unstructured mesh is a better tool for characterizing the pore space than voxel data. For instance, surfaces of rounded grains or crystalline surfaces (that are not aligned with the principle voxel dimensions) can be captured by surface triangulations more effectively than by regular voxels. However, in image-based modeling the mesh is created from the voxel image rather than the original material, so this argument is not as compelling as it would be otherwise.

A voxel-based meshing approach described by Young et al. [80] has been built on a marching-cubes-type approximation of voxels on the void-solid interface, with a look-up table that splits those voxels intersected by a surface into tetrahedral elements. Away from the interface the approach has the ability to transition to hexahedral elements. The authors noted that their strategy resulted in an overestimate of surface area which can prejudice physics based simulations that depend on surface area. It was also mentioned that increasing the voxel to diameter ratio does not necessarily lead to an improvement in the approximation of surface area, which is consistent with the work of Lindblad [44]. In their voxel-based meshing approach the lack of adaptivity also leads to an extremely high number of surface elements, and essentially ties mesh resolution to the number of voxels. Although no physics was included in the study, element quality was assessed.

In our broader work, we have used two approaches to generating unstructured tetrahedral meshes from segmented image data. One is based on an in-house algorithm, which maps the porous media surface onto an existing unstructured mesh using a distance function. The second is a Computer Aided Design (CAD) based approach, which we have run using the commercially available Avizo software. Generally, our in-house algorithm gives more control over both local refinement and constraining specific parameters such as surface area and porosity. The CAD-based approach has performed better in terms of retaining connectivity present in the voxel image and conforming to the voxel boundaries. In this paper all results are based on the latter CAD-based approach, run using Avizo software. The meshes are transferred to an in-house data format prior to running the Stokes flow solver. However, this step is for convenience in applying boundary conditions for our flow solver; the change in data format does not alter the mesh structure.

### 4.2.2 Boundary condition

As noted in a recent investigation [62], the choice of appropriate boundary conditions for modeling pore scale flow is somewhat arbitrary. This can be attributed to a lack of detailed information at geometrically complicated inlet and outlet planes required to specify either

the velocity profile or pressure distribution as well as on the other four side walls.

As with the inlet and outlet, the side walls are generally arbitrary cuts through the pore space, and the boundary conditions for the hypothetical flow patterns into and out of these side walls (i.e., had the porous medium not been cut) cannot be known. Hence, the generally accepted approach is to consider the side walls of the flow domain as no-slip surfaces.

The no-slip boundary condition simplifies the problem, the tradeoff being confinement of the fluid and increased drag force acting on the fluid. Ideally, this is mitigated by considering large enough samples so that results become independent of boundary conditions. An argument can be made, in fact, that the no-slip condition on the side walls is the same boundary condition routinely applied in laboratory core flood experiments in which the confining sleeve is a no-flow and no-slip boundary condition along the external surface of the core. (Albeit, the physical dimensions of a laboratory core are typically an order of magnitude larger than the comparable tomography image.)

The alternative to the no-slip approach is to impose periodic boundary conditions. However, for real materials this requires mirroring or an artificial buffer region and either of these approaches has its own drawbacks.

For the inlet and outlet faces, the most common objective is to apply upstream and downstream pressures. This presents some difficulty because for FEM the direct boundary condition that can be applied is total stress. For inlet/outlet pores with high viscous stresses the pressure and the normal component of total stress can differ significantly. One way to address this problem is to add pipe-like sections upstream and downstream of the domain. This approach minimizes viscous stresses in the inlet and outlet (because of the large dimensions and slow flow relative to the pore dimensions) and thus allows application of a traction boundary condition as a substitute for the desired hydrostatic pressure condition. An approach similar to this has been used by [62, 81]. In studies of flow through sphere packs the extension of the computational domain prevented particles from intersecting the inlet and outlet planes which simplified both the implementation of boundary conditions and

the identification of boundary elements.

We have tested this same strategy previously and found no significant variation in predicted permeability based on the addition of inlet and outlet sections. Hence, our standard approach to pore-scale FEM modeling is to apply boundary conditions directly to the pore space on the inlet and outlet faces of the domain: total normal traction is set equal to the negative of the desired applied pressure. This approach avoids the added computational expense of modeling the inlet and outlet flow sections.

### 4.3 Samples

Computer-generated structures provide a number of advantages for testing pore-scale modeling algorithms. The most obvious advantage is the ability to fully control the pore structure. Another advantage related to image-based modeling is that geometric-based data (e.g., locations and sizes of spheres in a random packing) can be converted to voxel data at any desired image resolution without segmentation error.

Computer-generated sphere packings have been widely used to simulate granular materials. In some cases, unconsolidated sphere packs have been modified using procedures that mimic daigenetic processes, thus producing consolidated materials [7, 36, 83]. The simplest modification is to increase the sphere radii to allow sphere-sphere overlaps, which decreases porosity. In the current study, this approach was applied to random sphere pack with 1000 particles. The original packing had a cube-shaped domain size 1mm on each side. The sphere size distribution had a mean diameter of 100 microns and a standard deviation equal to 25% of the mean. The pack was fully periodic packing and had a porosity of 36.5%. The diameters of the spheres were then increased until the porosity was reduced to 14.5%.

To allow studies of image resolution, this artificially consolidated structure was converted into five voxel images, with voxel resolution varying from 2 microns (an image consisting of $500^3$ voxels), to 10 microns ($100^3$ voxels). At the best image resolution, as can be seen in Figure 4.1b the solid/void surfaces are smoother, while the voxelization clearly compromises

Table 4.1: Porosity ($\phi$) and specific surface areas ($S_v$) for different resolutions of the geometry.

| L/a | a($\mu$m) | $\phi$ (%) | $S_v$ (1/m) |
|---|---|---|---|
| 100 | 10 | 14.33 | 18374.80 |
| 200 | 5 | 14.34 | 19808.62 |
| 300 | 3.33 | 14.34 | 20298.41 |
| 400 | 2.5 | 14.34 | 20554.09 |
| 500 | 2 | 14.34 | 20705.89 |

the pore structure when the resolution is poor (Figure 4.1a). Porosity and specific surface areas of these images are tabulated in Table 4.1. Porosity variation is small, which reflects the fact that even at low image resolution the portions of solid voxels hanging into the pore space is somewhat offset by the portions of void voxels residing inside the spheres. Specific surface areas are calculated based on the algorithm presented in Thompson [75], and this value increases with increasing resolution but begins to converge at higher resolutions.

Figures 4.2a and 4.2b are histograms showing pore and pore-throat size distributions in the final structure. These values were obtained by creating a physically-representative pore network from the 2-micron-voxel data set. The resulting network is described by a variety of rigorous geometric measurements made in the pore space. These measurements include the size of maximal inscribed spheres in each pore and maximal inscribed spheres at the tightest point in connecting pore throats. Hence, this type of network data is ideal for characterization of the pore space.

Overall, the pore-throat size distribution, porosity, permeability, and image resolutions for this artificial system are reasonably consistent with values that would be expected for image-based modeling of moderate- to high-permeability sandstones (i.e., order hundreds of millidarcy). This higher permeability rock, in turn, is the most amenable to quantitative prediction of properties using digital imaging.

LB simulations are performed on a computer-generated sphere pack rather than a real microtomography image, which allows image resolution to be varied arbitrarily and without any segmentation error. The sphere pack was originally an unconsolidated packing of

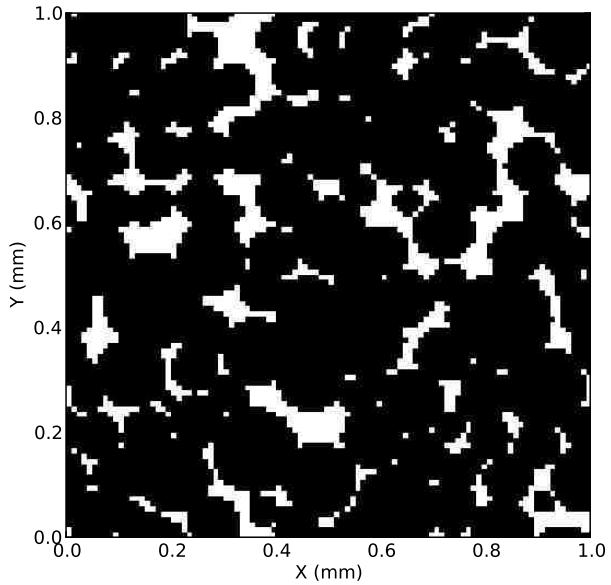


(a) Low-resolution image

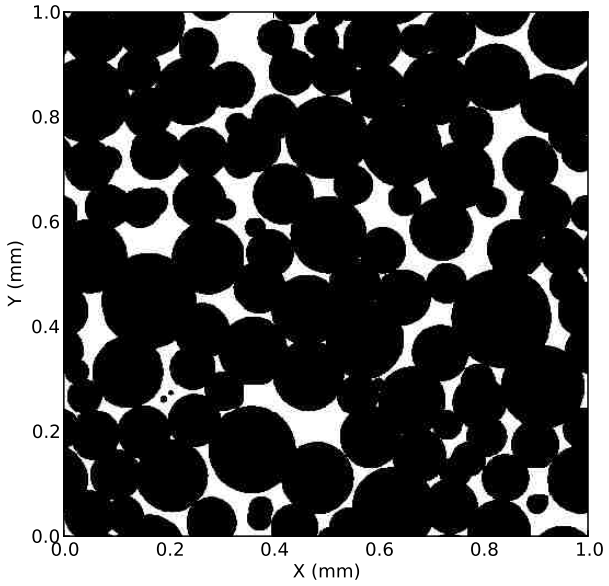


(b) High resolution image

Figure 4.1: Images of the random sphere pack with two different resolutions. (a) and (b) show the images with resolutions $a_0$ and $a_0/5$, respectively. Due to the higher resolution in (b), roughness of the staircase-like representation is more smoothed out compared to the low-resolution image.

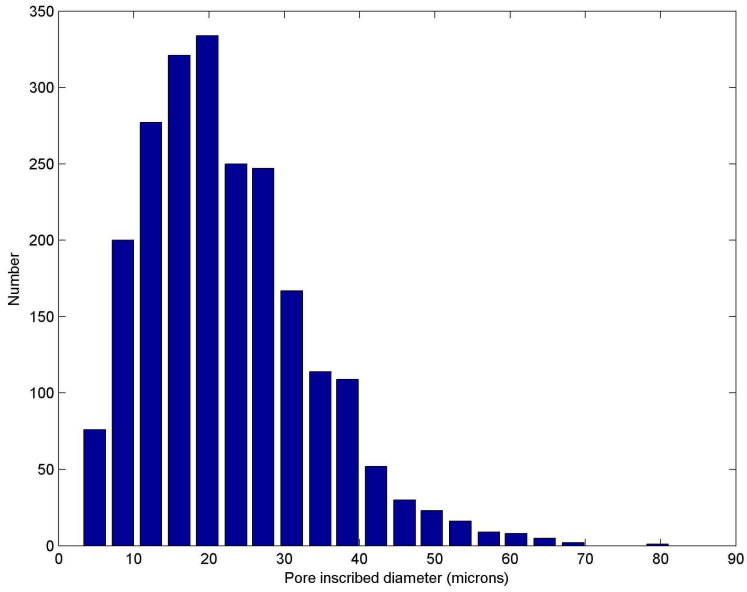


(a)

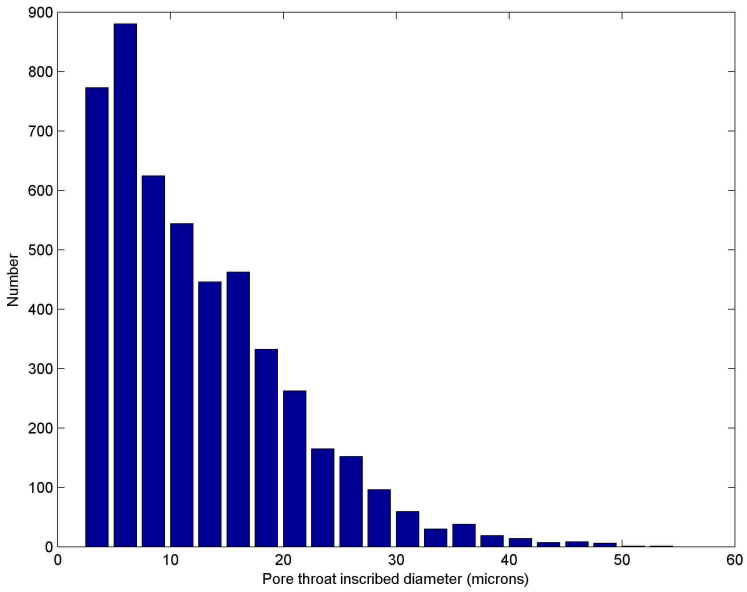


(b)

Figure 4.2: Pore and pore-throat size distributions for the computer-generated porous medium. Values are the diameters of maximal inscribed spheres in the pores (a) and at the tightest constrictions in the connecting pore throats (b). Measurements were made using a network-generation algorithm on the two micron digital image.

non-overlapping sphere, but for these simulations the sphere radii were increased to allow overlaps. This step creates a structure that mimics a consolidated material, which is of interest for oil and gas applications and represents a more challenging simulation than in sphere packings because of the smaller and less connected pore space. Permeability and tortuosity computations are made using both LB simulations (structured lattices) and FEM simulations (unstructured tetrahedral meshes). All FEM simulations presented in this research work were performed by Yijie Shen and Nathan Lane.

For clarification, terminology used in the remainder of the paper is the following. The term *image resolution* is used to denote the size of the voxels used to digitize the image. Poor image resolution implies larger voxels (i.e., a less clear picture of the pore structure); good quality image resolution means smaller voxels. The term *numerical resolution* is used to denote the characteristic spacing of the numerical discretization. For LB, this spacing is usually a fixed value (the spacing between each lattice node). For unstructured meshes it varies. In this paper we present unstructured mesh resolution by reporting the total number of elements. Since the domain size is fixed, this is an unambiguous quantity.

## 4.4 LB results

### 4.4.1 Image resolution

LB simulations were performed on the five data sets. Recall that the overall domain dimensions remain constant (a cube 1mm on each side), but voxel dimensions range from 10 $\mu m$ at the coarsest to 2 $\mu m$ at the finest resolution. In a typical LB approach the numerical lattice is coincident with the voxel grid. Hence, numerical resolution improves (i.e., grid spacing decreases) as image resolution improves.

Z-direction fluid flow is simulated for the five images. Flow is body-force driven and the lateral boundaries are no-flow boundaries. Periodic boundary conditions are applied at the inlet and outlet of the simulated samples. (The physical domains are periodic structures.) Calculated z-direction permeabilities of these images are plotted in Figure 4.3.

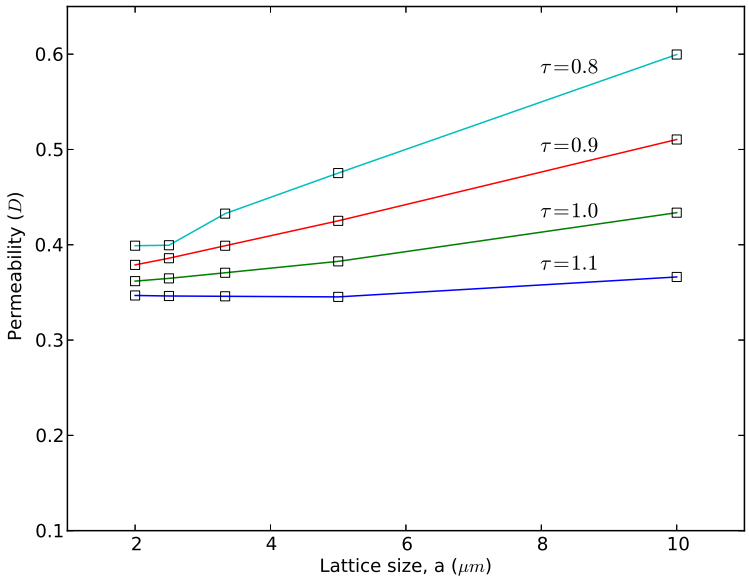


Figure 4.3: Calculated z-direction permeabilities for different lattice spacings and different relaxation times. For improved resolution (smaller lattice spacing), permeability decreases and permeability becomes less sensitive to relaxation time. For each resolution, calculated permeabilities are higher for lower relaxation times. For the relaxation time of 1.1, calculated permeabilities for all the image resolutions are similar, although microscale flow behavior is not consistent.

In general, permeability decreases as the image resolution and grid spacing improves (the two resolution effects are inseparable in the current set of simulations). The data are also broken down by relaxation time. Calculated permeability is more sensitive to relaxation time in the lower-resolution images: at 10 $\mu m$ resolution, permeability varies by 62%; at 2 $\mu m$, the variation is only 14%. These variations are due to both relaxation time dependence of finite-size effects and the no-flow boundary condition (bounce-back scheme) used in these simulations. In images with larger lattice spacings (lower resolutions), pore spaces are characterized by fewer grids, which makes both the position-dependence of no-flow boundaries and the finite-size effects more significant.

For the particular case of relaxation time equal to 1.1, the computed permeability is essentially constant over the range of image/lattice resolutions. However, despite these bulk permeability values being consistent, further investigation showed that the pore-scale flow

fields are significantly different from one another. This behavior is discussed further in the next section.

### 4.4.2 Grid refinement

In the above analysis (and many LB studies), it is not possible to separate the effects of improved image resolution and improved numerical resolution because the numerical grid is coincident with the voxel grid. Hence, to quantify this effect for the current data, we fix the image resolution and increase the numerical resolution by placing multiple lattice points within each voxel.

We use the lowest resolution image ($100^3$ voxels), and then perform simulations with $2, 3, 4,$ and 5 lattice nodes per linear voxel dimension. This makes the five different grid resolutions correspond to the same grid resolutions shown in Figure 4.3, but the pore structure does not change. In the subsequent reporting, we refer to these five simulations as 1X, 2X, 3X, 4X, and 5X, respectively.

Comparing the results of Figure 4.3 and Figure 4.4 shows that computed permeability is more sensitive to grid spacing alone than the combined effects of image resolution plus grid spacing that was discussed in the previous section. Specifically, for the fixed pore structure represented by the low-resolution image, computed permeability decreases by a factor of between 2 and 3 depending on the relaxation time. Furthermore, even at the smallest 2-$\mu m$ grid spacing, the results do not yet appear to have converged numerically. The effect is more pronounced for the smaller relaxation times.

To put this result in a more general context, consider the low-resolution versus high-resolution voxel images as two different porous media (rather than two different approximations to the same structure). In this hypothetical case, the voxel data are considered to be exact representations of two different pore structures defined by the low- and high-resolution images. Accordingly, one would expec them to have different permeabilities. Comparing the most reliable $a = 2$ results from Figures 4.3 versus 4.4 indicates that the true permeability of

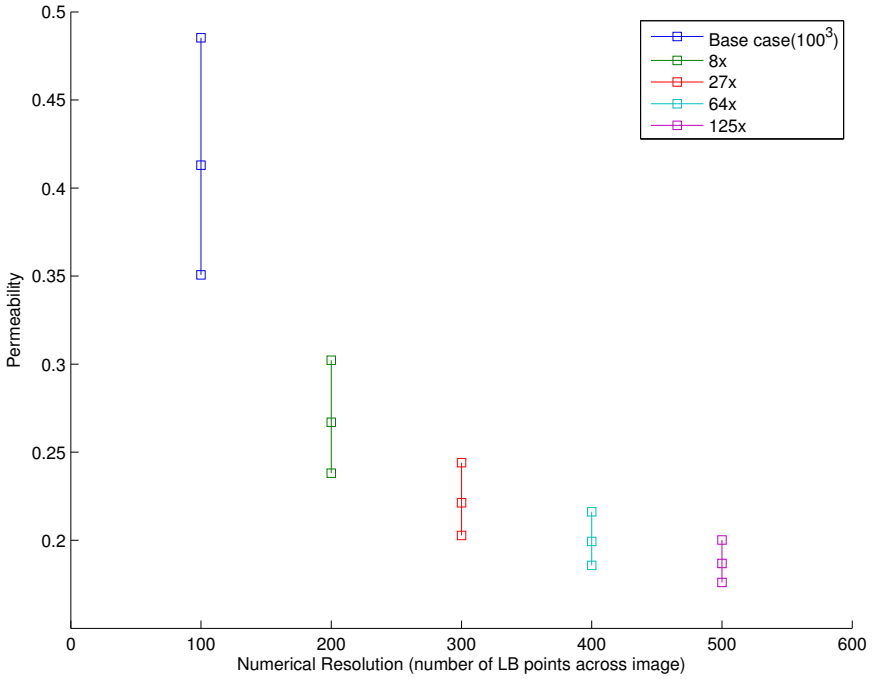


Figure 4.4: Calculated permeabilities versus lattice spacing for 1X, 2X, 3X, 4X, and 5X images for different relaxation times. For all relaxation times, calculated permeabilities decrease as grid spacing decreases. The results are more sensitive to grid spacing than when both image resolution and grid spacing vary.

the high-resolution structure is approximately twice the permeability of the low-resolution structure. This finding gives insight into the relatively flat $\tau = 1.1$ curve in Figure 4.3 that was discussed earlier. Specifically, as grid spacing decreases, the changing numerical resolution corresponds to lower computed permeabilities. However, as grid spacing decreases the physical flow structure also changes, and in this particular case the physical change in the voxel structure leads to increased permeability. The two effects appear to essentially offset one another for the $\tau = 1.1$ case.

These observations are significant because permeability is often used as a surrogate measure of confidence/quality in image based modeling. (For instance, validation is often based on permeability agreement with an experimental value, consistency in permeability for two different image resolutions, or permeability independence versus numerical resolution). The $\tau = 1.1$ result in Figure 4.3 is a case that would misleadingly suggest convergence in the computed permeability values.

Table 4.2: Calculated z-direction permeability and tortuosity of grid-refined and resolved samples for different relaxation times

| Lattice spacing a ($\mu$m) | $\tau$ | $100^3$ image with varying lattice spacing | | Images with varying voxel size | |
|---|---|---|---|---|---|
| | | $K_z$ | T | $K_z$ | T |
| 10 | 1.1 | 0.37 | 1.58 | 0.37 | 1.58 |
| | 1.0 | 0.43 | 1.58 | 0.43 | 1.58 |
| | 0.9 | 0.51 | 1.57 | 0.51 | 1.57 |
| | 0.8 | 0.60 | 1.57 | 0.60 | 1.57 |
| 5 | 1.1 | 0.24 | 1.65 | 0.34 | 1.60 |
| | 1.0 | 0.26 | 1.65 | 0.38 | 1.59 |
| | 0.9 | 0.30 | 1.65 | 0.42 | 1.59 |
| | 0.8 | 0.34 | 1.66 | 0.47 | 1.59 |
| 3.33 | 1.1 | 0.20 | 1.67 | 0.35 | 1.6 |
| | 1.0 | 0.22 | 1.67 | 0.37 | 1.59 |
| | 0.9 | 0.24 | 1.67 | 0.40 | 1.59 |
| | 0.8 | 0.26 | 1.66 | 0.43 | 1.58 |
| 2.5 | 1.1 | 0.18 | 1.68 | 0.35 | 1.61 |
| | 1.0 | 0.20 | 1.67 | 0.36 | 1.60 |
| | 0.9 | 0.21 | 1.67 | 0.39 | 1.60 |
| | 0.8 | 0.23 | 1.67 | 0.41 | 1.60 |
| 2 | 1.1 | 0.17 | 1.69 | 0.35 | 1.61 |
| | 1.0 | 0.18 | 1.69 | 0.36 | 1.61 |
| | 0.9 | 0.19 | 1.69 | 0.38 | 1.60 |
| | 0.8 | 0.21 | 1.68 | 0.40 | 1.60 |

Tortuosity and z-direction permeabilities are tabulated in Table 4.2. Tortuosities are less sensitive to changes of relaxation times in comparison with permeabilities. Tortuosity also remains relatively constant for different image resolutions. However, as numerical resolution is changed in the $100^3$ image, tortuosity varies between 1.57 and 1.69, which indicates a more tortuous path that fluids take to flow through the low-image-resolution structure.

Figures 4.5a and 4.5b show velocity streamline plots at the same grid spacing, but for the high- and low-image resolutions respectively. As can be seen in these figures, poor image resolution can lead to lost connections as well as a coarser representation of surface structure, both of which contribute to the differences in permeability when comparing equal grid spacings but different image resolution.

Figures 4.6a and 4.6b depict normalized $z$-direction velocity ($v_z/\langle v_z \rangle$) in the same location

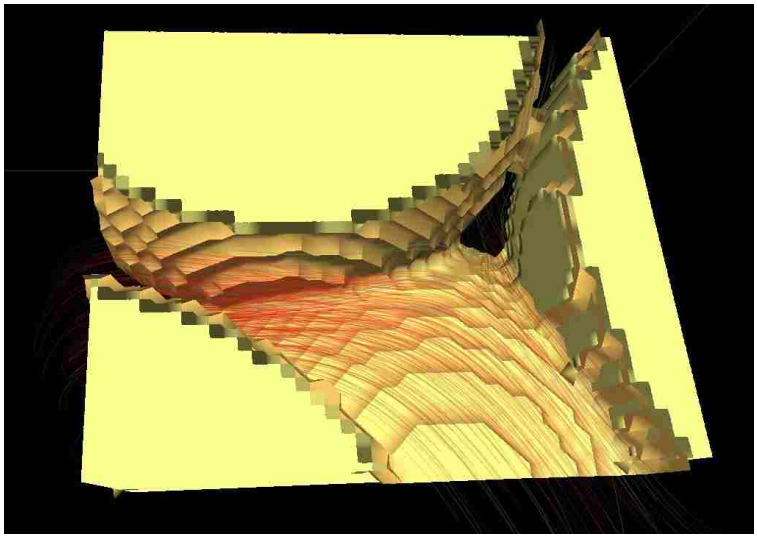

(a)

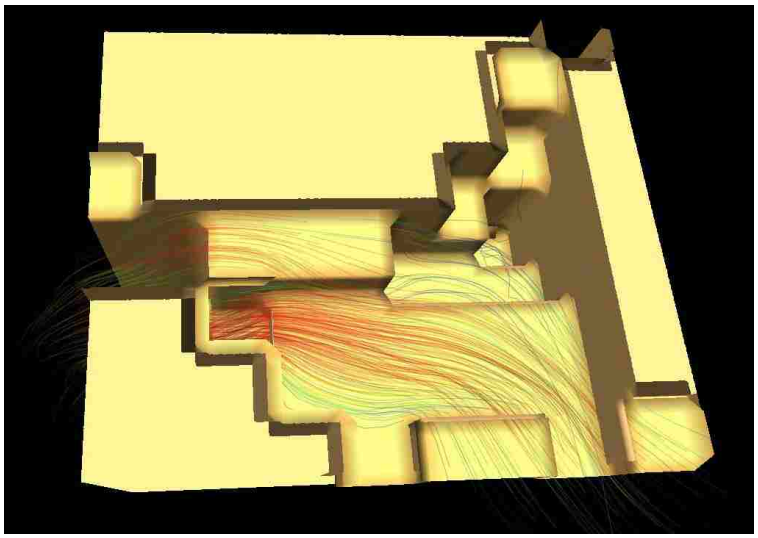

(b)

Figure 4.5: Velocity streamline plots from the highest image resolution data set (a) and the 5X sample (b). Numerical grid spacing in the two cases are the same, but image resolution results in a significant difference in resolved pore structure.

in the $xy$ plane, but for the high-resolution versus 5X simulation respectively. Velocities are significantly higher than the average because this region connects two pores via a narrow pore throat. Plots of velocity profiles in these two images for different relaxation times are shown in Figures 4.6c and 4.6d. The effect of the relaxation time on the velocity profiles is not significant.

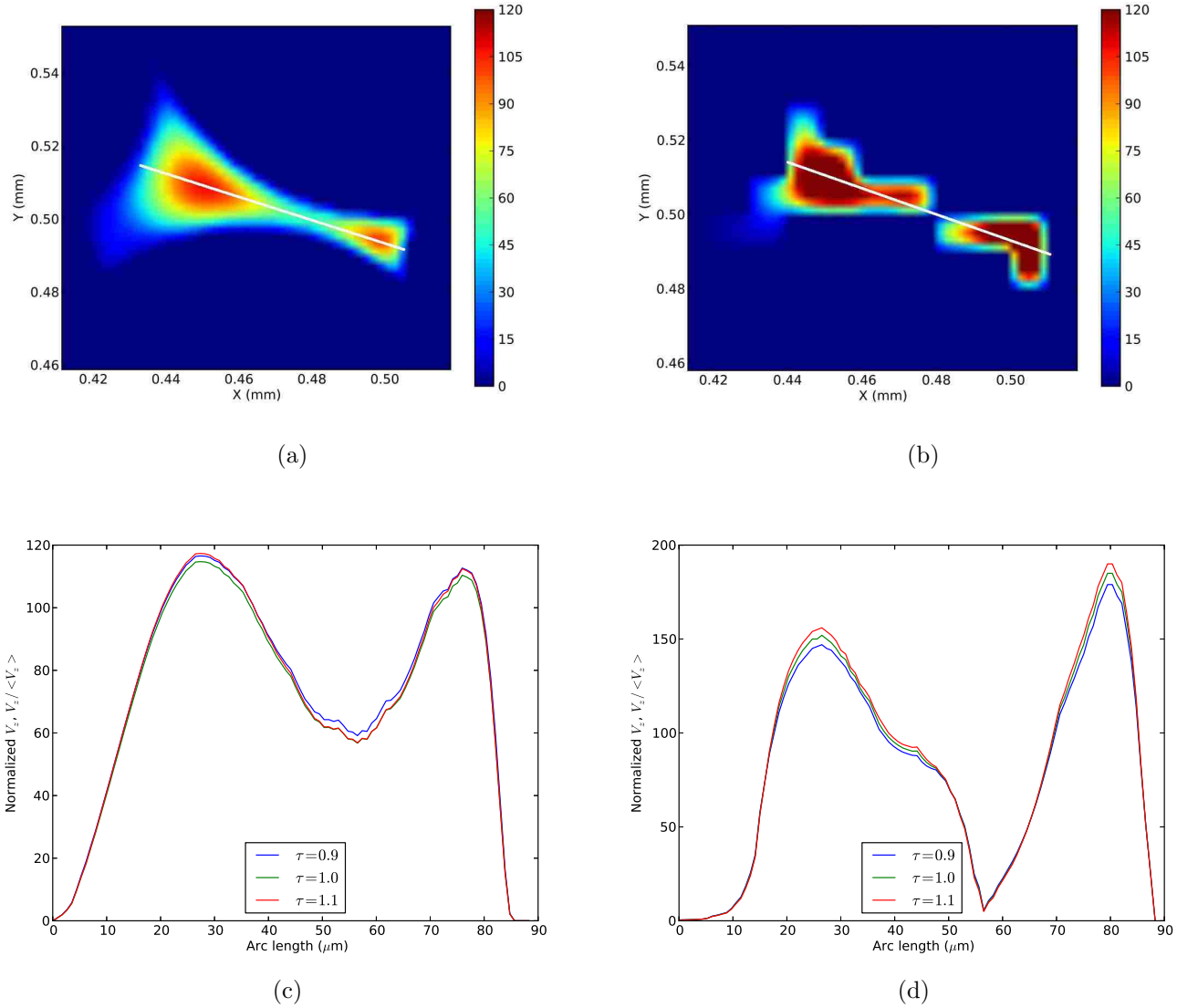


Figure 4.6: Contour plots of normalized z-direction velocity, $v_z/\langle v_z \rangle$ in (a) the highest-resolution and (b) the 5X simulations. On the bottom row are normalized velocity profiles from the two upper images along the line shown, for the highest resolution and the 5X simulations, for different relaxation times.

## 4.5 FEM results

The image- versus numerical-resolution issues are quite different when using FEM for pore-scale modeling because of the mesh generation step. On one hand, the FEM (or other mesh-based methods) has the disadvantage of having the additional meshing step prior to simulation. This makes the mesh two steps removed from the original porous media structure,

meaning it will be affected by any resolution, imaging, or segmentation errors contained in the voxel data, but may have additional geometric or topologic errors associated with mapping the voxel structure onto the unstructured mesh. On the other hand, the ability to use an unstructured mesh allows image resolution and numerical resolution to be decoupled more effectively than with lattice based techniques. Other advantages include the ability to employ local mesh refinement and the ability to create smooth surfaces, even in cases where a fixed-resolution, non-smooth voxel image is the template. FEM results for comparative analysis were provided by Prof. Karsten Thompson's Poresim research group.

### 4.5.1 Image resolution

Adjusting parameters in the mesh generation algorithms allows mesh resolution (elements per volume) to be controlled more-or-less independently of the underlying image resolution. This attribute implies that improving image resolution does not force the size of the computational problem to increase. This idea is illustrated for the current problem in Figures 4.7, which shows the same section of an image at two resolutions. The poor resolution case is from the 10 micron data set. The high resolution case is from the 2 micron data set. The meshes overlaying each voxel image contain similar sized elements, which qualitatively highlights how element size can be decoupled from the voxel size.

Figure 4.8a shows computed permeability as a function of number of elements in the mesh. Results are shown for all five voxel resolutions. Meshes with the largest number of elements tend to conform to the voxel-based pore structure most accurately and will also minimize numerical error. For the best image resolution and the largest number of elements, the permeability agrees well with the two-micron resolution results from the LB simulations. Also, as the image resolution decreases but numerical accuracy remains high, permeability decreases by a factor of approximately two, which is consistent with the LB simulations.

For fixed image resolution and decreasing number of elements, permeability also decreases. Notably, this trend is opposite what was observed in the LB simulations for the low image-

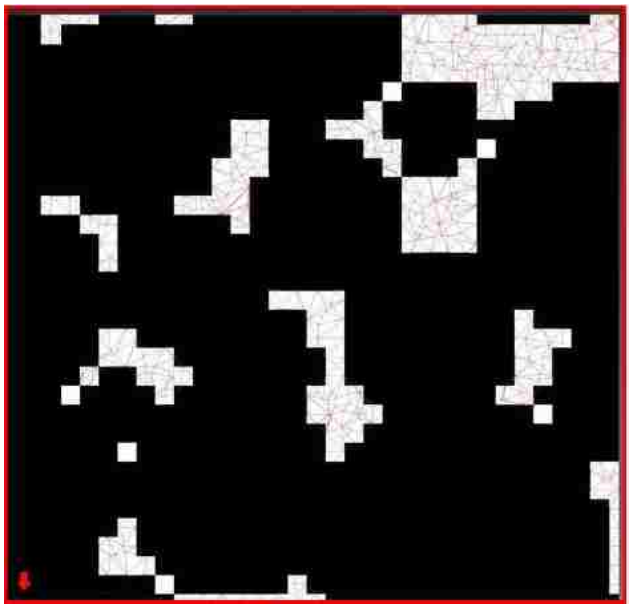

(a)

(b)

Figure 4.7: (a) Low resolution voxel image (10 microns) with overlaying mesh. (b) High resolution voxel image (2 microns) with overlaying mesh. Average element size and number of elements remain similar despite the drastic difference in image resolution.

resolution data set. Further insight into the FEM behavior is provided by Figure 4.8b, which is a plot of effective porosity versus element resolution. (Effective porosity is the mesh volume divided by the total volume. This mesh-based porosity generally differs somewhat from the voxel-based porosity because the unstructured mesh is a different approximation

of the void structure compared to the voxel pore space.) For the meshing algorithm used in this study, coarsening of the mesh causes a simultaneous decrease in mesh volume and effective porosity. Hence, the decrease in permeability with decreasing number of elements is due at least in part to the fact that flow is being modeled in a tighter pore space.

Before leaving this topic, we note that the change in permeability could also be tied to numerical accuracy in addition to the porosity effect. A series of tests were conducted in which the surface triangulation (on the interior grain surfaces) was not allowed to change, while the number of elements in the interior mesh was varied by more than an order of magnitude. This test allows mesh resolution to vary while porosity and the meshed surface structure to remain fixed. In contrast to the Figure 4.8a results, the fixed-porosity test showed little change in permeability as a function of number of elements over the range tested. This result is also consistent with tests in a variety of ducts, which shows that modeling viscous flow using the $P_2P_1$ element results in excellent accuracy even for few elements across the duct width. These latter results can be found in Lane [41].

### 4.6 Relative errors of LBM and FEM velocity fields

In this work, a point-by-point comparison of the calculated velocity fields of FEM and LB is done. Velocity fields of FEM simulations are interpolated using the shape functions to calculate the velocities at each lattice point. Velocities at each point are then normalized by the average velocity in the domain. Errors of the normalized z-direction velocity at each lattice point of LB and FEM simulations at $500^3$ voxels are calculated using Equation 4.1:

$$\Delta V_{z,i} = V_{z,i}^{LB}/\langle V_z^{LB}\rangle - V_{z,i}^{FEM}/\langle V_z^{FEM}\rangle \tag{4.1}$$

where $\Delta V_{z,i}$ is the difference between the normalized calculated z-direction velocity of LB and FEM for the grid $i$, $V_{z,i}^{LB}$ and $V_{z,i}^{FEM}$ are the calculated z-direction velocity of LB and FEM for the grid $i$, respectively, and $\langle V_z^{LB}\rangle$ and $\langle V_z^{FEM}\rangle$ are the calculated average z-direction velocity of LB and FEM, respectively.

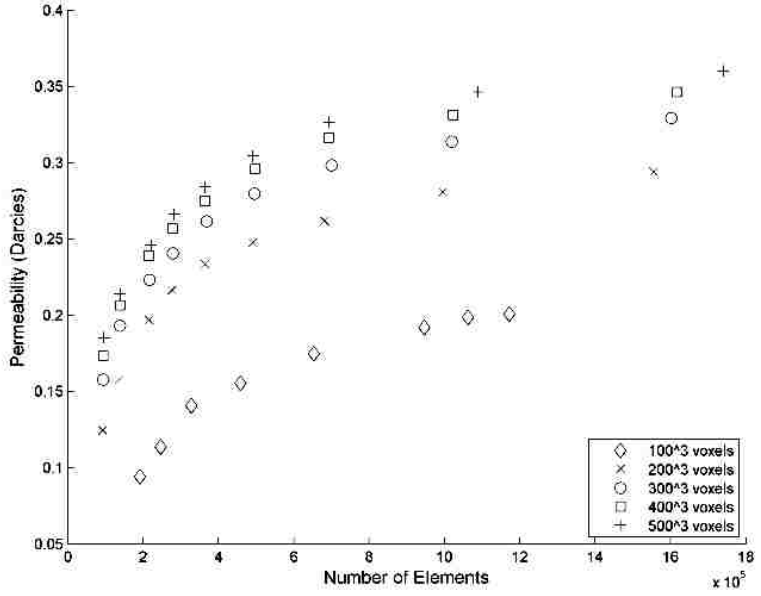


(a)

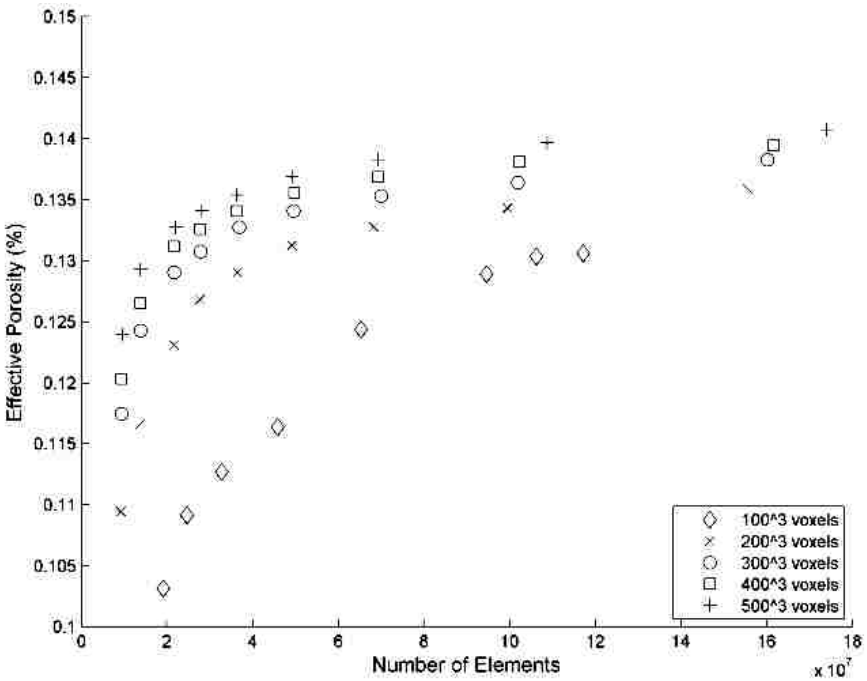


(b)

Figure 4.8: (a) Permeability versus number of elements for five different underlying image resolutions; (b) Effective porosity based on mesh volume versus number of elements for the same five image resolutions.

Figures 4.9 show a contour plot of the calculated z-direction velocity of FEM simulations of a xy cross-section of the $500^3$-voxel image and its corresponding error values contour plot of the two approaches. By inspection of these plots, one can see that FEM calculates higher velocity values than LB for regions with higher velocities.

Two regions from the 2D xy cross-section shown in Figure 4.9a are chosen to in order to compare the calculated velocity profiles of FEM and LB. In the first area, normalized z-direction velocities of FEM and LB along the horizontal line (shown in Figure 4.10a ) are plotted in Figure 4.10b. This figure shows that the differences between the velocities are higher at the regions away from the void-grain interfaces. At the center of the line where velocity reaches to its maximum value, predicted velocities of FEM are almost 11% higher than LB. In the Figure 4.10d, normalized z-direction velocities of the two approaches are plotted along the vertical line shown in the Figure 4.10c. Contrary to the region shown in Figure 4.10b, in this region, LB velocities are slightly higher than FEM. At the mid points on the line, predicted velocities of LB are around 16 % higher than FEM. It should be noted that normalized velocity values in the region shown in Figure 4.10b are higher than in this region.

Figure 4.11 shows the histogram of the relative error values of the normalized z-direction velocities of the two approaches of the highest resolution image. The mean value of the error is zero and the standard deviation is 74%. The frequency of the error values between -0.75 and 0.75 is more than 96% of the total number of the nodes (it should be pointed out that more than 85% of the nodes are located in the solid phase and therefore, both methods give zero velocity and error values).

Histograms of the normalized z-direction velocities predicted by the two methods for the $500^3$-voxel image are shown in the Figure 4.12. FEM seems to predict higher velocity magnitudes (both in positive and negative directions) and shows a wider range of velocity values compared to LB results. Permeability values predicted for both approaches for this image are close to one another. Although the leading direction velocity ranges and magnitudes are dif-

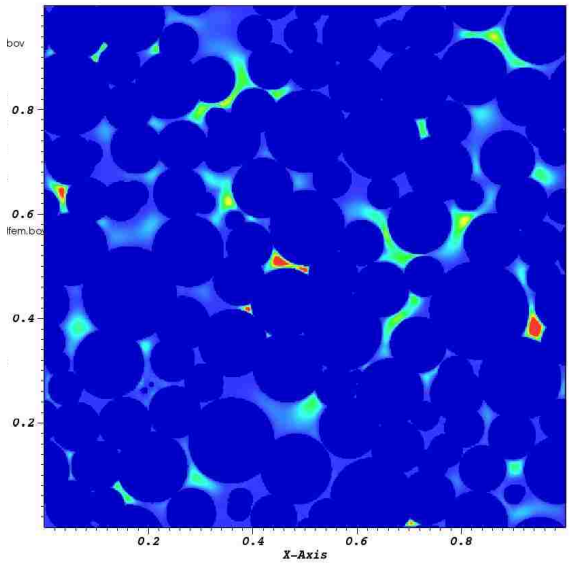


(a)

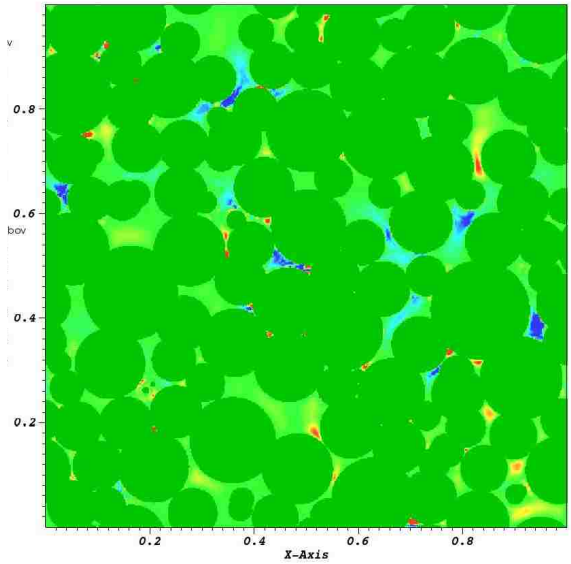


(b)

Figure 4.9: Z-direction velocity contour plot of the FEM simulations for a xy cross-section of the $500^3$-voxel image and its corresponding error values contour plot of the two numerical approaches. (a) A contour plot of the normalized z-direction velocity of the $500^3$-voxel image. (b) Relative errors of the z-direction velocity calculated at each node for two approaches. In (b), one can see that FEM estimates higher values of the velocities for regions of higher velocities.

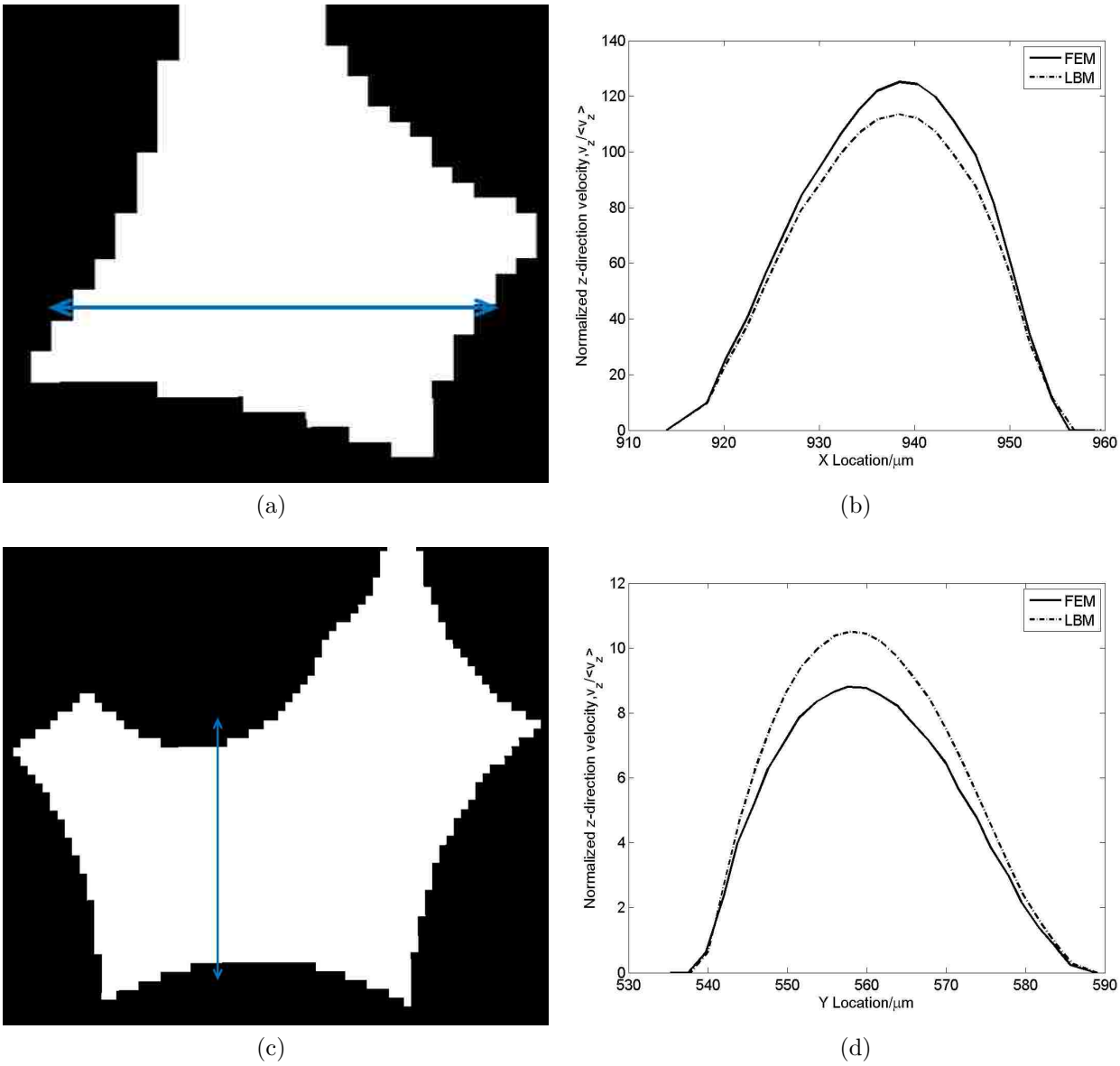


Figure 4.10: Two regions on the z-direction velocity contour plot of the Figure 4.9a and the predicted velocity profiles along the blue lines of the two approaches. (a) Shows a region of high velocity values. As can be seen, the predicted velocity values of FEM are higher than those predicted by LB. (b) shows an area with relatively lower velocity values compared to (a). (d) shows the predicted velocity profiles along the vertical blue line for the two methods. Predicted velocity values by LB are larger than those of FEM in this region.

ferent, they sum up to give similar values (since their summations are used for permeability calculations).

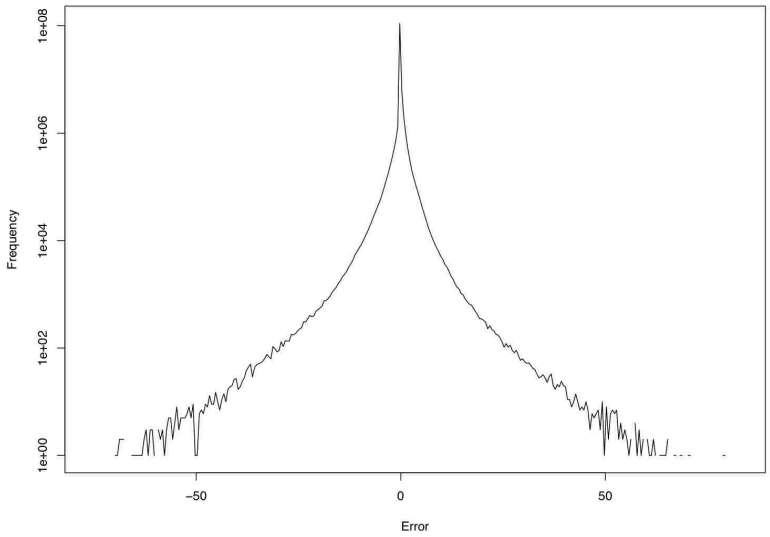


(a)

Figure 4.11: Histogram of the relative error values of the normalized z-direction velocities of the two approaches of the highest resolution image. The mean value of the error is zero and the standard deviation is 74%.

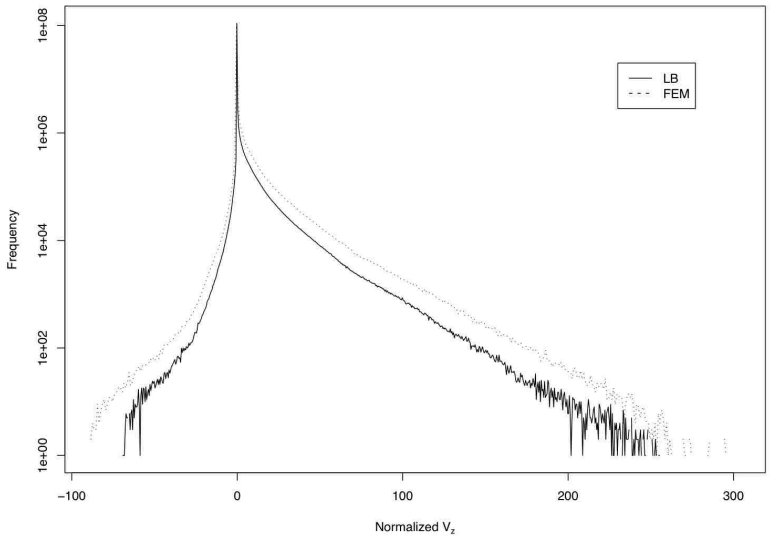


(a)

Figure 4.12: Predicted z-direction velocity histograms for the two methods for the highest resolution image. FEM seems to predict higher values for both positive and negative z-direction velocities. The regions with higher z-direction velocity magnitudes are also higher for FEM than LB.

### 4.7 Discussion

LB and FEM results converge to similar permeability values of approximately 0.35 Darcy when both image resolution and numerical resolution are highest. As image resolution becomes coarser, the pore structure and topology are compromised by the larger voxels. Evidence from both simulation methods shows that the lower-quality images have a correspondingly lower physical permeability (i.e., the actual permeability of the compromised structure). However, the situation is more complex when image resolution and numerical resolution both come into play (as is usually the case in practice).

When the LB lattice was taken to be the same as the voxel grid, the computed permeability decreased as image/lattice resolution improved. Additionally, the coarser-resolution images made the simulation results more sensitive to the choice of relaxation parameter.

For the choice of relaxation parameter $\tau = 1.1$, permeability is relatively insensitive to image/lattice resolution. However, we show that this insensitivity is an artifact: a combined effect of 1) the true permeability of the voxel structure increases with improved image resolution (because of geometric and/or topologic changes associated with the approximated pore structure) and 2) the computed permeability decreases with improved image resolution (because of better numerical accuracy). The fact that these two effects can offset one another is important to consider because permeability is often used as a surrogate measure to confirm the quality of results in image-based modeling.

FEM simulations require a separate meshing step, which allows numerical resolution to be more independent of the image resolution than with typical LB simulations. However, the numerical and image resolution cannot be separated completely because the mesh is usually generated from a voxel-based digital image, and poor resolution in the image data thus impacts the ability of the mesh to capture the pore structure, even if a large number of elements is used.

In the results shown here, when a large number of elements was used, permeability de-

creased as image resolution became worse. This behavior reflects structural changes in the voxelized pore space as image quality decreases. For the highest quality images (2 micron resolution), computed permeability decreased as the mesh was made coarser. It appears that this effect is associated with a constriction of the pore space as the mesh is coarsened more so than loss of numerical accuracy. If the surface structure of the mesh is able to accurately capture the pore structure, then the $P_2P_1$ element is able to give excellent results even with a relatively coarse mesh.

Further investigations show that despite predicting similar values of permeabilities in the both numerical methods, their velocity profiles in the pores are different. This could be of particular significance for determining the non-Darcy flow parameter in porous media, where local acceleration/deceleration are of importance.

# Chapter 5
# Stress dependent permeability and $\beta$-factor calculation

In the life of a producing reservoir, the net effective stress around completions from the reservoir ( in-situ stress minus fluid pressure) increases due to the fluid pressure depletion. Properties of the reservoir rock (permeability, porosity, and non-Darcy flow parameter), which are dependent on the pore space geometry of the porous rocks, can change as a result of this change. For selecting the best proppant for a stimulation operation, non-Darcy factor is one of the main factors that should be taken into account.

At regions close to the wellbore and inside a hydraulic/natural fracture, changes of the pressure due to fluid production/injection are higher than the regions away from the wellbore. Higher pressure changes can cause higher effective stress alterations in these regions. In an unconsolidated porous media such as in propped hydraulic fractures, these alterations in effective stress manifests itself in the topology alteration of the medium by either rearranging the grains (usually dominant in the unconsolidated porous media such as proppants in a hydraulic fracture) or fracturing of the grains. The grains (or pore space) rearrangement alters the porosity and topology of the pore space. The fractured grains may shift to the pores and decrease the pore spacing. These effects usually decrease the permeability of porous media and causes fluid to be pushed through narrower pore spaces and the inertial flow seems to be more significant.

According to Vincent et al. [77], non-Darcy flow parameter of the proppant packs are affected by the initial permeability and porosity of the proppants, proppant angularities,

size distributions of the proppants, heterogeneities, and surface roughness

Davies and Davies [14] summarized the stress-related alteration of properties of unconsolidated porous media. Changes of grain packing changes the topology of pores in the porous rock are attributed to grain slippage and rotation, changes in grain shapes, and grain fracturing.

### 5.1 Samples

Samples of porous media made of proppant grains under different stresses are provided to us by Prof. Clint Willson's research group. Imaging and segmentation of the proppant pack images are performed by Paula Sanematsu and Seth Bradley. The objective is to calculate permeability and $\beta$-factor of each stress condition using LB. In the simulations on the proppant samples, the low-resolution effects (both finite-size effects and relaxation-time dependence of the no-flow boundaries) on the simulated results are not significant; the pores bodies and pore throats of proppants are large enough and are several voxels thick. Proppants are located at the mid-section of a cylinder and are sandwiched by a different type of porous medium (Berea Sandstone). In order to be able to simulate the fluid flow through proppant samples, a region consisting only the proppants is cut from the original samples and all the simulations are run on them.

For the calculation of the $\beta-$factor of the proppant pack at different stress conditions, flow simulations at relatively high Reynolds number (criteria for onset of the non-Darcy flow is addressed in Chapter 2) and then $\beta-$factor can be calculated using an rearrangement of the Forchheimer equation.

As is addressed in Chapter 2, one of the drawbacks of the LB method is the compressibility errors. Applying a high pressure gradient (high body force) can result in a continuity error than can grow in each time-step and break down the simulation. The original simulations on the packing are done on the original geometry ($300^3$ voxels) and the maximum Reynolds number that is achieved was close to 10. Number of voxels are increased as numerical

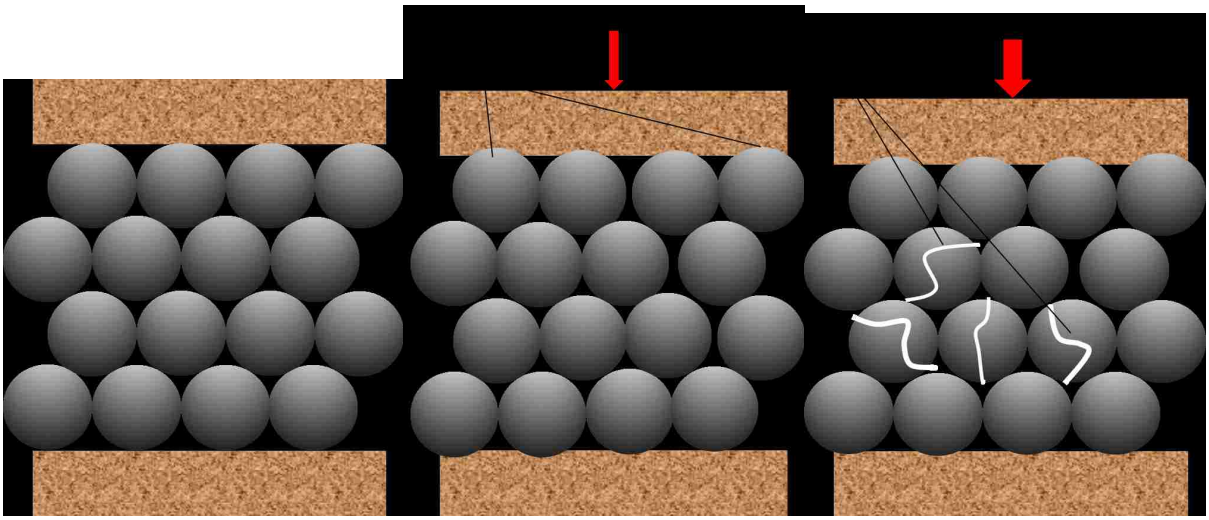

(a) (b) (c)

Figure 5.1: Schematic cross-sections of proppants under different confining stresses. At confining stresses below which grain crushing occurs, the height of the column consisting the proppants decreases due to the rearrangement (slippage) and deformations of the proppant grains, and the embedment of the proppants to the surrounding porous media. At high confining stress, crushing of grains may occur along with the generation of the intragrain fractures. The latter can cause generations of narrower flow pathways and therefore, local high-velocty regions that increase inertial flow parameters.

resolution is increased by sub-dividing each side of the voxels by 2 (thus increasing the total number of the voxels by factor of 8) and Reynolds number value of almost 20 could be achieved. Numerical resolution of these new samples are 6.8 micrometers.

Figure 5.1 shows the effect of increasing stress on the topological structure of a cross-section of the proppants. As can be seen, as the confining stress increases, grains pushed together and also pushed into the surrounding media, which results in the change in topology of the samples.

## 5.2 LB simulation results

From the proppant sample at different confining stresses, subsets of $300^3$ voxels from the center of packing at a specified stress are selected for running flow simulations. Flow in all three directions are simulated and permeability, $\beta$-factor, and tortuosity are calculated. For all simulations, ten layers of void voxels are added at each side of the samples in order to

make them periodic. Body force approach, which is an alternative to specifying pressure values at the inlet and outlet of the domain is utilized (see section 2.2.1 for more details). Periodic boundary conditions in all directions are used and body, however, body force is not exerted on these added layers. As it is expected, apparent permeability decreases as the fluid velocity increases. Furthermore, for higher stresses, since pores are tighter, permeability is lower.

Figures 5.2, 5.3, 5.4, and 5.5 show the velocity magnitude contour plots of the proppant packing under 0 , 4000, 12000, and 20000 psi confining stresses. For comparison, pressure gradients exerted for the simulations are normalized. In other words, velocity magnitudes in the lower Reynolds number image are multiplied by the ratio of the exerted pressure gradients of the higher velocity image to the lower one. For all the the confining stresses, the contour plots for higher flow velocities (higher Reynolds numbers) have more regions with higher velocities (with hot colors) compared to the lower velocities. This is because for higher flow velocities, the fluid is pushed through narrower pore spaces and therefore, have higher local velocities in these regions.

Figure 5.6 depicts the changes of apparent permeability with changes of Reynolds number for the packing at different stresses. For low flow rates, apparent permeability and absolute permeability of the porous media are almost the equal. Therefore, we can have an estimate of the permeability of the medium. As we can see, permeability of the packing decreases as confining stress on the packing increases. For lower stresses (before grain crushing occurs) most of the permeability reductions are due to the grains sliding and rearrangement. Permeability reductions are more significant for the highest confining stress (20 Kpsi) due to grain crushing and generation of the intragrain fractures. $\beta$-factor can be calculated from the slope of the changes of inverse of apparent permeability versus pseudo-Reynolds number. As confining stress increases, $\beta-$factor increases due to the fact that for higher confining stresses, the flow pathways are narrower compared to those in lower confining stresses. From 12Kpsi to 20 Kpsi, the change in $\beta-$factor is more substantial due to the fact that the

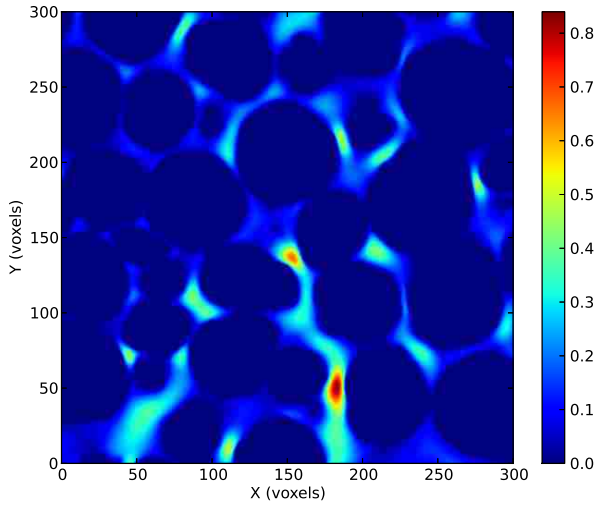


(a)

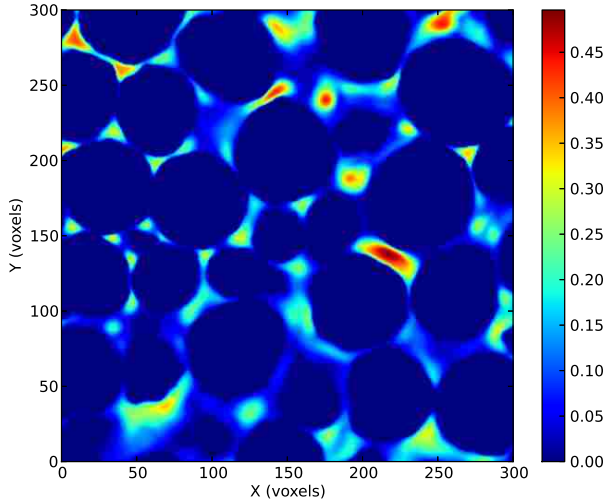


(b)

Figure 5.2: Normalized velocity-magnitude profile of a xy-cross section of the proppant pack under no confining stress. (a) shows the velocity magnitude profile for Reynolds number of 0.028 ($F_0 = 6.15E\text{-}04$) and (b) shows the profile for Reynolds number of 20.6 ($F_0 = 4.50E\text{-}01$)

grain fracturing generates narrow pathways that fluids are pushed through at high pressure gradients.

Figures 5.7a depict the inverse of apparent x-direction permeability versus pseudo Reynolds number. Based on Forchheimer equation, plot of inverse of permeability versus pseudo-Reynolds number will give a slope equal to $\beta$-factor and an intercept of Darcy permeability.

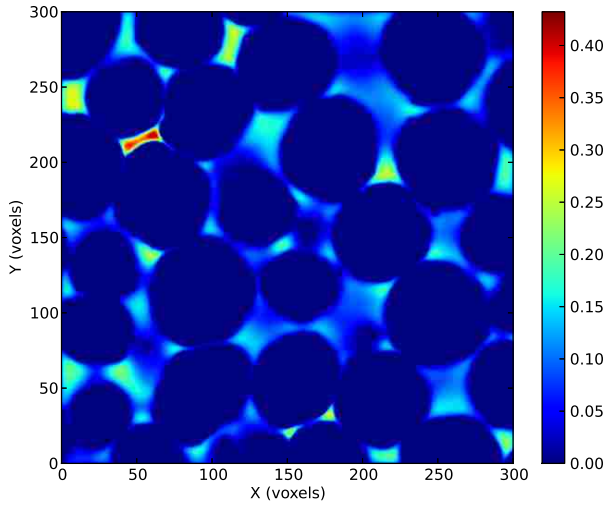


(a)

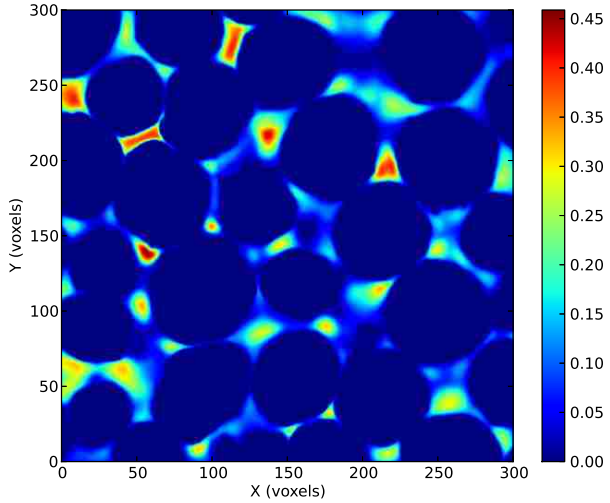


(b)

Figure 5.3: Normalized velocity-magnitude profile of a xy-cross section of the proppant pack under 4000 psi confining stress. (a) shows the velocity magnitude profile for Reynolds number of 0.027 ($F_0$ = 6.25E-04) and (b) shows the profile for Reynolds number of 19.7 ($F_0$ = 4.57E-01)

Calculated permeability tensors for each stress condition are shown in Table 5.1. Calculated permeabilities and $\beta-$factor for each stress condition for all the flow directions are tabulated in Tables 5.2 and 5.3, and 5.4.

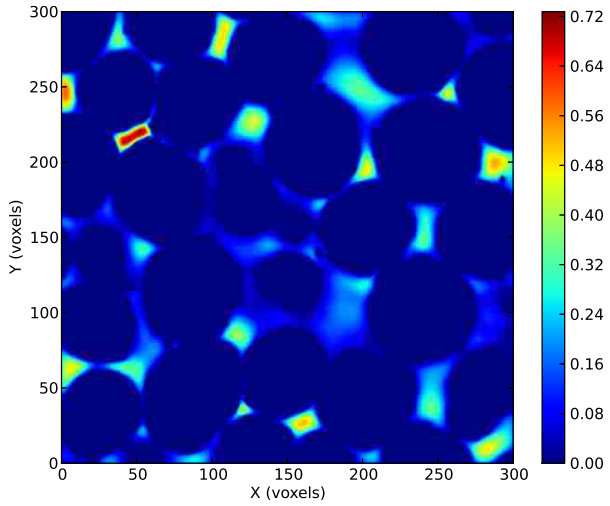


(a)

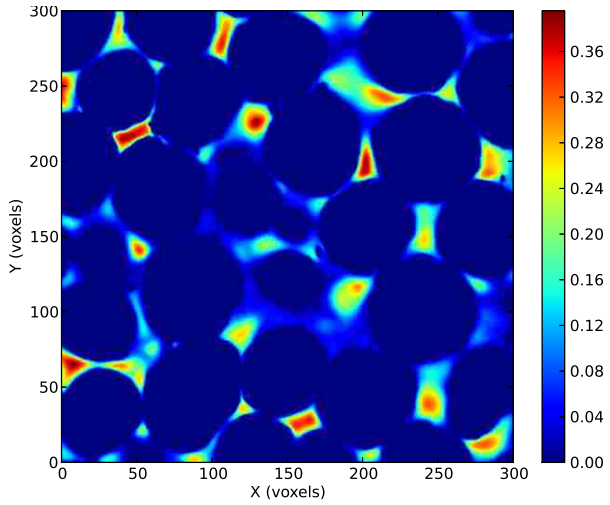


(b)

Figure 5.4: Normalized velocity-magnitude profile of a xy-cross section of the proppant pack under 12000 psi confining stress. (a) shows the velocity magnitude profile for Reynolds number of 0.024 ($F_0$ = 5.07E-04) and (b) shows the profile for Reynolds number of 18.1 ($F_0$ = 3.83E-01)

## 5.3 Discussion

Due to large pore- and grain-sizes of the proppant pack, calculation of the permeabilities for each stress conditions are done without substantial numerical errors (finite-size errors and relaxation-time dependence of the no-flow boundaries are not significant) . However, for calculating non-Darcy flow parameters, another issue comes into the picture for high pressure gradients (body-forces). This limits the highest achievable Reynolds numbers from

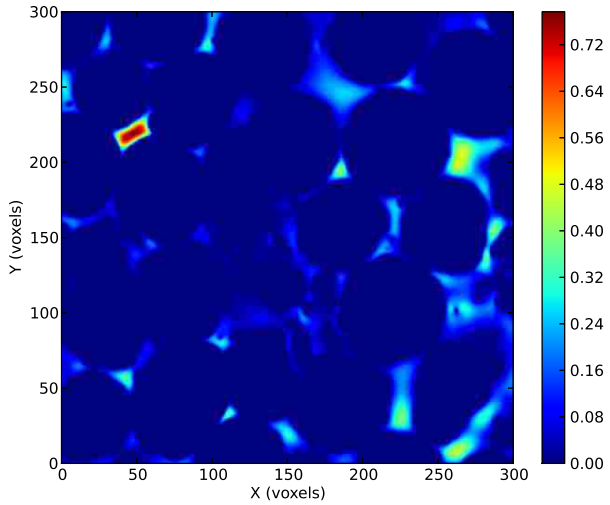


(a)

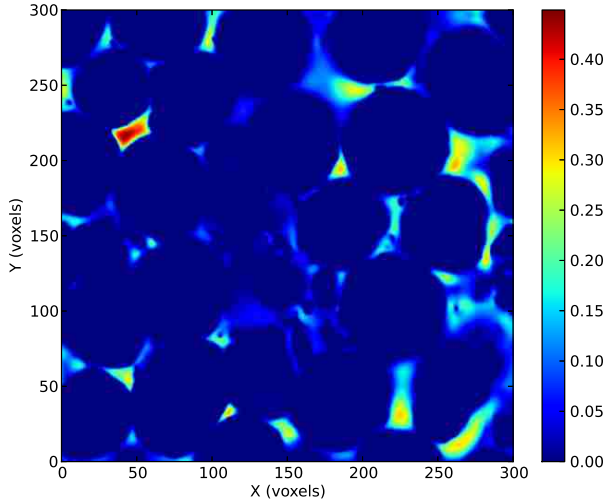


(b)

Figure 5.5: Normalized velocity-magnitude profile of a xy-cross section of the proppant pack under 20000 psi confining stress. (a) shows the velocity magnitude profile for Reynolds number of 0.010 ($F_0$ = 2.86E-04) and (b) shows the profile for Reynolds number of 8.97 ($F_0$ = 2.45E-01)

the simulations. In simulations on the original images (numerical resolution of 11.8 $\mu$m), Reynolds numbers as high as 10 are achieved. In order to reach higher ranges of Reynolds number, the numerical resolution of the images are increased by dividing each side of each voxels in the domain by two. This causes a numerical domain of 8 times as large and a numerical resolution of 6.9 $\mu$m. In this case, flow simulations result in Reynolds numbers as

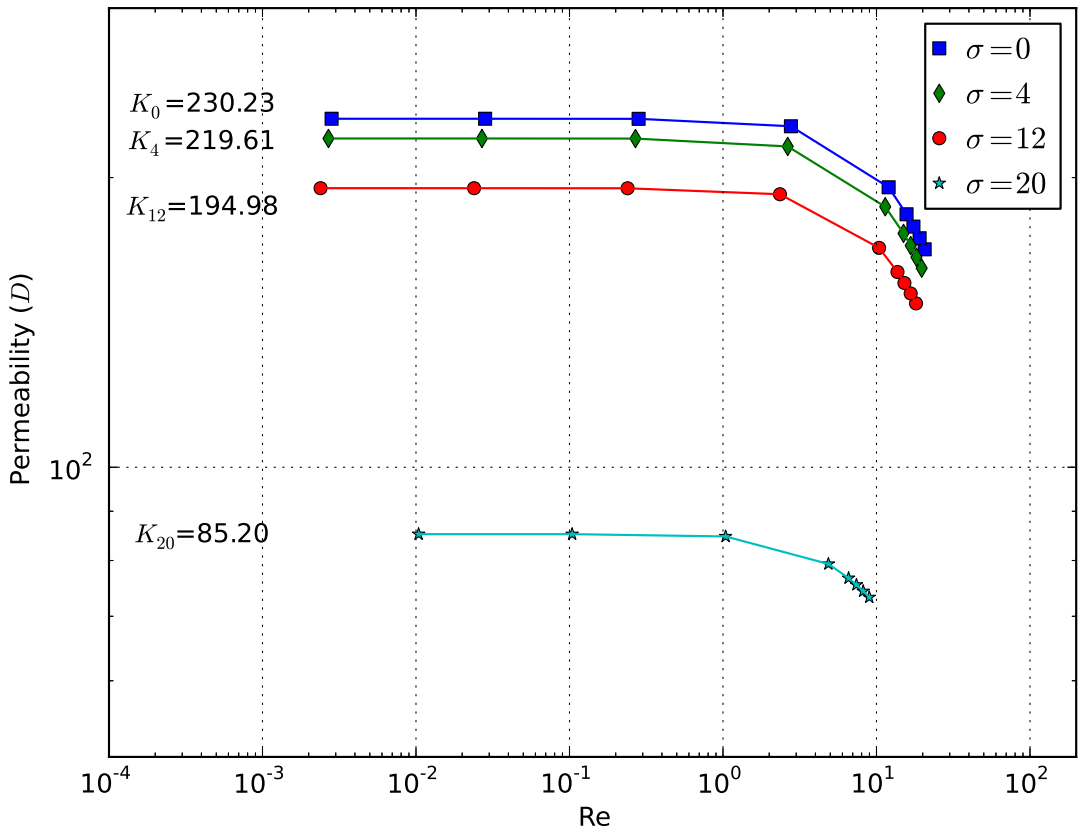


Figure 5.6: Apparent permeability of proppant packs at different confining stresses vs. Reynolds number. As confining stress on the samples increase, permeability of the samples decrease. Due to increase of flow rate (Reynolds number), inertial flow, which was once negligible in low-Reynolds number creeping flow starts to play a more significant role. Therefore, apparent permeability of the samples for elevated flow rates decrease. Subscripts show the confining stresses (Kpsi) on the packings

Table 5.1: Calculated permeabilities (in Darcy unit) for different confining stresses

| Permeability | 0 (Kpsi) | 4 (Kpsi) | 12 (Kpsi) | 20 (Kpsi) |
|---|---|---|---|---|
| $K_{xx}$ | 225.15 | 210.86 | 193.21 | 107.56 |
| $K_{xy}$ | -2.29 | 3.09 | -1.33 | 1.80 |
| $K_{xz}$ | -2.12 | -2.12 | -1.30 | -1.06 |
| $K_{yx}$ | -2.29 | 3.09 | -1.33 | 1.80 |
| $K_{yy}$ | 221.94 | 208.61 | 188.88 | 95.24 |
| $K_{yz}$ | -6.63 | 6.91 | 3.32 | 2.62 |
| $K_{zx}$ | -2.12 | -2.12 | -1.30 | -1.06 |
| $K_{zy}$ | -6.63 | 6.91 | 3.32 | 2.62 |
| $K_{zz}$ | 230.23 | 219.61 | 194.98 | 85.21 |

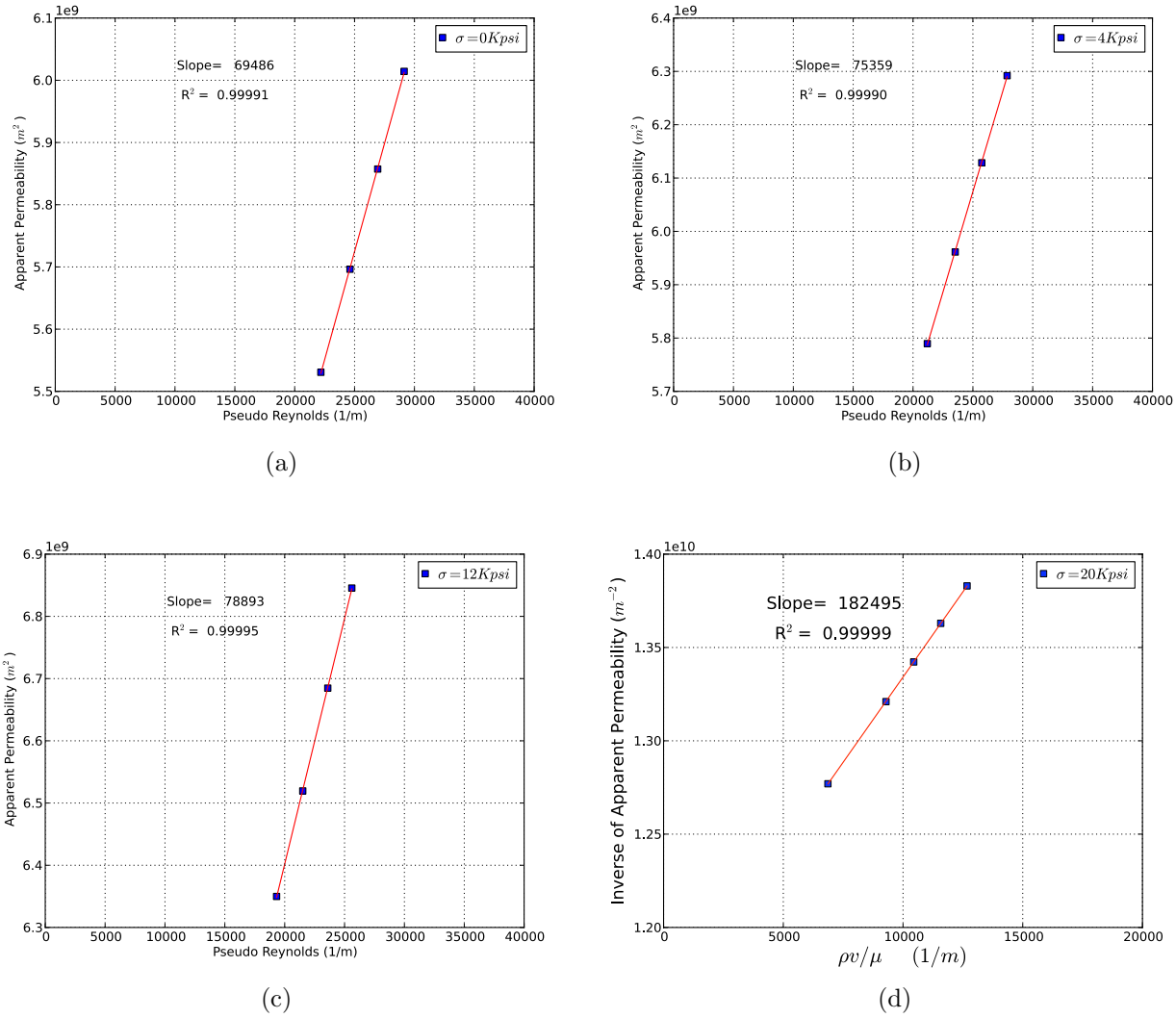


Figure 5.7: Inverse of apparent z-direction permeability vs. pseudo Reynolds number under 0 Kpsi, 4 Kpsi , 12 Kpsi, and 12 Kpsi stresses (a-d respectively). Slopes of each fitted line denote the calculated $\beta-$factor. $\beta-$factors increase as confining stress on the proppant pack increases.

Table 5.2: X-direction flow simulation results for different confining stresses

| Stress (Kpsi) | Permeability (D) | $\beta-$factor (1/m) | $R^2$ |
|---|---|---|---|
| 0 | 230.230 | 69486 | 0.9999 |
| 4 | 219.612 | 75359 | 0.9999 |
| 12 | 194.981 | 78893 | 0.9999 |
| 20 | 85.206 | 182495 | 1.0000 |

Table 5.3: Y-direction flow simulation results for different confining stresses

| Stress (Kpsi) | Permeability (D) | $\beta-$factor (1/m) | $R^2$ |
|---|---|---|---|
| 0 | 221.943 | 73034 | 0.9999 |
| 4 | 208.611 | 79184 | 0.9999 |
| 12 | 188.876 | 83076 | 0.9998 |
| 20 | 95.240 | 179555 | 0.9999 |

Table 5.4: Z-direction flow simulation results for different confining stresses

| Stress (Kpsi) | Permeability (D) | $\beta-$factor (1/m) | $R^2$ |
|---|---|---|---|
| 0 | 225.145 | 61488 | 0.9999 |
| 4 | 210.855 | 72506 | 0.9997 |
| 12 | 193.214 | 78938 | 0.9999 |
| 20 | 107.559 | 172876 | 0.9989 |

high as 20 ($F_0$ of 0.47), which are then used for determination of non-Darcy factors for each stress condition and flow directions.

Pore-scale flow simulations show that the permeability is relatively insensitive to stress prior to fracturing of proppant grains and the results differ from the results published by the proppant vendor. When grain fracturing occurs, the change of permeabilities are more substantial and there seems to be a better agreement with Vendors data. Non-Darcy flow results also show a smaller change with confining stress compared to the Vendor's data for lower stresses. Grain fracturing results in a substantial increase in the calculated non-Darcy flow parameter.

# Chapter 6
# Upscaling of pore-scale flow information into the completions scale simulation results

Hydraulic fractures are one the well-known completion methods for production from the tight gas formations. Performance of these hydraulic fractures are dependent on the non-Darcy flow. According to Vincent et al. [77], incorrect use of the published permeabilities of the proppants and neglecting the non-Darcy effect can cause an inaccurate estimations of the conductivities of the fracture, design of a sub-optimal stimulation treatment with a shorter effective producing fracture half-length, overestimation of the post-stimulation of the production, inaccurate selection of the proppant for the design of the fracture, and decrease in the productivity of the well.

## 6.1 Gas flow through porous media

The single-phase gas flow is derived using the combinations of continuity equation with Darcy's law as the momentum equation. The general form of the equation in cartesian coordinates is,

$$\frac{\partial}{\partial x}\left[\beta_c \frac{A_x k_x}{\mu_g B_g}\left(\frac{\partial p}{\partial x} - \gamma_g \frac{\partial Z}{\partial x}\right)\right]\Delta x + \frac{\partial}{\partial y}\left[\beta_c \frac{A_y k_y}{\mu_g B_g}\left(\frac{\partial p}{\partial y} - \gamma_g \frac{\partial Z}{\partial y}\right)\right]\Delta y + \frac{\partial}{\partial z}\left[\beta_c \frac{A_z k_z}{\mu_g B_g}\left(\frac{\partial p}{\partial z} - \gamma_g \frac{\partial Z}{\partial z}\right)\right]\Delta z + q_{gsc} = \frac{V_b}{\alpha_c}\frac{\partial}{\partial t}\left(\frac{\phi}{B_g}\right) \tag{6.1}$$

where $A_x$, $A_y$, and $A_z$ is the cross-sectional area perpendicular to x, y, and z directions, respectively, $B_g$ is gas formation volume factor (reservoir volume/volume at standard con-

ditions), $\gamma_g$ is gravity of gas, $\phi$ is the porosity of the rock in the grid block, $V_b$ is the volume of the grid block, $Z$ is the elevation of the center of the grid block.

As it can be seen in the equation above, the equation is non-linear since $\mu_g$ and $B_g$ are functions of the pressure. Comparing these terms with those of oil, in the gas phase, the dependence of these parameters are stronger to pressure and thus special linearization techniques should be used. Among the linearization techniques for these systems in the literature (explicit treatment of the transmissibility terms, extrapolation of the transmissibility terms, simple iteration, and fully implicit treatment of the transmissibility terms) [16], simple iteration of the transmissibility terms are used. In this method, the transmissibility terms are estimated at the one iteration prior to which pressures are evaluated. Detailed description of this method can be found in Ertekin et al. [16]. The formulation of this linearization method is described below,

$$\begin{aligned} &T^{n^\nu}_{gx_{i+1/2,j}}\left(P^{n+1^{(\nu+1)}}_{i+1/2,j} - P^{n+1^{(\nu+1)}}_{i,j}\right) - T^{n^\nu}_{gx_{i-1/2,j}}\left(P^{n+1^{(\nu+1)}}_{i,j} - P^{n+1^{(\nu+1)}}_{i-1/2,j}\right) + \\ &T^{n^\nu}_{gy_{i,j+1/2}}\left(P^{n+1^{(\nu+1)}}_{i,j+1/2} - P^{n+1^{(\nu+1)}}_{i,j}\right) - T^{n^\nu}_{gy_{i-1/2,j}}\left(P^{n+1^{(\nu+1)}}_{i,j} - P^{n+1^{(\nu+1)}}_{i,j-1/2}\right) = \\ &\qquad\qquad \frac{\Gamma^{n+1^{(\nu)}}_{g_{i,j}}}{\Delta t}\left(P^{n+1^{(\nu+1)}}_{i,j} - P^{n}_{i,j}\right) - q^{n+1}_{gsc_{i,j}} \end{aligned} \tag{6.2}$$

where $P_{i,j}$ is pressure of Gridblock (i,j), superscript $n$ and $n+1$ are the old and new timesteps, respectively. $T_{gx_{i\pm1/2,j}}$ is gas transmissibility along the x-direction between Gridblock (i,j) and Gridblock (i±1,j). Superscript $\nu$ and $\nu+1$ are old and new iterations, respectively, and

$$\Gamma^{n+1^{(\nu)}}_{g_{i,j}} = \frac{V_{b_{i,j}}}{\alpha_c}\left[\frac{\phi^o c_\phi}{B^{n+1}_g} + \frac{\phi^n}{B^n_g}\left(B^n_g/B^{n+1}_g - 1\right)/\left(P^{n+1} - P^n\right)\right]_{i,j} \tag{6.3}$$

$\left(B^n_g/B^{n+1}_g - 1\right)/\left(P^{n+1} - P^n\right)$ is the average compressibility between $P^n$ and $P^{n+1}$. where $c_\phi$ is the rock compressibility.

## 6.2 Verification

The code describing the gas flow through the reservoir is verified against the analytical solutions describing the volumetric gas reservoir material balance [13] and pressure evolution equation for an infinite-acting reservoir [1].

### 6.2.1 Volumetric Gas Reservoir Material Balance

The general material balance equation for a gas reservoir with water production $W_p$ is,

$$G(B_g - B_{gi}) + GB_{gi}\frac{(c_w S_{wi} + c_f)}{1 - S_{wi}}\Delta\bar{p} + W_e = G_p B_g + B_w W_p \tag{6.4}$$

where $G$ is Original gas in place (OGIP), $G_p$ is cumulative gas production, $B_{gi}$ is initial gas formation factor, $B_w$ is water formation factor, $W_p$ is cumulative water production, $W_e$ is the water influx, and $c_f$ and $c_w$ are rock and water compressibilities. Since the water and rock compressibilities are smaller compared to gas compressibilities, they can be neglected in the equation above. For a case of a volumetric reservoir with assuming there is no water productions and encroachments, the material balance equation simplifies to [13],

$$G(B_g - B_{gi}) = G_p B_g \tag{6.5}$$

or, by putting the $B_g$ terms in the eqaution, one can get,

$$G\frac{p_{sc} z T}{T_{sc} p} - G\frac{p_{sc} z_i T_i}{T_{sc} p_i} = G_p \frac{p_{sc} z T}{T_{sc} p} \tag{6.6}$$

Assuming isothermal conditions, then

$$G\frac{z}{p} - G\frac{z_i}{p_i} = G_p \frac{z}{p} \tag{6.7}$$

Table 6.1: Tabulated model parameters used for model verifications.

| Simulation Input | |
|---|---|
| Initial reservoir Pressure (psi) | 1614.7 |
| Reservoir Size ($ft^3$) | 100×100 ×10 |
| Gas Flow rate (MMscf/D) | 2 |
| Porosity (%) | 10 |
| Formation Permeability (mD) | 1 |

Table 6.2: Tabulated gas properties used for the gas flow simulations.

| P (psia) | Z | $\mu_g$ (cp) |
|---|---|---|
| 0.0 | 1.000 | 0.014001 |
| 400.0 | 0.9733 | 0.014337 |
| 800.0 | 0.9503 | 0.014932 |
| 1200.0 | 0.9319 | 0.015723 |
| 1600.0 | 0.9189 | 0.016681 |
| 2000.0 | 0.9120 | 0.017784 |
| 2400.0 | 0.9113 | 0.019008 |
| 2800.0 | 0.9169 | 0.020329 |
| 3200.0 | 0.9282 | 0.021721 |
| 3600.0 | 0.9445 | 0.023151 |
| 4014.7 | 0.9647 | 0.024580 |

where $p_i$ is initial pressure and $z_i$ is Initial gas compressibility factor. By rearranging, one can get,

$$\frac{p}{z} = -\frac{p_i}{z_i G} G_p + \frac{p_i}{z_i} \tag{6.8}$$

where $p_i$ , $z_i$, and $G$ are constants. Therefore, plotting $p/z$ vs. $G_p$ would yield a straight line with slope of $-\frac{p_i}{z_i G}$ and y-intercept of $\frac{p_i}{z_i}$ [13].

### 6.2.2 Model Validation

Validation of the numerical model is performed against the material balance ($p/z$ vs. $G_p/G$) of well C in Kabir et al. [35]. Figure 6.2 shows the plot of simulation results along with the material balance data. The results of reservoir simulation data matches well with the published data. Table 6.3 lists the well and reservoir data used for numerical simulation validation.

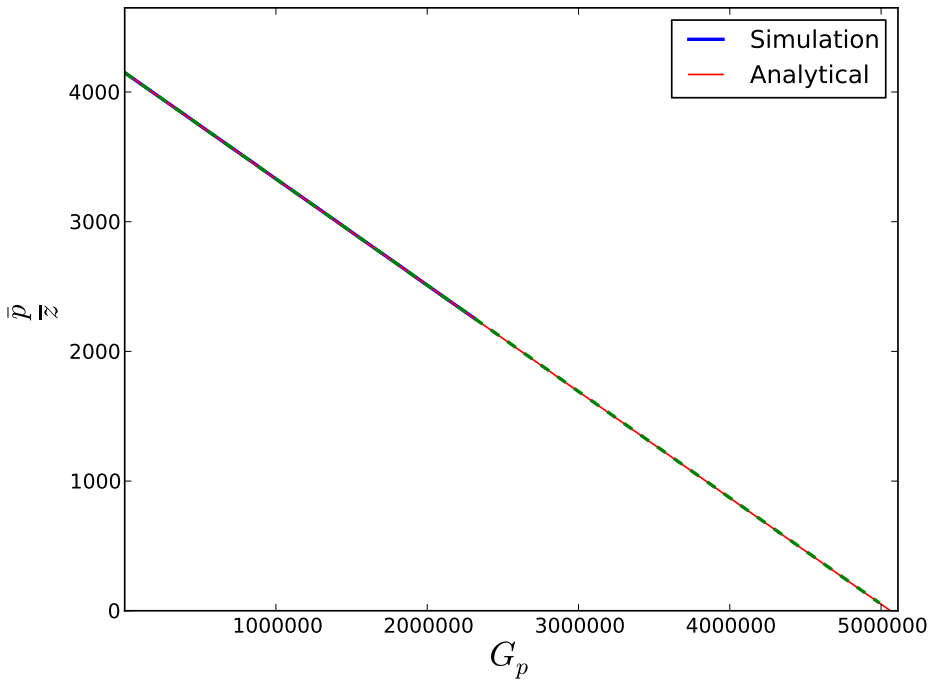


Figure 6.1: Material balance of a reservoir with properties listed in Table 6.1. Plotting $p/z$ yields a straight line with a slope of $-\frac{p_i}{z_i G}$. Blue curve shows the simulated results, the dashed line shows the fitted line to the results, and the red line shows the analytical results. The results show an agreement with the analytical solutions.

Table 6.3: Well and reservoir data used for numerical simulation validation

| Simulation Input | |
|---|---|
| Porosity (%) | 10 |
| Formation Permeability (mD) | 20 |
| Formation thickness (ft) | 100 |
| Original Gas in Place (OGIP) (Bcf) | 60 |
| Initial reservoir Pressure (psi) | 3741 |
| Gas specific gravity | 0.57 |
| Well radius (ft ) | 0.25 |

### 6.2.3 Constant production rate, radial cylindrical flow, infinite-acting reservoir (Transient)

The cartesian and radial diffusivity equations for a gas reservoir [16] can be written as

$$\frac{\partial}{\partial x}\left(\frac{\partial \psi}{\partial x}\right) + \frac{\partial}{\partial y}\left(\frac{\partial \psi}{\partial y}\right) + \frac{\partial}{\partial z}\left(\frac{\partial \psi}{\partial z}\right) = \frac{\phi \mu c_g}{0.000264k}\frac{\partial \psi}{\partial t} \tag{6.9}$$

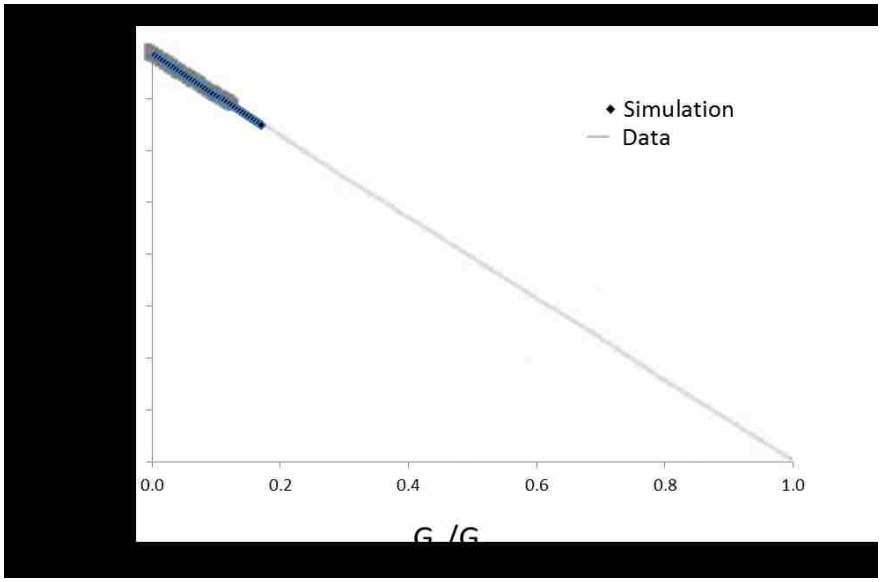


Figure 6.2: Validation of the numerical reservoir model against the material balance ($p/z$ vs. $G_p/G$) of well C in Kabir et al. [35]. In this figure, both $p/z$ values and the trend line match for the data and the reservoir simulation results.

and

$$\frac{1}{r}\frac{\partial}{\partial r}\left(r\frac{\partial \psi}{\partial r}\right) = \frac{\phi \mu c_g}{0.000264k}\frac{\partial \psi}{\partial t} \tag{6.10}$$

or in dimensionless terms,

$$\frac{1}{r_D}\frac{\partial}{\partial r_D}\left(r_D\frac{\partial p_D}{\partial r_D}\right) = \frac{\partial p_D}{\partial t_D} \tag{6.11}$$

where

$$t_D = \frac{0.0002637kt}{\phi \mu_g c_g {r_w}^2} \tag{6.12}$$

$$q_D = \frac{1.417Tq}{kh\psi_i} \tag{6.13}$$

$$\Delta p_D = \frac{\psi_i - \psi_{wf}}{\psi_i q_D} \tag{6.14}$$

where $\psi(p)$ at each pressure is defined as,

$$\psi(p) = 2\int_{p_0}^{p} \frac{p}{\mu_g z} dp \tag{6.15}$$

Following Al-Hussainy and Ramey [1], wellbore flowing pressure can be calculated using,

$$\psi(p_{wf}) = \psi(p_i) - \frac{1637(10)^3 qT}{kh}\left[log\left(\frac{kt}{\phi\mu_i c_{ti} r_w^2}\right) - 3.23\right] \tag{6.16}$$

Radial flow described in the equation above has a solution of the form

$$\Delta p_D = -0.5E_i\left(-\frac{r_D^2}{4t_D}\right) \tag{6.17}$$

where $E_i$ is the exponential integral and is defined by:

$$E_i(-x) = -\int_x^\infty \frac{e^{-u}du}{u} = [lnx - \frac{x}{1!} + \frac{x^2}{2(2!)} - \frac{x^3}{3(3!)} + ...] \tag{6.18}$$

For a case of constant production rate from an infinite-acting reservoir, $\Delta p_D$ for $r_D = 1$ $(r = r_w)$can be written as,

$$\Delta p_D = 0.5ln(t_D) + 0.809 \tag{6.19}$$

A semi-log plot between non-dimensional pressure drawdown and time would result in the slope of 0.5 and presented in Figure 6.3.

### 6.3 Numerical Model

In this study a single-phase gas, 2D, finite difference reservoir simulator is built. The reservoir assumed to be horizontal, homogeneous, isotropic, and initially filled with constant pressure gas. All the exterior boundaries are considered to be no-flow boundaries.

A hydraulic fracture is placed at the center of the reservoir. The hydraulic fracture extends on both sides of the wellbore and entire vertical extent of the fracture opening is assumed to be fully propped. Due to the symmetry in the model, flow simulations on merely one quadrant of the model are run. Since the width of the fractures are usually orders of magnitudes smaller than the sizes of grids usually used in the reservoir simulators (sizes of fracture openings are fractions of inches while grid sizes can be hundreds of feet), gradual mesh refinement

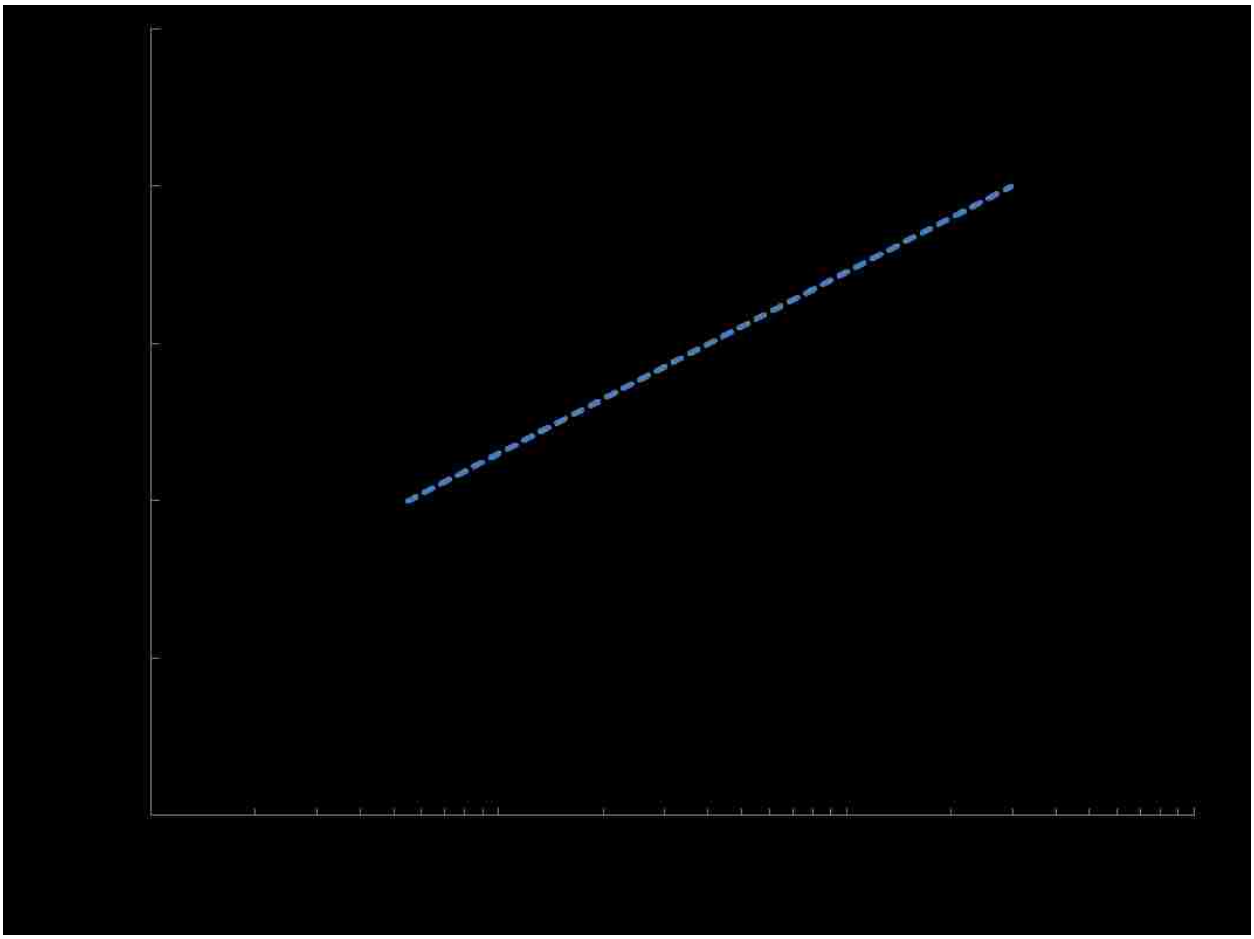

Figure 6.3: Transient gas well test analysis of the reservoir model described in Table 6.1. Plot of $\Delta p_D$ vs. $t_D$ results in a straight line with a slope of 0.5.

is implemented around the fracture. Time steps are chosen is a manner that stability of the model is maintained.

Different sets of reservoir simulations are run. Different parameters of the reservoir and fracture are altered and their impact on the profile of the fracture permeability, fracture apparent permeability, and fluid pressures are investigated. Among the model parameters, reservoir permeability, fracture length, and fracture width are altered.

A model with the parameters listed in the Table 6.4 is considered as a base-case and all the changes of the model parameters are made based on it. For all the cases, two flow simulations, one with considering non-Darcy flows and one without it are run. The fluid properties as a function of gas pressure are tabulated in the Table 6.2.

Table 6.4: Tabulated reservoir used for the base-case model.

| Simulation Input | |
|---|---|
| Initial reservoir Pressure (psia) | 4000.0 |
| Reservoir Size ($ft^3$) | 1000×1000×100 |
| Fracture Length (ft) | 500 |
| Fracture Width (ft) | 0.049 |
| Porosity (%) | 8 |
| Overburden Stress (psi) | 10000 |
| Formation Permeability (md) | 1 |

Gas flow simulation results of the base-case are shown in Figures 6.4, 6.5, 6.6, and 6.7. All the simulations with different gas flow rates, have the same cumulative gas production (2.37% of OGIP). (Apparent) permeability profile of the fracture for three different gas flow rates are shown in the Figures 6.4. As flow rates grow larger, fraction of the fracture x-direction permeability respect to the initial x-direction permeability (205.702 D) decreases. This is due to the increased pressure drop in the fracture and therefore, increase in the effective stress on the fracture cells. For higher gas flow rates, apparent permeabilities (which are inversely proportional to the flow velocities) decrease. The higher flow velocities in the cells, the higher non-Darcy flows would be and therefore, the lower apparent permeabilities are resulted. As fluid approaches the wellbore, the flow velocities become larger and they result in the lowest apparent permeabilities in the closest cell to the wellbore. For a flow rate of $q = 10MMscf/d$, apparent x-direction permeability decreases from 58% of the initial permeability to 27% of it for $q = 30MMscf/d$

Pressure distributions in the reservoir are plotted in the Figure 6.6. As the gas flow rates grow larger, lower bottom hole pressure are achieved due to inability of the reservoir matrix to feed the fracture,. As can be seen in the results of the next subsection, when the permeability of the matrix is larger (10md), we see a more distributed pressure contours in the reservoir compared to the base case.

Productivity indices of the base-case flow simulations are plotted in the Figures 6.7. Pro-

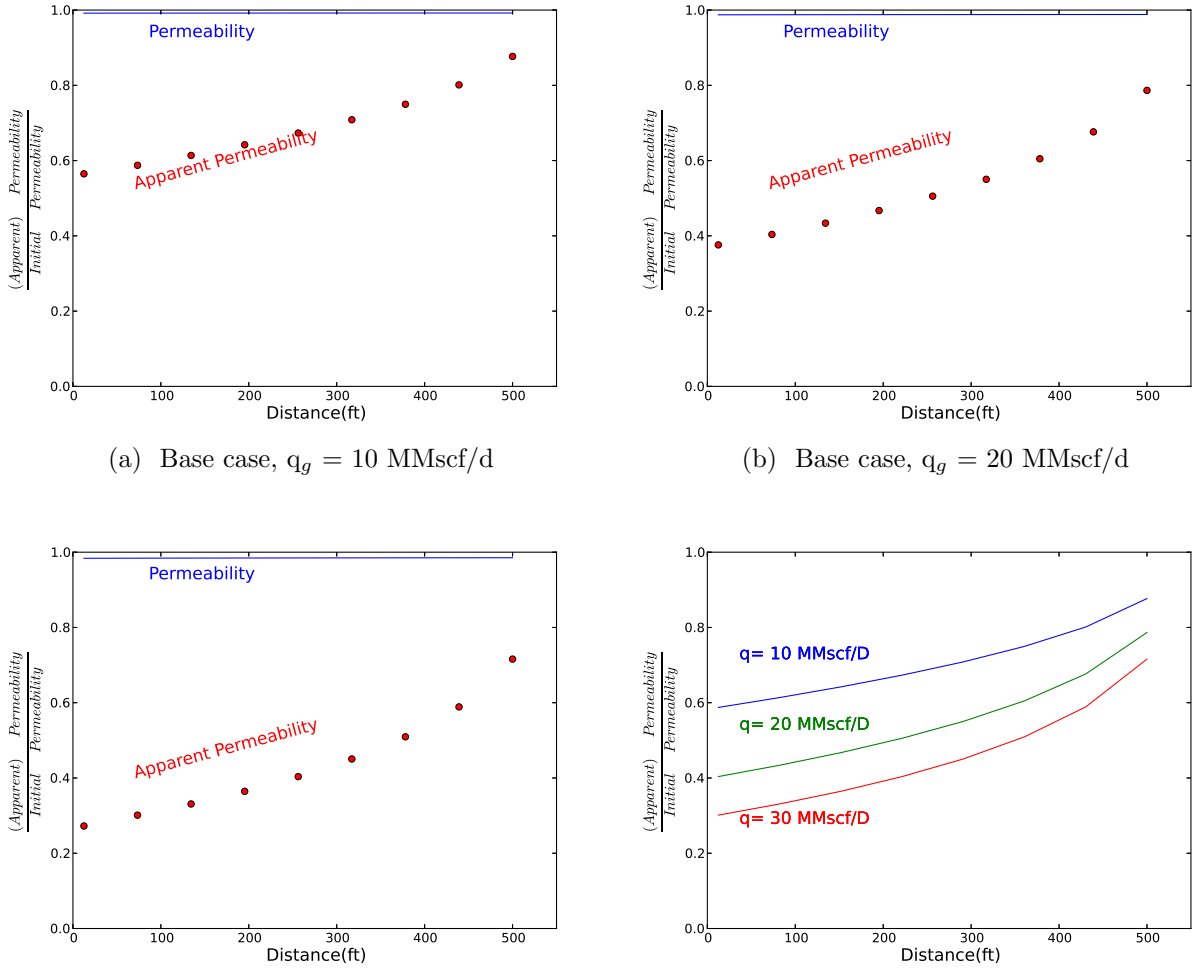


(a) Base case, $q_g$ = 10 MMscf/d

(b) Base case, $q_g$ = 20 MMscf/d

(c) Base case, $q_g$ = 30 MMscf/d

(d) Base case, $q_g$ = 10 MMscf/d

Figure 6.4: Normalized fracture (apparent) permeability profile for the base case for three different flow rates of of 10 MMscf/D in (a), 20 MMscf/D in (b), 30 MMscf/D in (c), and a comparison of the profiles for these flow rates in (d). For a case of ignoring non-Darcy flows, the blue curves show the change of the permeability of the fracture due to change of the effective stress in the fracture. Red bullets show the apparent permeability profile in the fracture when non-Darcy parameter in considered in the simulations. As can be seen, there is a substantial apparent permeability drop in the fracture due to the non-Darcy flows.

ductivity index of a gas reservoir is,

$$J_g = \frac{q\mu z}{\bar{p}_r^2 - p_{wf}^2} \tag{6.20}$$

where $J_g$ is the productivity index of gas reservoir, $z$ is the gas compressibility factor, $\mu$ is the gas viscosity, $q$ is the gas flow rate in standard conditions, $\bar{p}_r$ is the reservoir average

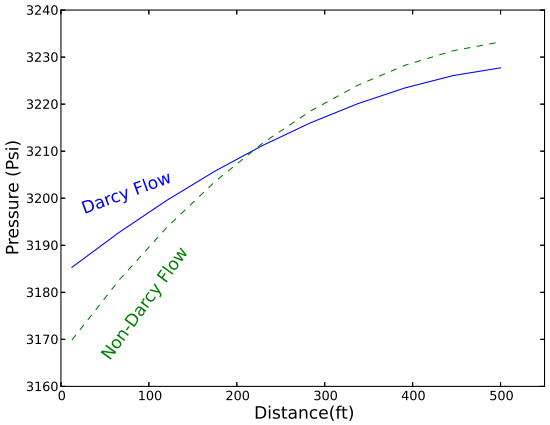


(a) Base case, $q_g$ = 10 MMscf/d

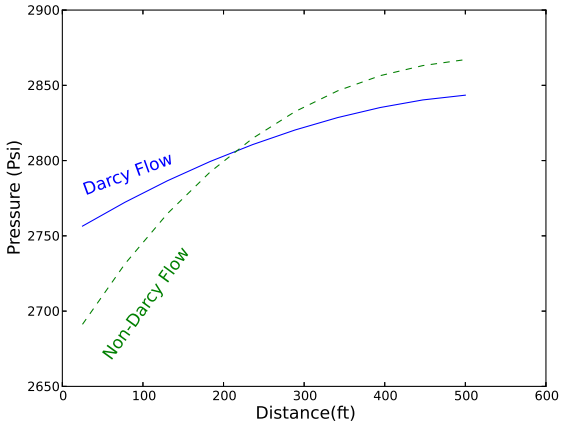


(b) Base case, $q_g$ = 20 MMscf/d

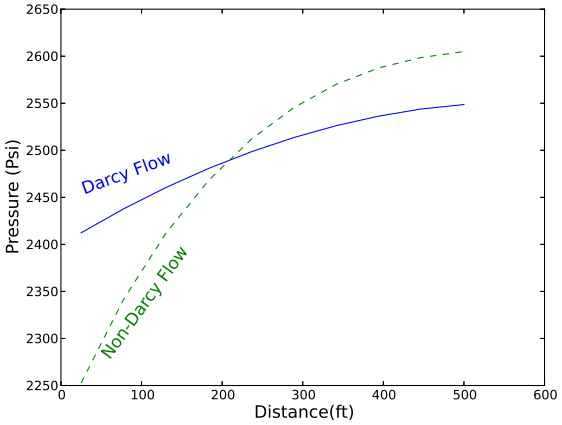


(c) Base case, $q_g$ = 30 MMscf/d

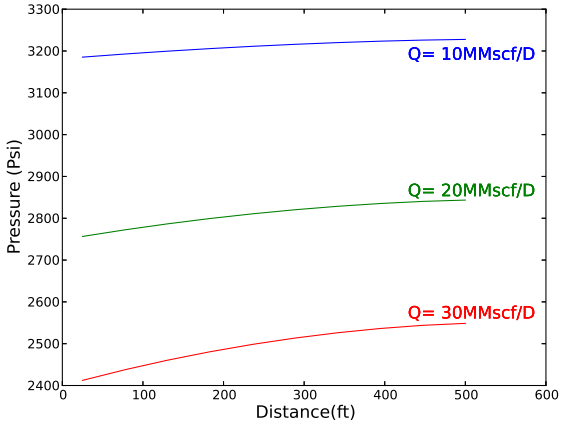


(d) Base case, $q_g$ = 30 MMscf/d

Figure 6.5: Fracture pressure profiles for the base case for three different flow rates of of 10 MMscf/D in (a), 20 MMscf/D in (b), 30 MMscf/D in (c), and a comparison of the profiles for the cases in which non-Darcy flows are considered in the flow simulations in (d). For all the flow rates, gradients of the pressure drop are higher for the case considering non-Darcy flow parameters in the simulation than those without considering non-Darcy flow parameters. Pressures in the fracture has thier lower values in the cells closest to the wellbore.

pressure, and $p_{wf}$ is the flowing bottom hole pressure.

All the figures show the same pattern of a sharp reduction at the early stages of the gas production followed by a slight reduction of productivity index by further gas productions. The early-time reductions of productivity indices are due to the transient behavior of the reservoir (infinite acting behavior). When the semi-steady-state regime is reached (pressure changes are felt by the all the boundaries of the reservoir), rate of change of the productivity

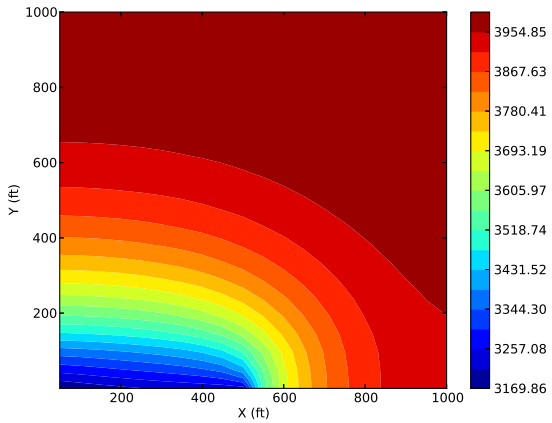


(a) Base case, $q_g = 10$ MMscf/d

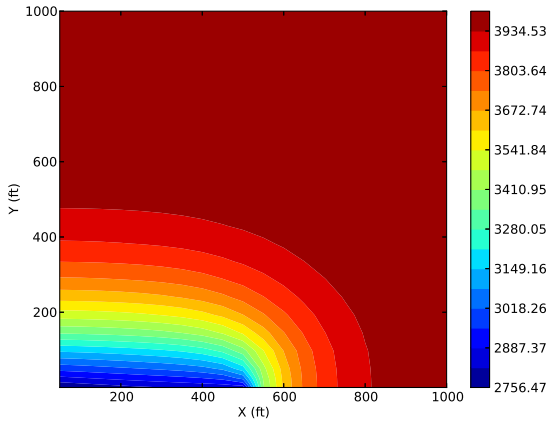


(b) Base case, $q_g = 20$ MMscf/d

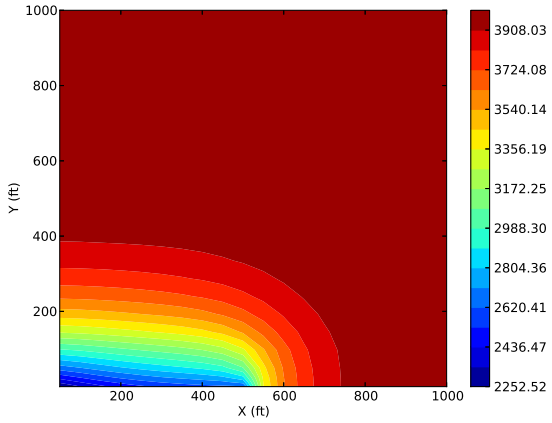


(c) Base case, $q_g = 30$ MMscf/d

Figure 6.6: Pressure distributions of the base-case for three different flow rates of 10 MMscf/D in (a) , 20 MMscf/D in (b), and 30 MMscf/D in (c). As the gas flow rate increases, lower flowing bottom hole pressures are required to maintain the flow rate.

indices with time (or cumulative gas production) becomes subtle. This reduction is due to the fact that the rate of change of the flowing bottom hole pressure is more significant compared to the rate of change of the reservoir pressure due to low permeability of the reservoir matrix surrounding the fracture, and a lower hydraulic connection between the fracture and the matrix exist. Therefore, according to the Equation 6.20, productivity index decreases with time. Moreover, for all the gas flow rates considered, including non-Darcy flows in the simulations cause reductions in the flowing bottom hole pressure (it is also seen in the Figures 6.5), and therefore, lower productivity indices are achieved compared to the cases where non-Darcy flows are not considered. As the gas flow rate increases, differences between the two curves increase.

In summary, as gas flow rates increase, non-Darcy factor increases and therefore, reductions in the apparent permeability occur. Reductions in the flowing bottom hole pressure shown in Figure 6.5d and reductions in the productivity-index ratio, which is defined by $J_{non-D}/J_D$ and it is shown in Figure 6.7d. For gas flow rate of 30 MMscf/D, the productivity-index ratio reaches almost 91%.

### 6.3.1 Effect of the reservoir permeability

In order to investigate impact of the reservoir permeability on the simulation results, permeability of the reservoir increased from the base-case's permeability (1 md) to 10 md and all the other fluid and reservoir properties are maintained the same as in the base case. Figures 6.8 show the (apparent) permeability profiles of the fracture for different flow rates. In this case, due to a better hydraulic connectivity between the fracture and the reservoir matrix, the fracture pressure drops are less than those of the base case. Pressure profiles in the fracture for different flow rates are plotted in the Figures 6.9. In this case, for all the flow rates, the pressure values in the fracture for all the corresponding flow rates are higher in the case of the $K_{res} = 10$ md for the same gas flow rates. This is due to a better hydraulic connectivity between the reservoir and the fracture. Like the apparent permeability profiles of the base case, there are substantial apparent permeability drops in the fracture due to

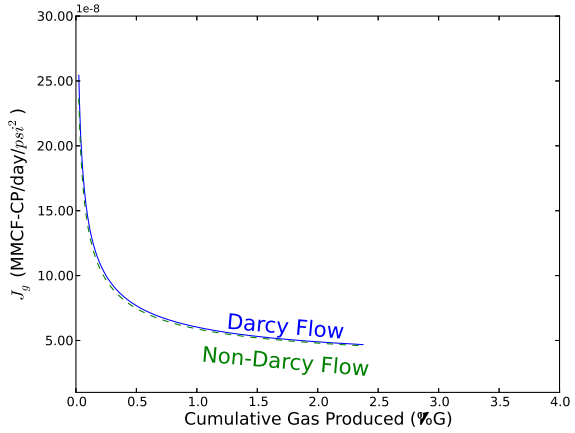


(a) Base case, $q_g$ = 10 MMscf/d

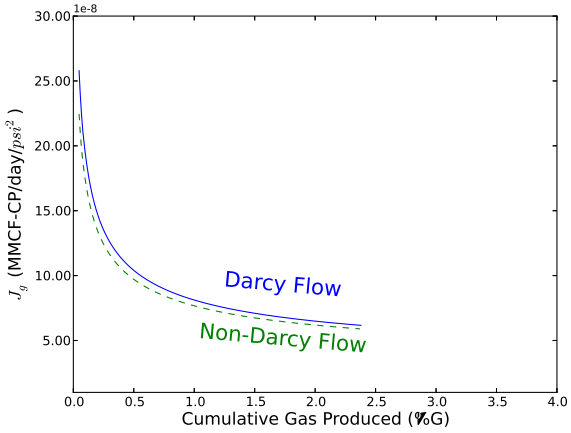


(b) Base case, $q_g$ = 20 MMscf/d

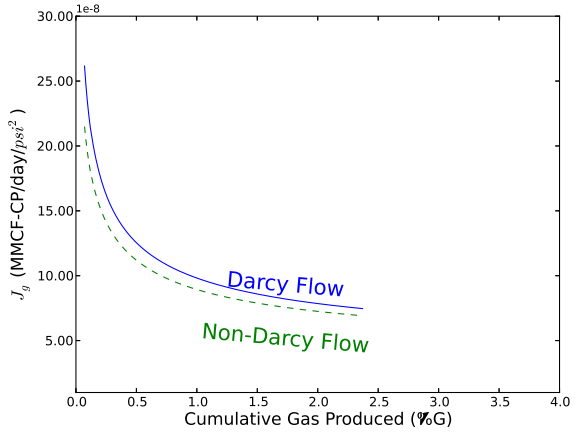


(c) Base case, $q_g$ = 30 MMscf/d

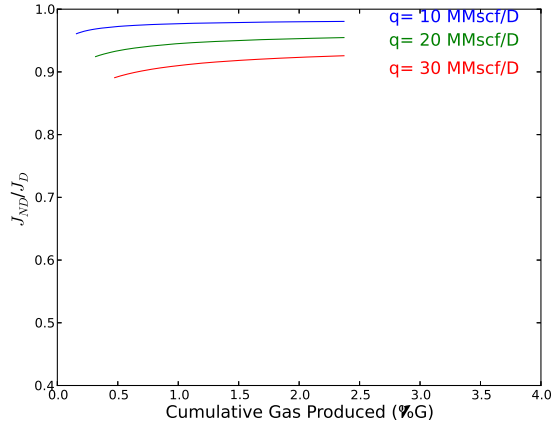


(d) Base case, $q_g$ = 20 MMscf/d

Figure 6.7: Productivity indices of the base-case for three different flow rates of 10 MMscf/D in (a), 20 MMscf/D in (b), and 30 MMscf/D in (c), and comparison of the productivity-index ratios for these flow rates in (d). For all the gas flow rates considered, including non-Darcy flows in the simulations, causes reductions in the flowing bottom hole pressure (it is also seen in the Figures 6.5), and therefore, lower productivity indices are achieved compared to the cases where they are not considered. As the gas flow rate increases, differences between the two curves increase. (d) shows the reduction in the productivity-index ratios as gas flow rates increase.

the non-Darcy considerations. However, compared to the base case, apparent permeability reductions are not as high. Pressure distributions (shown in Figures 6.10) are more propagated in the reservoir for this case compared to the base case for the same gas flow rates. Productivity indices of the simulation results for different gas flow rates are shown in Figures 6.11. In this case, productivity-index ratio reach to almost 80% when non-Darcy flows

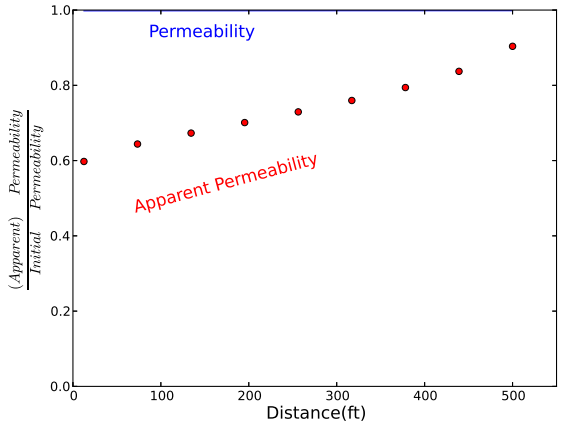


(a) $K_{res}$ = 10 md, $q_g$ = 10 MMscf/D

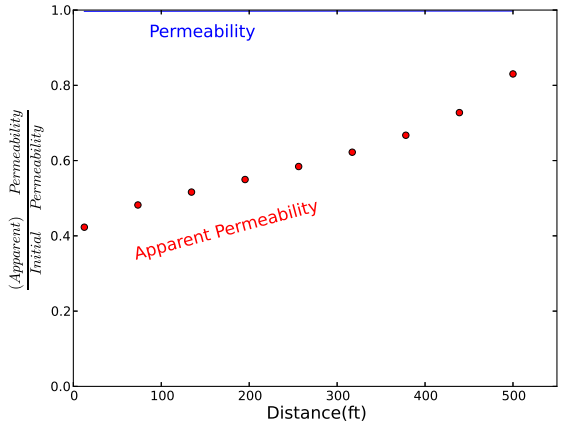


(b) $K_{res}$ = 10 md, $q_g$ = 20 MMscf/D

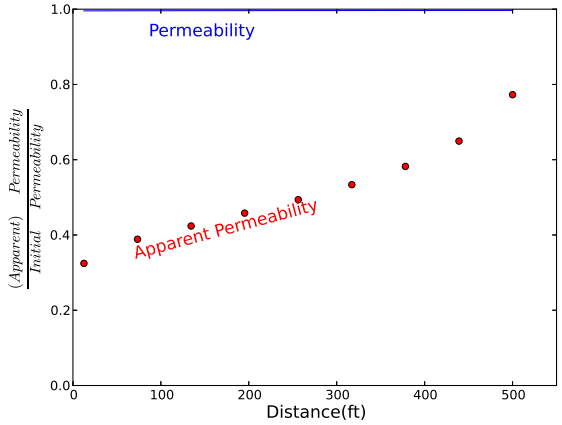


(c) $K_{res}$ = 10 md, $q_g$ = 30 MMscf/D

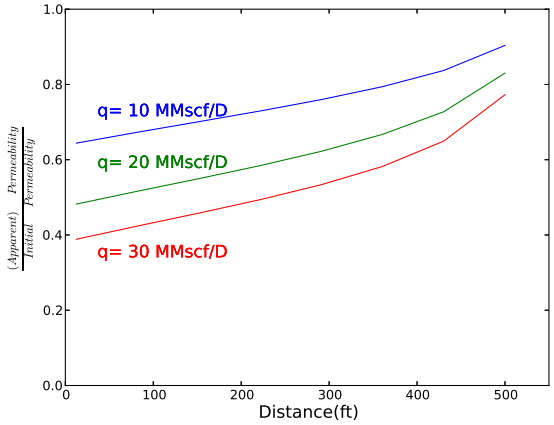


(d) $K_{res}$ = 10 md, $q_g$ = 10 MMscf/D

Figure 6.8: Normalized fracture (apparent) permeability profiles for the case with reservoir permeability of 10 md for three different flow rates of 10 MMscf/D in (a), 20 MMscf/D in (b), 30 MMscf/D in (c), and a comparison of the profiles for these flow rates in (d). Permeability reductions are less compared to the base case due to the fact that pressures in the fractures do not drop as high as the base case's. Like the base case apparent permeability profiles, there are substantial apparent permeability drops in the fracture due to the non-Darcy considerations. However, compared to the base case, apparent permeability reductions are not as high.

are considered in the simulations for gas flow rate of 30 MMscf/D.

### 6.3.2 Effect of the fracture width

Impact of the fracture width on the gas flow simulations is considered by increasing the fracture width from 0.049 ft in the base case to 0.098 ft. Figures 6.12 show the impact of

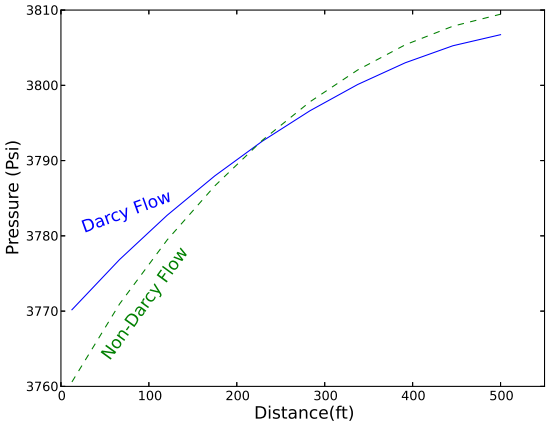


(a) $K_{res}$ = 10 md, $q_g$ = 10 MMscf/D

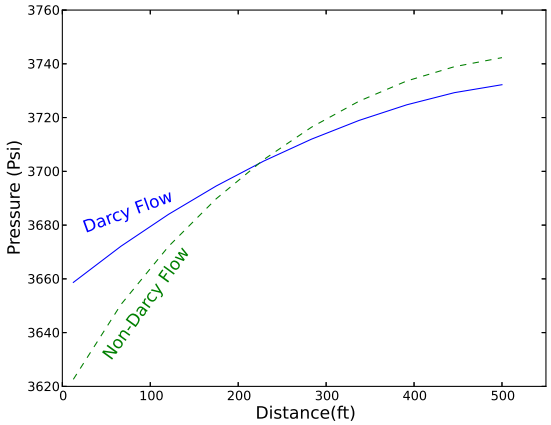


(b) $K_{res}$ = 10 md, $q_g$ = 20 MMscf/D

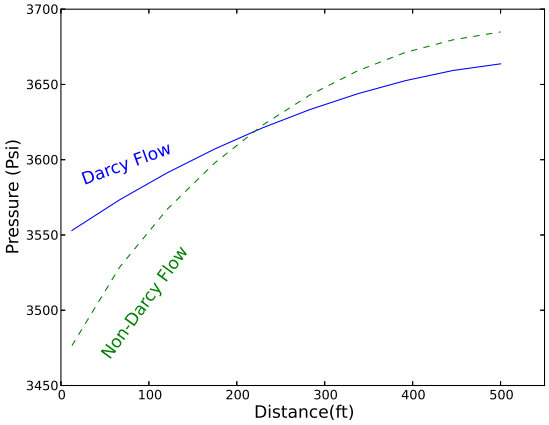


(c) $K_{res}$ = 10 md, $q_g$ = 30 MMscf/D

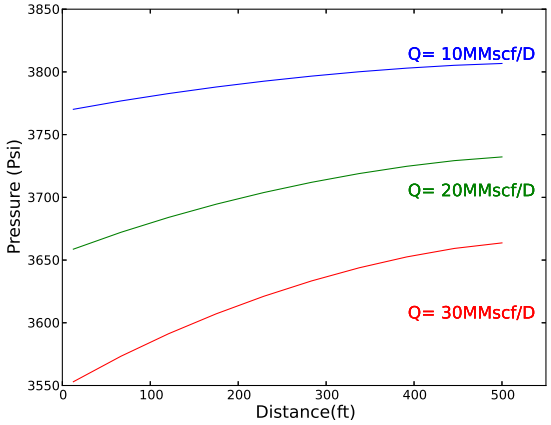


(d) $K_{res}$ = 10 md, $q_g$ = 30 MMscf/D

Figure 6.9: Fracture pressure profile for the case with the reservoir permeability of 10 md for three different flow rates of 10 in (a), 20 in (b), and 30 MMscf/D in (c), and a comparison of the profiles for these flow rates in (d). The rates of change of pressure with distance are slightly lower for this case compared to the base case for both Darcy flow and non-Darcy flow. The pressure in the fracture closest to the wellbore is also higher for this case compared to the base case for both Darcy and non-Darcy flow for corresponding flow rates.

non-Darcy flows on the calculated normalized (apparent) permeability profile of the fracture. The calculated apparent permeabilities in this case is higher than those in the base case. For instance, for a flow rate of $30 MMscf/D$, the calculated apparent permeability of the closest cell to the wellbore shows a reduction of almost 30% compared to an almost 45% decrease in the base case. The rate of reductions of apparent permeability with distance is also less significance in this case compared to the base case for the same gas flow rates. Gas velocities

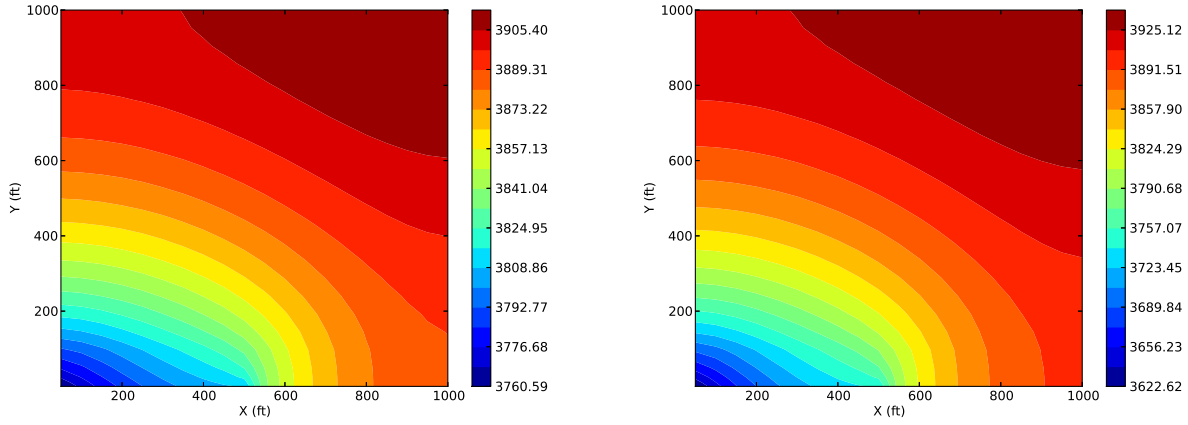


(a) $K_{res}$ = 10 md, $q_g$ = 10 MMscf/D

(b) $K_{res}$ = 10 md, $q_g$ = 30 MMscf/D

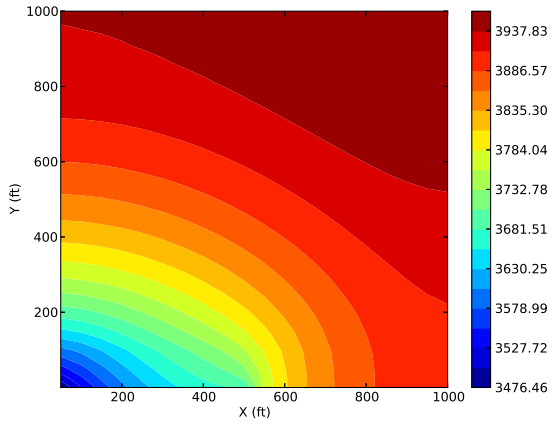


(c) $K_{res}$ = 10 md, $q_g$ = 20 MMscf/D

Figure 6.10: Pressure distributions of the case with the reservoir permeability of 10 md for three different gas flow rates of 10 in (a), 20 in (b), and 30 MMscf/D. Due to higher permeability of the reservoir and therefore, a better hydraulic communications between the reservoir and the fracture, the pressure contour lines are more distributed compared to the base case for the same gas flow rates.

in the fracture are lower when the fracture width (and therefore, cross-sectional area to flow) is larger. This causes less significant non-Darcy flows. Pressures at the fracture (shown in Figures 6.13) are higher in this case compared to the base case for the same flow rates. This also can be seen in that Pressure distributions in the reservoir are shown in Figures 6.14. Figure 6.15 show the calculated productivity indices of this case for different flow rates. For these flow rates, the effect of the non-Darcy flows on the productivity indices are less

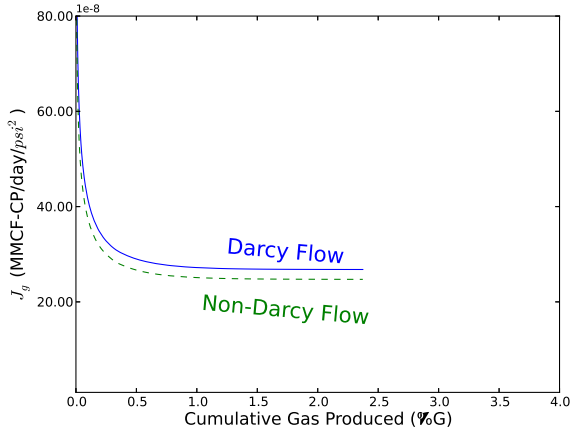


(a) $K_{res}$ = 10 md, $q_g$= 10 MMscf/D

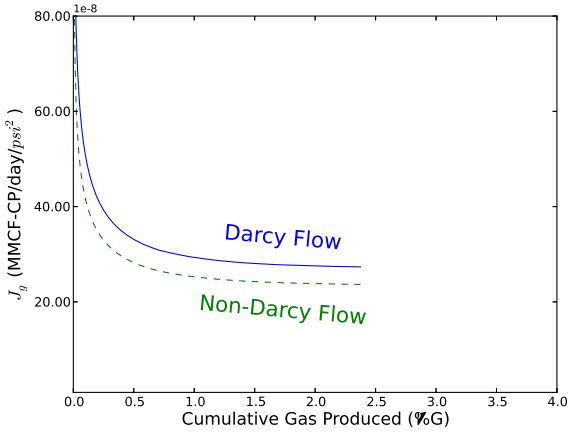


(b) $K_{res}$ = 10 md, $q_g$ = 20 MMscf/D

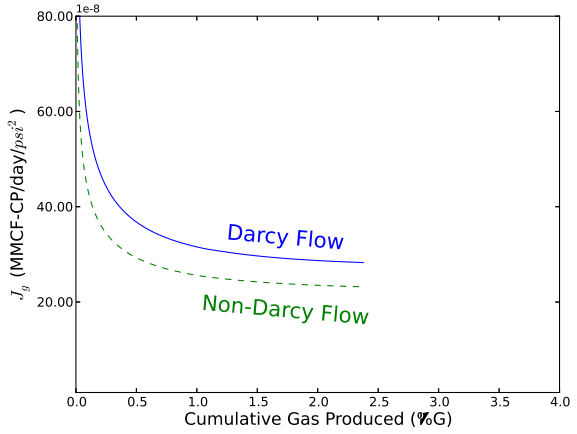


(c) $K_{res}$ = 10 md, $q_g$ = 30 MMscf/D

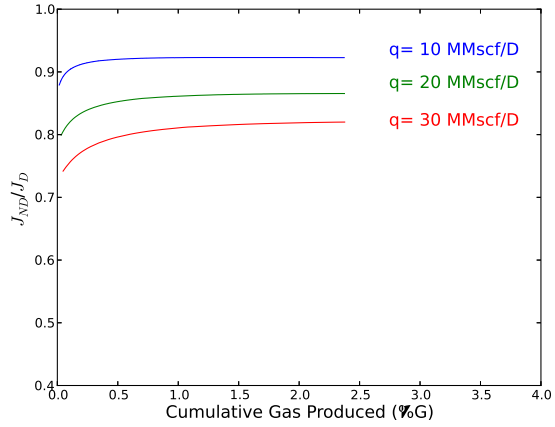


(d) $K_{res}$ = 10 md, $q_g$ = 20 MMscf/D

Figure 6.11: Productivity indices of the case with the reservoir permeability of 10 md for three different gas flow rates of 10 in (a), 20 in (b), and 30 MMscf/D in (c), and comparison of productivity-index ratios for these gas flow rates. As in the base case, productivity indices of the Darcy flows are higher than non-Darcy flows for each flow rate. Changes of the productivity indices at the semi-steasy-state regimes are less compared to the base case. This is due to the better hydraulic connectivity between the reservoir and the fracture, which results in higher flowing well pressures for the same flow rates compared to the base case. Effects of the non-Darcy flows on the productivity indices are more significant compared to the base case. Productivity-index ration can reach to almost 80% for q= 30 MMscf/D.

significant and as can be seen in Figure 6.15d, for a flow rate of 30 MMscf/D, non-Darcy flows reduce the productivity index to almost 95% compared to almost 90% in the base case.

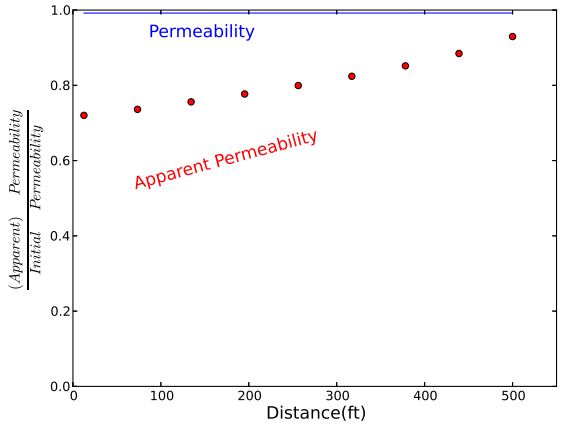


(a) Fracture width = 0.098 ft, $q_g$ = 10 MMscf/d

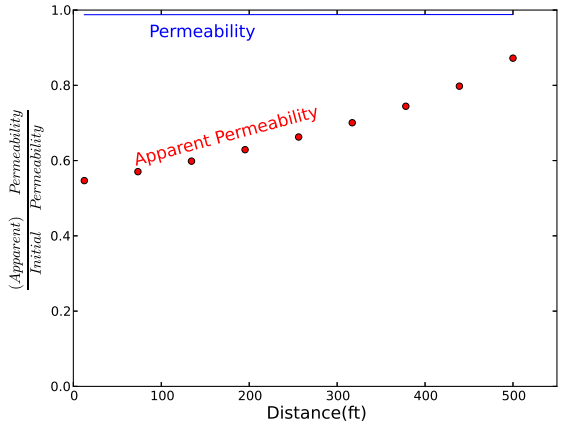


(b) Fracture width = 0.098 ft, $q_g$ = 20 MMscf/d

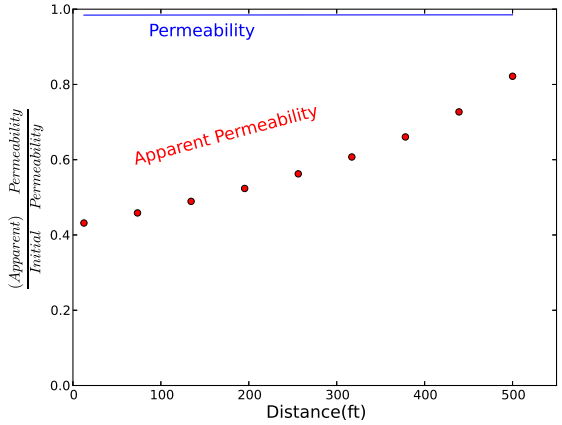


(c) Fracture width = 0.098 ft, $q_g$ = 30 MMscf/d

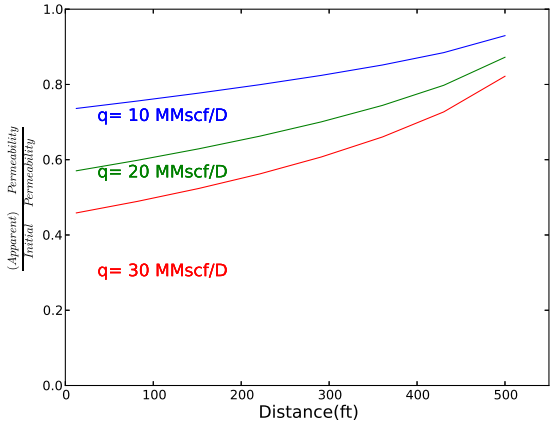


(d) Fracture width = 0.098 ft

Figure 6.12: Normalized fracture (apparent) permeability profiles for the case with the fracture width of 0.098 ft for three different flow rates of 10 in (a), 20 in (b), and 30 MMscf/D in (c), and a comparison of the profiles for these flow rates in (d).

### 6.3.3 Effect of the fracture length

Impact of the fracture length on the gas flow simulation results are investigated by increasing the fracture half-length from 500 ft in the base case to 1000 ft. Figures 6.16 show the impact of the non-Darcy flows on the calculated permeabilities and apparent permeabilities for different flow rates. Calculated apparent permeabilities in this case are extended to the entire length of the reservoir and apparent permeability values in the cells closest to the wellbore are similar to those of the base case for each flow rates. Due to existence of longer

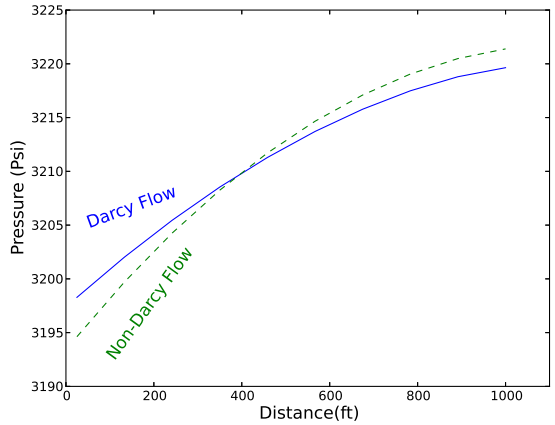


(a) Fracture width = 0.098 ft, $q_g$ = 10 MMscf/d

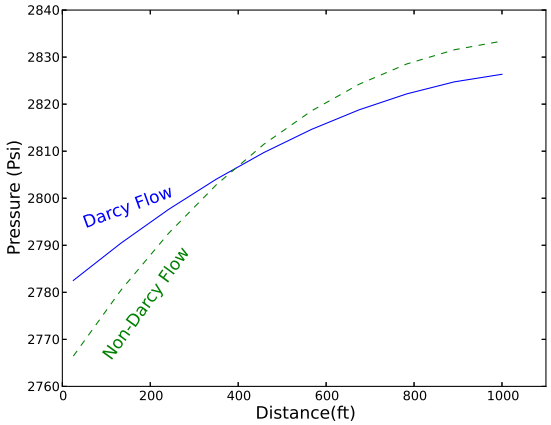


(b) Fracture width = 0.098 ft, $q_g$ = 20 MMscf/d

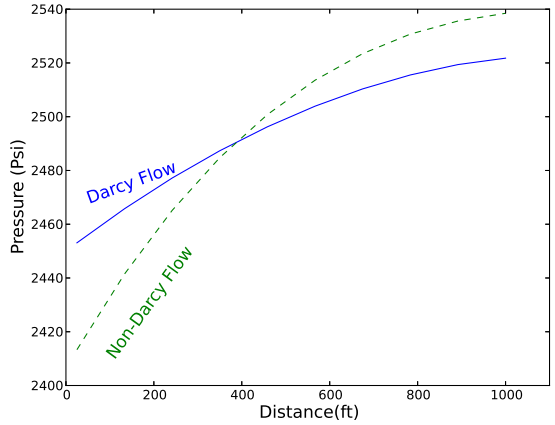


(c) Fracture width = 0.098 ft, $q_g$ = 30 MMscf/d

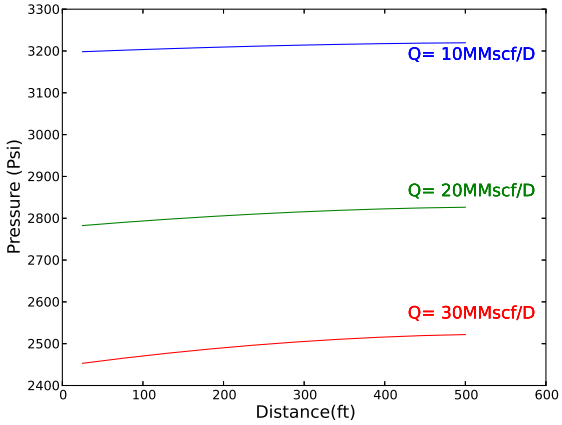


(d) Fracture width = 0.098 ft

Figure 6.13: Fracture pressure profile for the case with fracture width of 0.098 ft for three different flow rates of of 10 MMscf/D in (a), 20 MMscf/D in (b), 30 MMscf/D in (c), and comparison of the pressure profiles for the cases in which non-Darcy flows are considered in the flow simulations. For all the gas flow rates, the fracture pressure in the cell next to the wellbore are slightly higher than the base case for the same gas flow rates.

conduit for delivering gas to the wellbore, the pressure gradients in the fracture (shown in the Figures 6.17) are less significant and the pressures in the cells next to the wellbore are higher in this case than in the base case. Pressure distributions of this case, shown in Figures 6.18 are also significantly different from the base case's. Due to the absence of the fracture tip in this case, hydraulic communications between the reservoir and the fracture occur entirely though the lateral walls of the fracture resulting in almost parallel iso-pressure

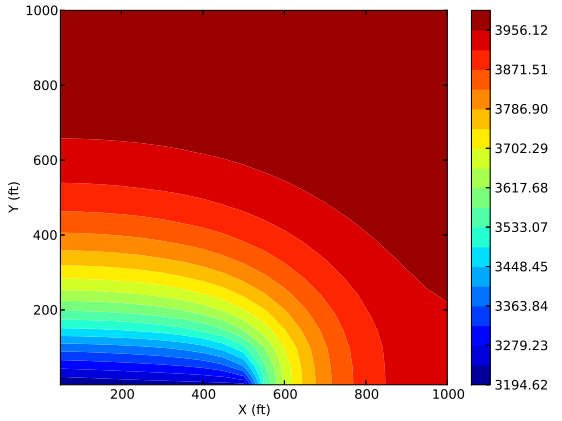


(a) Fracture width = 0.098 ft, $q_g$ = 10 MMscf/d

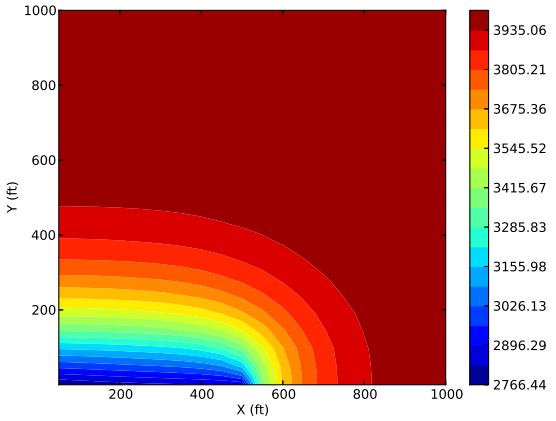


(b) Fracture width = 0.098 ft, $q_g$ = 30 MMscf/d

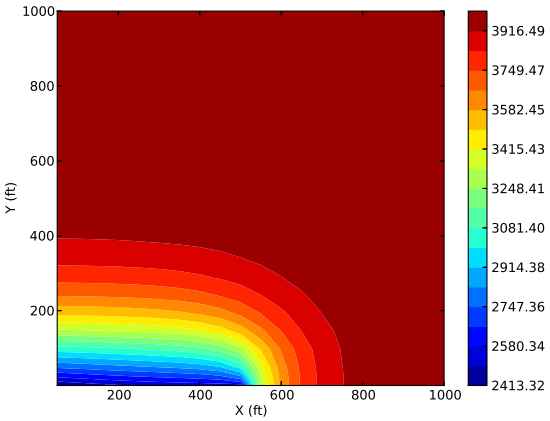


(c) Fracture width = 0.098 ft, $q_g$ = 20 MMscf/d

Figure 6.14: Pressure distributions of the case with a fracture width of 0.098 ft for three different gas flow rates of 10 in (a), 20 in (b), and 30 MMscf/D in (c). For all the flow rates, minimum and maximum flow rates are slightly higher than the base case for corresponding flow rates.

lines to the fracture walls. Calculated productivity indices of this case are plotted in the Figures 6.19. The impact of the non-Darcy flows on the productivity indices are higher in this case compared to the base case due to the fact that non-Darcy flows exist in higher number of cells. Productivity-indices ratio decreases to almost 80% when the gas flow rate is 30 MMscf/D compared to 90% in the base case.

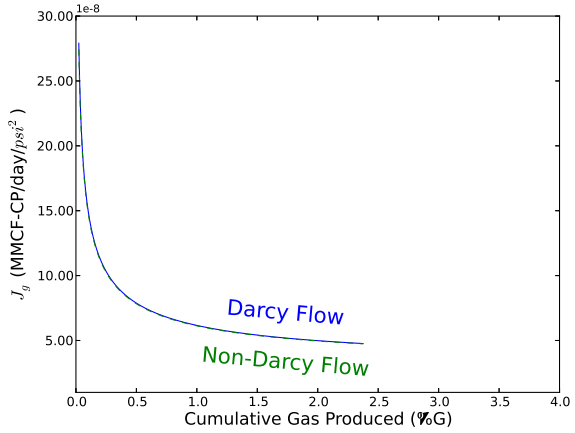


(a) Fracture width = 0.098 ft, $q_g$ = 10 MMscf/d

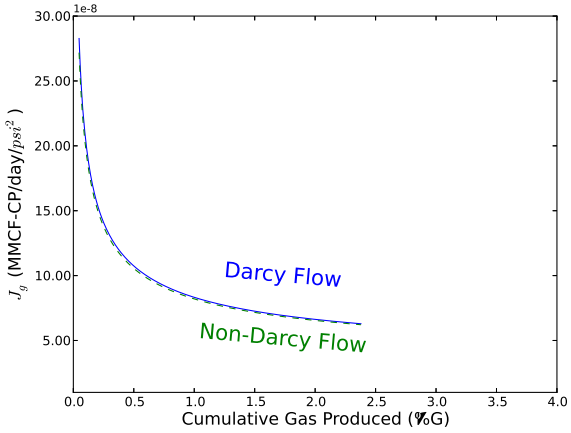


(b) Fracture width = 0.098 ft, $q_g$ = 20 MMscf/d

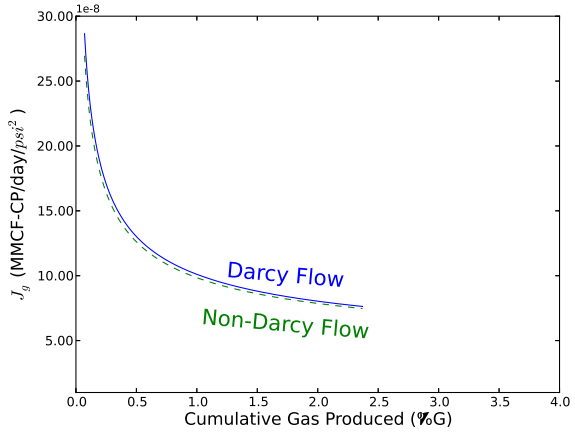


(c) Fracture width = 0.098 ft, $q_g$ = 30 MMscf/d

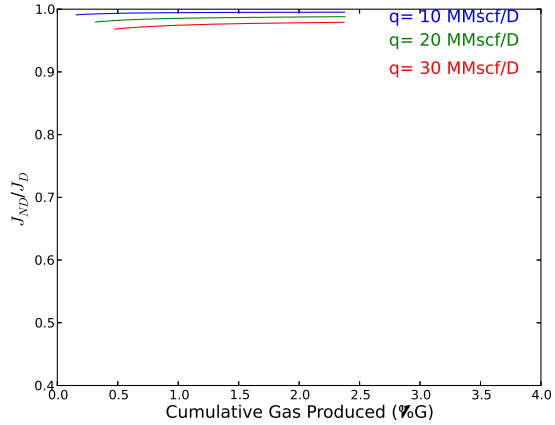


(d) z-direction permeability vs. resolution

Figure 6.15: Productivity indices the case with a fracture width of 0.098 ft for three different flow rates of 10 MMscf/D in (a), 20 MMscf/D in (b), 30 MMscf/D in (c), and comparison of productivity-index ratios for these gas flow rates. Impact of non-Darcy flows in the simualtions are less significant in this case compared to the base case. For gas flow rate of 30 MMscf/D, non-Darcy flows reduce the productivity-index ratios to 95%.

## 6.4 Discussion

Impact of the effective stresses (defined by the difference between the overburdern stresses and the fluid pressures) on the permeability values of the fracture is not significant because according to the pore-scale simulations results, there are slight reductions of permeability with increasing confining stresses. Since the onset of the grain fracturing is not determined from the proppant images, I did not impose conditions in which effective stresses increase

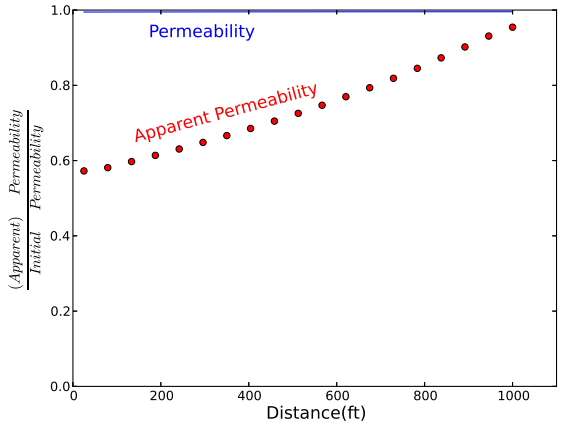


(a) Fracture length = 1000 ft, $q_g$ = 10 MMscf/d

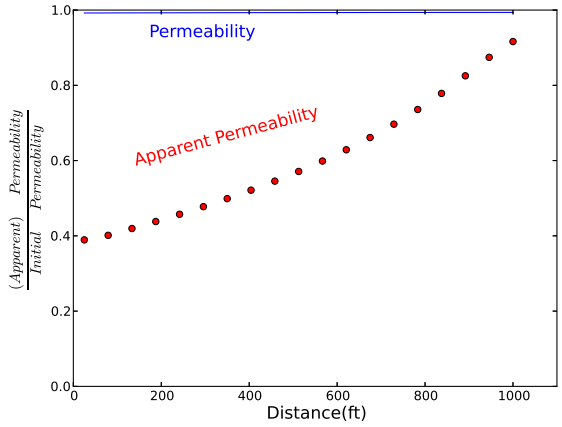


(b) Fracture length = 1000 ft, $q_g$ = 20 MMscf/d

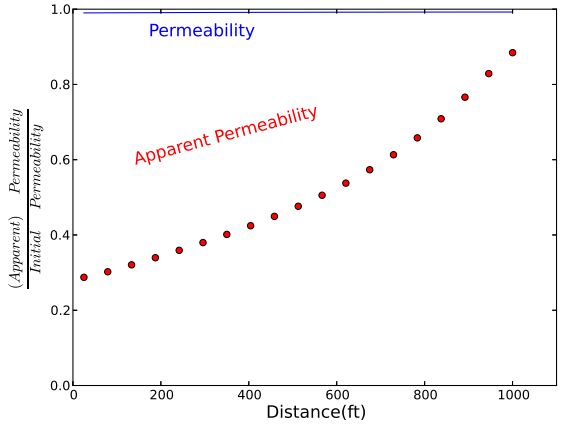


(c) Fracture length = 1000 ft, $q_g$ = 30 MMscf/d

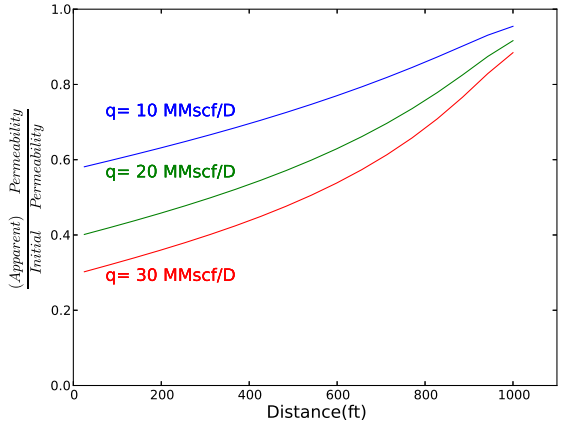


(d) Fracture length = 1000 ft

Figure 6.16: Normalized fracture (apparent) permeability profiles in the hydraulic fracture with the fracture half-length of 1000 ft at three gas flow rates of 10 MMscf/D in (a), 20 MMscf/D in (b), 30 MMscf/D in (c), and a comparison of apparent permeability profiles for these flow rates. The change of apparent permeability with the gas flow rates is similar to the base case results foe corresponding flow rates.

beyond 12000 psi. Therefore, they do not have a substantial impact on the productivity indices.

Including the calculated values of inertial flow parameter in the flow simulations has a significant impact on the calculated apparent permeability values inside the fracture, pressure profiles in the fracture, and productivity indices.

Four different simulation parameters, fracture width, fracture length, gas flow rate, and

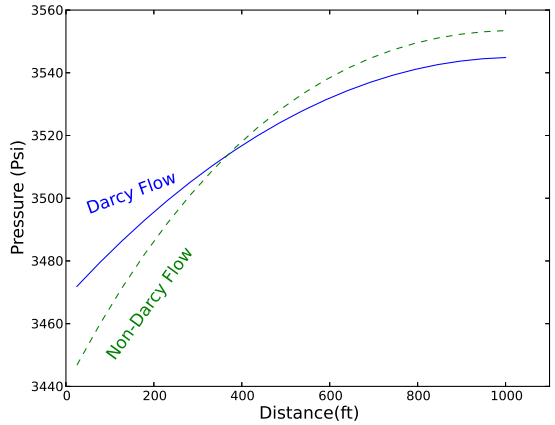


(a) Fracture half-length = 1000 ft, $q_g$ = 10 MMscf/d

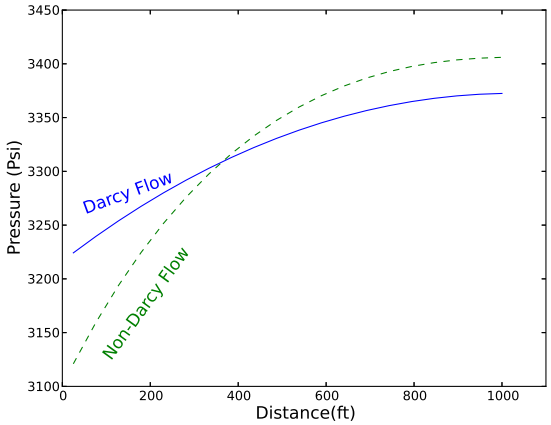


(b) Fracture half-length = 1000 ft, $q_g$ = 20 MMscf/d

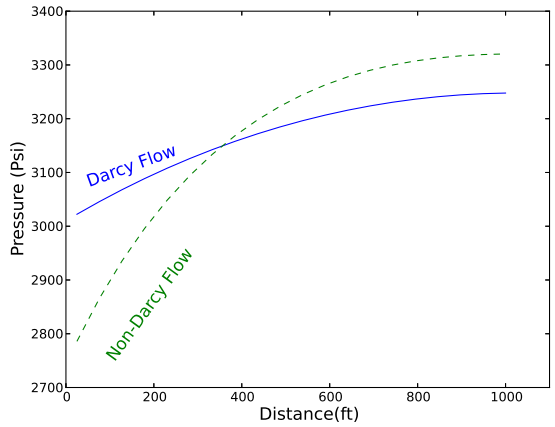


(c) Fracture half-length = 1000 ft, $q_g$ = 30 MMscf/d

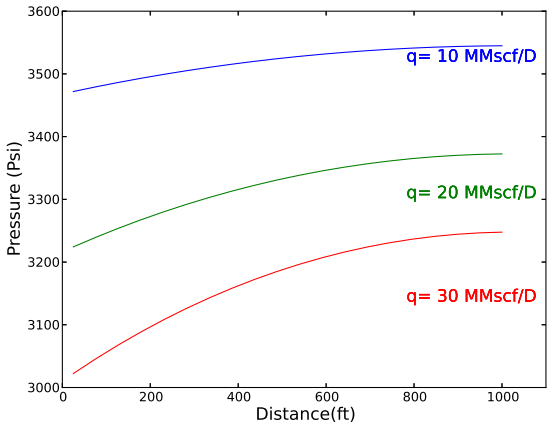


(d) Fracture half-length = 1000 ft

Figure 6.17: Fracture pressure profile for the case with fracture half-length of 1000 ft for three different flow rates of of 10 MMscf/D in (a), 20 MMscf/D in (b), 30 MMscf/D in (c), and comparison of the pressure profiles for the cases in which non-Darcy flows are considered in the flow simulations. The rates of change of the pressures in the fracture with the distance are less compared to those of the base case for corresponding flow rates. The pressure in the cell closest to the wellbore for each flow rate is also higher than those of the base case due to existence of a longer conduit contributing to delivering fluids to the wellbore.

reservoir permeabilities, are investigated in this study. Qualitatively, increasing the fracture width causes the non-Darcy flows to be less significant. This is due to existence of larger cross-sectional areas for fluid flows and therefore, lower flow velocities in the fracture (flow velocities are inversely proportional to the normal cross-sectional area). This causes pressure and apparent permeability drops in the fracture become smaller and productivity-index ratios

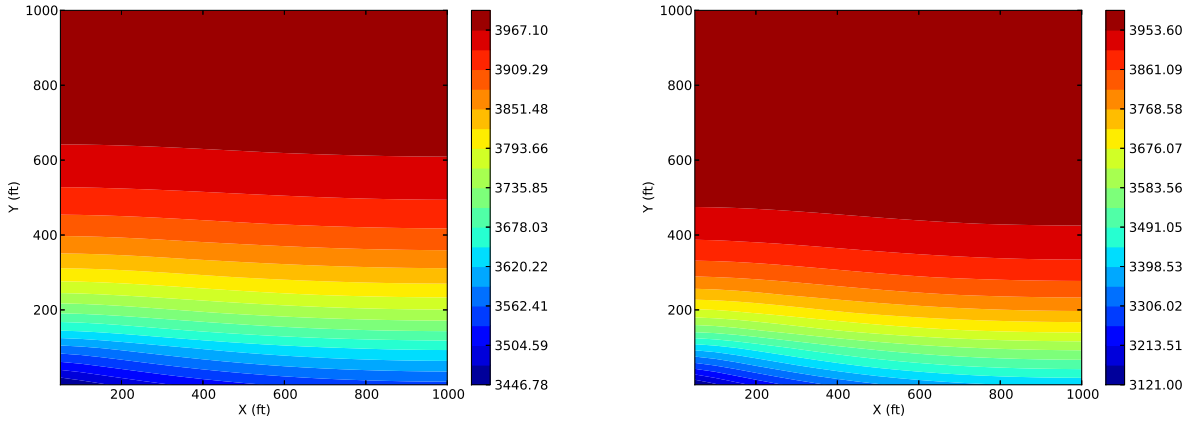


(a) Fracture half-length = 1000 ft, $q_g$ = 10 MMscf/d (b) Fracture half-length = 1000 ft, $q_g$ = 30 MMscf/d

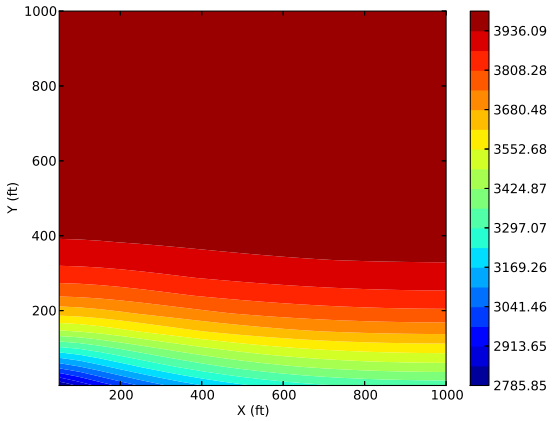


(c) Fracture half-length = 1000 ft, $q_g$ = 20 MMscf/d

Figure 6.18: Pressure distributions of the case with a fracture half-length of 1000 ft for three different gas flow rates of 10 in (a), 20 in (b), and 30 MMscf/D in (c). The pressure distributions in this case are significantly different from the base case's. Because of the absence of the a fracture tip in this case, hydraulic connections between the fracture and the reservoir rock occurs through the walls of the fracture, which results in almost parallel pressure contours around the fracture.

have higher values.

When reservoir permeability increases, impact of non-Darcy flows on the fluid pressures inside the fracture become slightly less significant. These is a better hydraulic communication between the fracture and the surrounding rocks through the fracture walls and therefore, fluid velocities in the direction of fracture (x-direction in the model) are smaller. Rate of decrease in the fracture pressures and apparent permeabilities are slightly less significant according

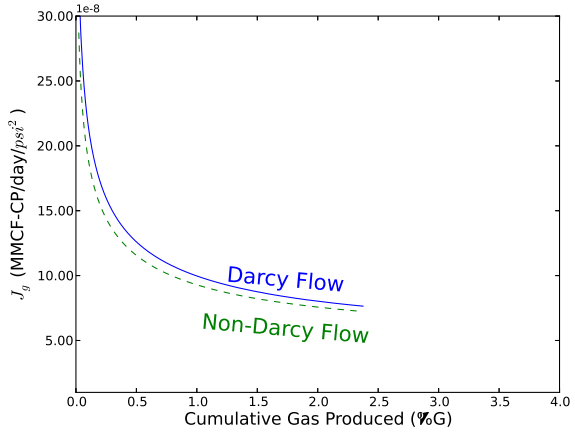


(a) Fracture half-length = 1000 ft, $q_g$ = 10 MMscf/d

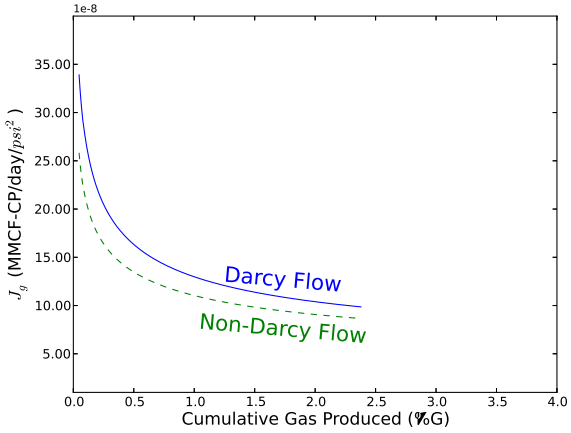


(b) Fracture half-length = 1000 ft, $q_g$ = 20 MMscf/d

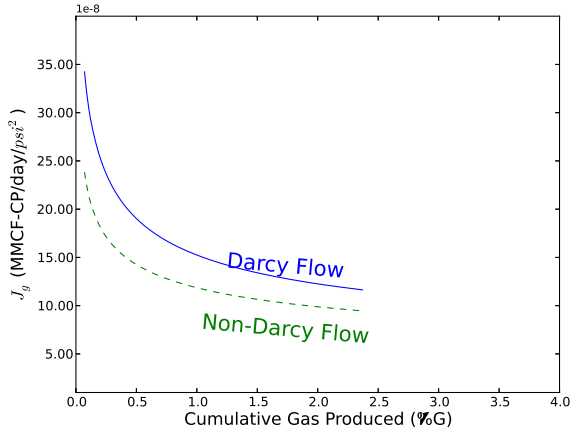


(c) Fracture half-length = 1000 ft, $q_g$ = 30 MMscf/d

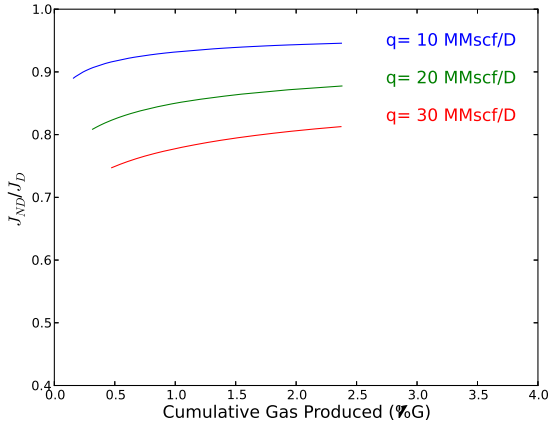


(d) Fracture half-length = 1000 ft

Figure 6.19: Productivity indices the case with a fracture length of 1000 ft for three different flow rates of 10 MMscf/D in (a), 20 MMscf/D in (b), 30 MMscf/D in (c), and comparison of productivity index ratios for these gas flow rates. In this case, since the non-Darcy flows exist in a larger number of cells, the impact of the non-Darcy flows on the productivity indices are higher.

to our simulation results.

Based on the simulation results, when fracture length doubles, the rate of pressure drops in the fracture becomes steeper. This is mainly because of larger number of cells with non-Darcy flows in them. Productivity-index ratios are are also less in this case.

# Chapter 7
# Conclusions and Future Research

## 7.1 Summary

A computer-generated sphere packing with overlapping spheres was used as a surrogate for a consolidated granular material and digitized to create voxel images at five different resolutions. These images, which are free of experimental and segmentation errors, are then used to compute permeability and tortuosity using lattice Boltzmann (LB) and finite elements methods (FEM). The resulting set of images was used to independently probe the effects of both image resolution and numerical resolution (grid spacing or mesh size) on permeability for LB and FEM flow simulations. This approach is important because in practice it is often difficult to separate the effects of these two factors. Because these results are from computer-generated porous media, they do not contain experimental or segmentation errors that are present in real images. This fact, combined with the realistic values for permeability and resolution that were chosen, means that the results presented here provide good benchmarks for the expected performance of LB and FEM results in image-based modeling applications.

Permeabilities and non-Darcy flow parameters of a proppant pack at different confining stresses are computed using LB simulations. The calculated results are compared with the vendor provided data and it is observed that they differ from the vendor provided data. Calculated results are then incorporated into a 2D single-phase gas reservoir simulator. Impacts of fracture width and length, reservoir permeability, and gas flow rates on the productivity indices, fracture pressure and apparent permeability profiles, and pressure distributions in

the reservoir are also investigated.

## 7.2 Conclusions

Evidence from both simulation methods (LB and FEM) shows that the lower-quality images have a correspondingly lower physical permeability (i.e., the actual permeability of the compromised structure). However, the situation is more complex when image resolution and numerical resolution both come into play (as is usually the case in practice). Results show how changes in computed permeability are affected by image resolution (which dictates how well the pore geometry is approximated) versus grid or mesh resolution (which changes numerical accuracy). For LB, the image and grid resolution are usually taken to be the same; we show at least one case where effects of grid and image resolution appear to counteract one another, giving the mistaken appearance of resolution-independent results.

When the LB lattice was taken to be the same as the voxel grid, the computed permeability decreased as image/lattice resolution improved. Additionally, the coarser-resolution images made the simulation results more sensitive to the choice of relaxation parameter.

For the choice of relaxation parameter $\tau = 1.1$, permeability is relatively insensitive to image/lattice resolution. However, we show that this insensitivity is an artifact: a combined effect of 1) the true permeability of the voxel structure increases with improved image resolution (because of geometric and/or topologic changes associated with the approximated pore structure) and 2) the computed permeability decreases with improved image resolution (because of better numerical accuracy). The fact that these two effects can offset one another is important to consider because permeability is often used as a surrogate measure to confirm the quality of results in image-based modeling.

LB and FEM predict similar values of the permeabilities while their local velocity fields are different from one another.

Pore-scale flow simulations show that the permeability is relatively insensitive to stress prior to fracturing of proppant grains and the results differ from the results published by the

proppant vendor. Calculated non-Darcy flow parameters also show a slight increase with increase in confining stress compared to a stress beyond which grain fracturing occurs.

Including non-Darcy flow parameter calculated using image-based flow simulations resulted in substantial changes in pressure profiles in the fracture and productivity index of the well. Based on the simulation results, 20% decrease in the productivity index is observed by including non-Darcy flow parameter in the simulations.

## 7.3 Future Research

This section briefly addresses issues and future work that may be fruitful to other researchers.

### 7.3.1 Pore-scale image-based flow simulations

There are many problems in which the solution to the partial differential equation describing the dynamics cannot be resolved numerically by a set of discrete points. This problem rises usually as a result of lack of computational resources. In image-based flow simulations, this problem arises mainly because of the lack of sufficient resolutions (number of grid points in pore space) and its wide implications on topology alterations of the porous media. Simulation framework to use underresolved image samples such as dolomite to calculate the permeability and non-Darcy flow parameter with a closure model seem to be necessary.

Further studies can also be done on the impact of image and numerical resolutions on image-based inertial flow parameter estimations. A comparison of the two numerical approaches (FEM and LB) can also give some insight about their predictive capabilities.

### 7.3.2 Inertial-flow parameter estimation using pore-scale flow simulations

In 2001, the International Organization for Standardization (ISO) and American Petroleum Institute (API) have organized a new committee to write procedures for measuring the properties of proppants used for hydraulic fracturing. In 2003 a second committee was formed to write procedures on measuring long term conductivity of a proppant pack. These two

new procedures will enable users to evaluate and to compare proppant characteristics under the specifically described test conditions for use in hydraulic fracturing operations. They investigated impacts of elevated temperatures, fracturing fluid residues, cyclic stress loading, embedment, formation fines, and other factors on the proppant pack conductivity [38]. For image-based estimations of properties of proppant packs there seem to be a need for standardization of the simulation procedures. In particular, number of the proppants, thickness of the surrounding porous media, and required image resolutions can be of particular importance.

Verified and validated pore-scale dynamics simulators capable of predicting dynamics of both fluid- and solid-phases can be useful in calculations of properties of porous media. In image-based flow simulations of the real images of porous media, unlike the flow experiments, the movement of the grains and other solid particles due to the drag force of the fluid on the solids can not be accounted for. This drag force can be particularly important for high fluid flows, where inertial flows become increasingly important. In this study, for 20000 psi confining stress, the crushed solid particles can flow with fluid from their nesting regions and plug up some pores and limit the flow. This can influence the calculated permeability and inertial flow parameter.

In hydrocarbon reservoirs, we are dealing with multiphase flow of fluids toward the wellbore. Further studies using multiphase flow simulation models (such as multiphase LB and Level-set approaches in FVM) through estimations of relative permeabilities and multiphase inertial flow parameters can enrich our understanding of hydrocarbon productions.

During the life of a hydrocarbon reservoir, due to occasional work-over and testing operations, cyclic stress alterations may occur that can cause fatigue and may alter calculated properties of the packing. Performing image-based simulations on such samples can be insightful.

Having more images at different confining stresses can help in identifying a more exact determination of the onset of the crushing of the proppants. Pore-scale simulation results

can also be compared with other numerical approaches.

### 7.3.3 Upscaling of pore-scale simulation results

The results of this part can be more useful to other researchers if they are validated with real production data. There are many simplifications in this study that should be addressed for better analyses. In this study, proppant concentrations are assumed to be uniform (fractures are fully propped). More realistic concentration profiles along the length of the hydraulic fractures can be used. Real stress fields inside and around the hydraulic fracture should be used instead of merely using overburden stress. Moreover, investigations with more elaborate fracture geometries, by including induced micro-fractures and fissures, and using single-layer proppant layer data can be done. The reservoir simulator can also be extended to a three-dimensional multiphase model to investigate the impacts of multiphase inertial flow factors and stress-dependent relative permeabilities.

# Bibliography


[1] Al-Hussainy, R. and H. Ramey (1966). Application of Real Gas Flow Theory to Well Testing and Deliverability Forecasting. *Journal of Petroleum Technology 18*(5), 637–642.

[2] Amao, A. M. (2007). *Mathematical model for Darcy Forchheimer flow with applications to well performance analysis*. Ph. D. thesis, Texas Tech University.

[3] Augier, F., F. Idoux, and J. Y. Delenne (2010). Numerical simulations of transfer and transport properties inside packed beds of spherical particles. *Chemical Engineering Science 65*(3), 1055–1064.

[4] Auzerais, F. M., J. Dunsmuir, B. B. Ferréol, N. Martys, J. Olson, T. S. Ramakrishnan, D. H. Rothman, and L. M. Schwart (1996). Transport in sandstone: A study based on three dimensional microtomography. *Geophysical Research Letters 23*(7), 705.

[5] Baker, M. J. and G. R. Tabor (2010). Computational analysis of transitional air flow through packed columns of spheres using the finite volume technique. *Computers & Chemical Engineering 34*(6), 878–885.

[6] Balhoff, M. T. and M. F. Wheeler (2009). A Predictive Pore-Scale Model for Non-Darcy Flow in Porous Media. *SPE Journal 14*, 11–14.

[7] Bosl, W., J. Dvorking, and A. Nur (1998). A study of porosity and permeability using a lattice boltzmann simulation. *Geophysical Research Letters 25*(9), 1475–1478.

[8] Bosl, W. J. and A. Nur (1998). A study of porosity and permeability using a lattice boltzmann equation. *Geophysical Research Letters 25*(9), 1475–1478.

[9] Buick, J. and C. Greated (2000). Gravity in a lattice Boltzmann model. *Physical Review E - Statistical Physics, Plasmas, Fluids, and Related Interdisciplinary Topics 61*(5A), 5307–20.

[10] Chen, S., D. Martínez, and R. Mei (1996). On boundary conditions in lattice Boltzmann methods. *Physics of Fluids 8*(9), 2527.

[11] Chukwudozie, C. (2011). Pore-scale lattice boltzmann simulations of inertial flows in realsitic porous media: a first principle analysis of the forchheimer relationship. Master's thesis, Louisiana State University.

[12] Cornell, D. and D. L. Katz (1953). Flow of gases through consolidated porous media. *Industrial & Engineering Chemistry 45*(10), 2145–2152.

[13] Craft, B. C. and M. F. Hawkins (1990). *Applied Petroleum Reservoir Engineering*. Prentice Hall.

[14] Davies, J. P. and D. K. Davies (2001). Stress-Dependent Permeability : Characterization and Modeling. *SPE Journal 6*(12), 224–235.

[15] Dixon, A. G. (2012). Fixed bed catalytic reactor modelling—the radial heat transfer problem. *Canadian Journal of Chemical Engineering 90*(3), 507–527.

[16] Ertekin, T., J. H. Abou-Kassem, and G. R. King (2001). *Basic Applied Reservoir Simulation*. Society of Petroleum Engineers.

[17] Fatt, I., D. H. Davis, and L. A. Habra (1952). Reduction in permeability with overburden pressure. *Journal of petroleum technology 4*(12), 16.

[18] Ferreol, B. and D. H. Rothman (1995). Lattice-Boltzmann Simulations of Flow Through Fontainebleau Sandstone. *Transport in Porous Media 20*, 3–20.

[19] Firoozabadi, A. and D. L. Katz (1979). An analysis of high-velocity gas flow through porous media. *Society of Petroleum Engineers* (6827-PA).

[20] Forchheimer, P. (1901). Wasserbewegung durch boden. *Z. Ver. Deutsch. Ing 45*(1782), 1788.

[21] Fourar, M., G. Radilla, R. Lenormand, and C. Moyne (2004). On the non-linear behavior of a laminar single-phase flow through two and three-dimensional porous media. *Advances in Water Resources 27*(6), 669–677.

[22] Geertsma, J. (1974). Estimating the coefficient of inertial resistance in fluid flow through porous media. *SPE Journal 14*(5), 445–450.

[23] Ghaddar, C. K. (1995). On the permeability of unidirectional fibrous media: A parallel computational approach. *Physics of Fluids 7*(11).

[24] Ghassemi, A. and A. Pak (2011). Pore scale study of permeability and tortuosity for flow through particulate media using Lattice Boltzmann method. *International Journal for Numerical and Analytical Methods in Geomechanics 35*, 886—-901.

[25] Gunjal, P. R., V. V. Ranade, and R. V. Chaudhari (2005). Computational study of a single-phase flow in packed beds of spheres. *AIChE Journal 51*(2), 365–378.

[26] Guppy, K. H., H. Cinco-Ley, and H. J. Ramey (1982). Pressure Buildup Analysis of Fractured Wells Producing at High Flow Rates. *Journal of Petroleum Technology 34*(11), 2656–2666.

[27] Hassanizadeh, S. M. and W. G. Gray (1987). High velocity flow in porous media. *Transport in Porous Media 2*, 521–531.

[28] He, X., Q. Zou, L.-s. Luo, and M. Dembo (1997). Analytic Solutions of Simple Flows and Analysis of Nonslip Boundary Conditions for the Lattice Boltzmann BGK Model. *Journal of Statistical Physics 87*.

[29] Holditch, S. and R. Morse (1976). The effects of non-darcy flow on the behavior of hydraulically fractured gas wells. *Journal of Petroleum Technology 28*(10), 1169–1179.

[30] Holditch, S. A. and D. M. Blakeley (1992). Flow Characteristics of Hydraulic Fracture Proppants Subjected to Repeated Production Cycles. *SPE Production Engineering 7*(1), 15–20.

[31] Holdych, D. J., D. R. Noble, J. G. Georgiadis, and R. O. Buckius (2004). Truncation error analysis of lattice Boltzmann methods. *Journal of Computational Physics 193*(2), 595–619.

[32] I. Ginzbourg and P. M. Adler (1994). Boundary flow condition analysis for the three-dimensional lattice Boltzmann model. *Journal of Physics II France 4*(2), 191–214.

[33] Jin, G., T. Patzek, and D. Silin (2004). Direct prediction of absolute permeability of unconsolidated and consolidated reservoir rock. spe 90086. In *SPE Annual conference Houston (TX)*.

[34] Jones, F. O. and W. Owens (1980). A Laboratory Study of Low-Permeability Gas Sands. *Journal of Petroleum Technology 32*(9).

[35] Kabir, C., D. Ismadi, and S. Fountain (2011). Estimating in-place volume and reservoir connectivity with real-time and periodic surveillance data. *Journal of Petroleum Science and Engineering 78*(2), 258 – 266.

[36] Kameda, A. (2005). *Permeability Evolution in Sandstone: Digital Rock Approach*. Ph. D. thesis, Stanford.

[37] Kandhai, D., A. Koponen, A. Hoekstra, M. Kataja, J. Timonen, and P. Sloot (1999). Implementation aspects of 3d lattice-bgk: Boundaries, accuracy, and a new fast relaxation method. *Journal of Computational Physics 150*(2), 482 – 501.

[38] Kaufman, P. B., W. Robert, M. Ziegler, R. Aidner, S. M. Neves, M. A. Parker, and K. Abney. Gabriel warwick kerr de paiva cortes, et al. 2007. introducing new api/iso procedures for proppant testing. spe 110697. In *Annual Technical Conference and Exhibition*, pp. 11–14.

[39] Krüger, T., F. Varnik, and D. Raabe (2009, Apr). Shear stress in lattice boltzmann simulations. *Phys. Rev. E 79*, 046704.

[40] Kucinschi, B. R., A. a. Afjeh, and R. C. Scherer (2008). On the application of the lattice Boltzmann method to the investigation of glottal flow. *Journal of the Acoustical Society of America 124*(1), 523–534.

[41] Lane, N. M. (2011). *Numerical Studies of Flow in Porous Media Using an Unstructured Approach*. Ph. D. thesis, Louisiana State University.

[42] Li, Y., E. J. LeBoeuf, P. Basu, and S. Mahadevan (2005). Stochastic modeling of the permeability of randomly generated porous media. *Advances in Water Resources 28*(8), 835–844.

[43] Lin, Z., H. Fang, and R. Tao (1996). Improved lattice Boltzmann model for incompressible two-dimensional steady flows. *Physical review. E 54*(6), 6323–6330.

[44] Lindblad, J. (2005). Surface area estimation of digitized 3d objects using weighted local configurations. *Image and Vision Computing 23*(2), 111 – 122.

[45] Logtenberg, S. A. and A. G. Dixon (1998). Computational fluid dynamics studies of fixed bed heat transfer. *Chemical Engineering and Processing 37*(1), 7–21.

[46] Ma, H. and D. W. Ruth (1993). The Microscopic Analysis of High Forchheimer Number Flow in Porous Media. *Transport in Porous Media 13*, 139–160.

[47] Maier, R. and R. Bernard (2010). Lattice-Boltzmann accuracy in pore-scale flow simulation. *Journal of Computational Physics 229*(2), 233–255.

[48] Maier, R. S., R. S. Bernard, and D. W. Grunau (1996). Boundary conditions for the lattice Boltzmann method. *Physics of Fluids 8*(7), 1788.

[49] Maier, R. S., D. M. Kroll, R. S. Bernard, S. E. Howington, J. F. Peters, and H. T. Davis (2000). Pore-scale simulation of dispersion. *Physics of Fluids 12*(8), 2065.

[50] Maier, R. S., D. M. Kroll, Y. E. Kutsovsky, H. T. Davis, and R. S. Bernard (1998). Simulation of flow through bead packs using the lattice Boltzmann method. *Physics of Fluids 10*(1).

[51] Manwart, C., U. Aaltosalmi, a. Koponen, R. Hilfer, and J. Timonen (2002). Lattice-Boltzmann and finite-difference simulations for the permeability for three-dimensional porous media. *Physical Review E 66*(1), 1–11.

[52] Manz, B., L. F. Gladden, and P. B. Warren (1999). Flow and dispersion in porous media: Lattice-Boltzmann and NMR studies. *AIChE Journal 45*(9), 1845–1854.

[53] Martys, N. S. and H. Chen (1996, Jan). Simulation of multicomponent fluids in complex three-dimensional geometries by the lattice boltzmann method. *Phys. Rev. E 53*, 743–750.

[54] Nabovati, A., E. W. Llewellin, and A. C. Sousa (2009). A general model for the permeability of fibrous porous media based on fluid flow simulations using the lattice Boltzmann method. *Composites Part A: Applied Science and Manufacturing 40*(6-7), 860–869.

[55] Nabovati, A. and A. C. M. Sousa (2007). Fluid Flow Simulation in Random Porous Media at Pore Level Using Lattice Boltzmann Method. *Journal of Engineering Science and Technology 2*(3), 226–237.

[56] Newman, M. S. and X. Yin (2013). Lattice Boltzmann Simulation of Non-Darcy Flow In Stochastically Generated 2D Porous Media Geometries. *SPE Journal 18*(1).

[57] Noble, D. R., S. Chen, J. G. Georgiadis, and R. O. Buckius (1995). A consistent hydrodynamic boundary condition for the lattice Boltzmann method. *Physics of Fluids 7*(1), 203.

[58] Noble, D. R., J. G. Georgiadis, and R. O. Buckius (1995, October). Direct assessment of lattice Boltzmann hydrodynamics and boundary conditions for recirculating flows. *Journal of Statistical Physics 81*(1-2), 17–33.

[59] Okabe, H. and M. Blunt (2004, December). Prediction of permeability for porous media reconstructed using multiple-point statistics. *Physical Review E 70*(6), 1–2.

[60] Pan, C., M. Hilpert, and C. Miller (2001). Pore-scale modeling of saturated permeabilities in random sphere packings. *Physical Review E 64*(6), 1–9.

[61] Pan, C., L.-S. Luo, and C. T. Miller (2006). An evaluation of lattice boltzmann schemes for porous medium flow simulation. *Computers & Fluid 35*, 898–90.

[62] Piller, M., M. Nolich, S. Favretto, F. Radaelli, and E. Rossi (2009). Analysis of hydraulic permeability in porous media: From high resolution x-ray tomography to direct numerical simulation. *Transport in Porous Media 80*(1), 57–78.

[63] Psihogios, J., M. E. Kainourgiakis, A. G. Yiotis, A. T. Papaioannou, and A. K. Stubos (2007). A Lattice Boltzmann study of non-newtonian flow in digitally reconstructed porous domains. *Transport in Porous Media 70*(2), 279–292.

[64] Rivers, M., D. Zhu, and A. D. Hill (2012). Proppant Fracture Conductivity with High Proppant Loading and High Closure Stress. In *SPE 151972*.

[65] Robbins, D. J., M. S. El-Bachir, L. F. Gladden, R. S. Cant, and E. von Harbou (2012). Cfd modeling of single-phase flow in a packed bed with mri validation. *AIChE Journal 58*(12), 3904–3915.

[66] Schure, M. R., R. S. Maier, D. M. Kroll, and H. Ted Davis (2004). Simulation of ordered packed beds in chromatography. *Journal of Chromatography A 1031*(1-2), 79–86.

[67] Shi, Y., T. Zhao, and Z. Guo (2006). Lattice Boltzmann method for incompressible flows with large pressure gradients. *Physical Review E 73*(2), 1–11.

[68] Skordos, P. A. (1993). Initial and boundary conditions for the lattice Boltzmann method. *Phys. Rev. E 48*(6), 4823–4842.

[69] Stahl, B., B. Chopard, and J. Latt (2010). Measurements of wall shear stress with the lattice Boltzmann method and staircase approximation of boundaries. *Computers & Fluids 39*(9), 1625–1633.

[70] Stephens, W. T., S. K. Schubarth, K. R. Dickson, E. M. Snyder, K. J. Doles, and D. Herndon (2007). Behavior of Proppants Under Cyclic Stress. In *SPE 106365*.

[71] Sterling, J. D. and S. Chen (1996). Stability Analysis of Lattice Boltzmann Methods. *Journal of Computational Physics 123*, 196–206.

[72] Stewart, M., A. Ward, and D. Rector (2006). A study of pore geometry effects on anisotropy in hydraulic permeability using the lattice-Boltzmann method. *Advances in Water Resources 29*, 1328–1340.

[73] Succi, S., E. Foti, and F. Higuera (1989). Three-dimensional flows in complex geometries with the lattice boltzmann method. *Europhys. Lett. 10*, 433–438.

[74] Sukop, M. C. and D. T. Thorne (2007). *Lattice Boltzmann modeling: an introduction for geoscientists and engineers*. Springer Publishing Company, Incorporated.

[75] Thompson, K. E. (2007). Computing particle surface areas and contact areas from three-dimensional tomography data of particulate materials. *Particle & Particle Systems Characterization 24*(6), 440–452.

[76] Vairogs, J., C. Hearn, D. W. Dareing, and V. Rhoades (1971). Effect of Rock Stress on Gas Production From Low-Permeability Reservoirs. *Journal of Petroleum Technology 23*(9), 1161–1167.

[77] Vincent, M. C., C. M. Pearson, and J. Kullman (1999). Non-Darcy and Multiphase Flow in Propped Fractures : Case Studies Illustrate the Dramatic Effect on Well Productivity. In *SPE 54630*.

[78] Wyble, D. (1958). Effect of Applied Pressure on the Conductivity, Porosity and Permeability of Sandstones. *Journal of Petroleum Technology 10*(11), 57–59.

[79] Ye, X., N. Tonmukayakul, J. D. Weaver, and J. F. Morris (2012). Experiment and Simulation Study of Proppant Pack Compression. In *SPE International Symposium and Exhibition on Formation Damage Control, 15-17 February 2012, Lafayette, Louisiana, USA SPE 151647*, Number February, pp. 15–17.

[80] Young, P., T. Beresford-West, S. Coward, B. Notarberardino, B. Walker, and A. Abdul-Aziz (2008). An efficient approach to converting three-dimensional image data into highly accurate computational models. *Philosophical Transactions of the Royal Society A 366*(1878), 3155–3173.

[81] Zaman, E. and P. Jalali (2010). On hydraulic permeability of random packs of monodisperse spheres: Direct flow simulations versus correlations. *Physica A: Statistical Mechanics and its Applications 389*(2), 205–214.

[82] Zeng, Z. and R. Grigg (2006). A Criterion for Non-Darcy Flow in Porous Media. *Transport in Porous Media 63*(1), 57–69.

[83] Zhan, X., L. M. Schwart, M. Toksoz, W. Smith, and F. Morgan (2010). Pore-scale modeling of electrical and fluid transport in berea sandstone. *Geophysics 75*(2), F135–F142.

[84] Zoback, M. D. and J. D. Byerlee (1975). Permeability and Effective Stress. *AAPG Bulletin 59*(1), 154–158.

# Vita

Ali Takbiri Borujeni was born in 1983, in Borujen, Iran, to Hedayat and Mahmonir. He attended Taleghani High School for his secondary school education and graduated in 1999. He then proceeded to Abadan Institute of Technology, Iran, from where he earned a Bachelor of Engineering in Petroleum Reservoir Engineering in 2004. Thereafter, he proceeded to a dual degree program at Petroleum University of Technology in Iran and Instittute Francais du Petrole in France, Louisiana, U.S.A., for graduate studies. He is currently a candidate for the PhD in Petroleum Engineering, to be awarded in August 2013. Ali is a volleyball and soccer player. He has been the captain of two times volleyball champion of LSU Intramural Tournaments.